Università degli Studi di Pavia

Facoltà di Ingegneria

Finite Element Analysis of Aortic Valve Surgery

by

Simone Morganti

A Thesis submitted in Fulfilment of the Requirements for the Degree of Doctor in Philosophy in

Bioengineering and Bioinformatics
at Università degli Studi di Pavia, Pavia, Italy

Ph.D. Program Coordinator: Prof. A. Buizza

Supervisor:
Prof. F. Auricchio - Università degli Studi di Pavia

XXIV Ciclo (2008-2011)

All models are wrong;
some are useful
G. Box

Acknowledgements

Time goes fast. Writing the acknowledgements is always the last think to do, probably the first making you aware of the approaching Ph.D. program conclusion.
These last three years gave me the opportunity to do many interesting, often exciting, activities which I probably would have never done otherwise.
Modeling in the field of medicine is to me one of the most beautiful things to do...I had the opportunity to create models of heart valves working closely with physicians and surgeons.
Moving around the world is something really exciting...I had the opportunity to live for six months in the United States. That was amazing!
Meeting people and adding names to the friend list is one of the meanings of life...I had the opportunity to know many people from different countries and cultures.
These are just some few reasons for which I would like to thank, first of all, Prof. Ferdinando Auricchio who encouraged and supported me during the whole Ph.D. project. Thank you for motivating me with your knowledge, experience and kindness.
Then, I would like to thank Alessandro for his professional competence and, above all, friendship.
Thanks to all my lab-mates: Elisa, Giuseppe, Carolina, Adrien, Anna, Mauro, Andrea but also Matthieu and all the american guys working in office 3.402. Thank you for lightening the fun burden of doing research (...even though increasing, in parallel, the amount of caffein in my body).
Special thanks to Michele who has been a real guide for me during these three (and more) years. Thank you friend for sharing with me joys and sorrows of research as well as emotions of life.
Last but not least, I would like to thank my family whose education and support have constituted the unavoidable fuel of this fantastic experience.
Finally, thanks to Sissi for her essential support, smile, patience, deep love.

Contents

English summary

THE proper pumping function of the heart is determined by both the action of the muscular wall and the efficiency of the four heart valves, which allow blood flow in only one direction. In particular, the aortic valve regulates blood flow from the left ventricle to the aorta, preventing regurgitation. Heart valve pathologies represent a remarkable contribution to cardiovascular diseases, which are the major cause of death in the Western countries. In particular, the increase of life expectancy and, consequently, of population average age has favored the genesis and progression of degenerative diseases affecting heart valves. For this reason, research activities in this field are strongly encouraged, representing a significant resource to support and improve both diagnoses and treatments.
The historical and current paradigm in cardiovascular medicine is diagnosis and physicians are mainly driven by experience to determine a medical condition and, then, plan an intervention. The medical procedure success is strongly related to surgeon expertise remaining, in some aspects, *more art than science*.
Moreover, nowadays statistics is the common approach to establish whether a medical remedy is appropriate or not. However, statistics alone is not a reliable predictor of success for individual patients. There is simply too much variability from case to case, especially for diseased patients.
All these considerations represent a strong motivation to study by means of numerical methods both physiologic and pathologic heart valve behavior and, at the same time, to evaluate in advance the efficacy and optimality of specific treatments.
In this context, computational studies and, in particular, finite element analyses, are innovative tools to predict the outcome of a specific surgical operation. The present work is collocated within this scenario of *predictive medicine* since we use numerical simulations to investigate several aspects of aortic valve surgery with the aim of supporting the operation planning procedure by helping heart surgeons in choosing the optimal strategy for a specific patient.

Italian summary

Il sistema valvolare cardiaco garantisce, insieme alla parete muscolare, la funzione di pompa del cuore. In particolare, la valvola aortica permette al flusso sanguigno di avanzare nell'aorta durante la fase di contrazione cardiaca (sistole), impedendo un reflusso nel ventricolo sinistro durante la fase di rilassamento del cuore (diastole).

Tra le malattie cardiovascolari, che rappresentano la principale causa di morte nei paesi occidentali, le disfunzioni delle valvole cardiache ed, in particolare, le patologie della valvola aortica, costituiscono un contributo significativo destinato a crescere negli anni. Infatti, l'aumento dell'età media della popolazione e dell'aspettativa di vita favorisce il manifestarsi e il progredire delle malattie degenerative valvolari. Questo costituisce un forte stimolo per la ricerca scientifica in questo settore; ricerca che rappresenta un'importante risorsa per il miglioramento sia delle diagnosi che delle terapie (chirurgiche e non).

Il paradigma corrente nella medicina cardiovascolare è la diagnosi ed è l'esperienza che guida principalmente il medico per la classificazione della malattia e la pianificazione dell'intervento terapeutico; la statistica è la principale metodologia attualmente adottata per stabilire se uno specifico rimedio medico possa essere definito appropriato oppure no.

Risulta però evidente che la statistica non può rappresentare un valido indicatore di successo in casi specifici data l'alta variabilità anatomica e patologica che richiederebbe trattamenti ottimizzati in modo specifico per ogni paziente.

Inoltre, in letteratura si legge frequentemente che, allo stato attuale, gli interventi sulla valvola aortica presentano aspetti attribuibili più all'arte che alla scienza.

Queste considerazioni rappresentano una forte motivazione sia a studiare numericamente il suo funzionamento in condizioni fisiologiche e patologiche, sia a valutare quantitativamente quanto siano veramente efficaci e ottimali particolari interventi chirurgici, riparativi o sostitutivi.

A questo proposito, gli studi computazionali e tra questi, in particolare, le analisi agli elementi finiti, costituiscono un innovativo strumento per predire l'esito di un particolare trattamento chirurgico.

Proprio in questo contesto di *medicina predittiva* si inseriscono le poten-

zialità di strumenti ingegneristici computazionali atti a ottimizzare determinate scelte chirurgiche (per esempio riguardanti le dimensioni, la tipologia, il posizionamento di una particolare protesi) durante la fase di pianificazione dell'intervento.
Le simulazioni numeriche, infatti, mirano ad ottimizzare la scelta della protesi, studiando, per uno specifico paziente, diverse possibili configurazioni ed evidenziandone sia i valori di coaptazione durante la fase di diastole, sia gli stati di sollecitazione e deformazione.
La modellazione della valvola aortica, delle protesi utilizzate nelle tipologie di intervento considerate, così come la simulazione dell'accoppiamento tra le due parti presentano, dal punto di vista ingegneristico, diverse difficoltà a causa della loro complessità anatomo-funzionale: la geometria, le proprietà del materiale, le condizioni di carico, rappresentano tutti problemi di non immediata soluzione, oggetto di studio di questa tesi di dottorato.

Chapter 1

Introduction

THE engineering science is constantly under rapid and irreversible change since the advent of computers. Both computational modeling and computer capabilities are growing fast. At present, computational analysis is widely adopted in the industrial world to design and optimize sophisticated products and systems: "design speaks to analysis and analysis speaks to design" [1].

1.1 Computational science and cardiovascular diseases

In the last decades, the evolution of computational science has enabled the study of biomedical problems and structures which are characterized by complex geometries, heterogeneous materials and whose functionality is determined by multiple concomitant factors.
The application of modern computational techniques in the field of biomechanics represents a challenging research activity since it may lead (i) to an improvement of the basic knowledge of physiology, (ii) to the development of methodologies, diagnostic tools, therapeutic devices, materials and innovative prostheses for medical applications and, last but not least, (iii) to the prediction of surgical outcomes. All of these aspects may contribute to a progressive advance in medicine and, in particular, in cardiovascular surgery.
Cardiovascular disease (CVD) is, in fact, the leading cause of death both in Europe and in the United States. Each year CVD causes 4.3 million deaths (nearly half of all deaths) in Europe involving an estimated cost of €192 billion a year [2] while in the United States, on the basis of 2006 mortality rate data, nearly 2300 americans die of CVD each day, an average of 1 death every 38 seconds, implying a total direct and indirect cost around $503.2 billion [3].
Valvular heart disorders represent a remarkable contribute to CVD, even though often underestimated. Older age and increasing life expectancy make

valvular heart disease and degeneration a serious and growing public-health problem, thus requiring appropriate resources to improve diagnosis, treatment and research [4]. Nearly 30% of all adults over 65 have a sclerotic aortic valve, 10% of which having accompanying stenosis [5]. More than 300000 heart valve surgical operations were performed in 2006 worldwide [4].

1.2 Towards a change in medical paradigm: from diagnosis to prediction

The current paradigm in cardiovascular medicine and valvular surgery is diagnosis and experience represents the main access to disease classification and treatment planning.
Up to now, there is no effort to predict the outcome of an operation. Statistics is the principal way to establish whether a specific medical remedy is suitable and appropriate or not. However, statistics cannot represent a reliable predictor of success for individual patients since there is high variability from case to case, especially in pathologic situations: anatomical variability and morphological alterations due to pathology would warrant specific surgical procedures and prosthetic devices tailored to each specific patient.
This is confirmed, for example, by Tyrone-David, currently one of the most well-known surgeons of the aortic valve, father of the aortic valve sparing technique, who stated that "...like most reconstructive procedures in cardiac surgery, the actual performance of the operation remains more art than science" [6]. For this reason, surgeon skill and expertise, which are obviously basic requirements to ensure a satisfactory success rate of a procedure, should be supported by innovative predictive approaches provided by computational science.
This concept can be referred to as "predictive medicine" in which patient-specific simulations are performed to evaluate the efficacy of various possible treatments and to plan and design the optimal surgical solution based on predictions of outcomes provided by computational modeling. Of course, in order to achieve the above-mentioned goal, engineers need to strictly collaborate with physicians since anatomy, physiology, histology and pathology are all essential ingredients for realistic aortic valve computer-based simulations.

1.3 Aortic valve models: state of the art

In the context of predictive medicine, modern computational methods play a crucial role and, in particular, finite element analysis (FEA), which is a powerfull, well-known and well-established technology for performing virtual computer-based simulations, represents the key to anticipate pathologic

configurations and surgical outcomes.
The first engineering and mathematical studies on the aortic valve date back to the 70's with the pioneering works by a group of the Washington University that first characterized the mechanics of human aortic valve by computing the stress/strain distribution throughout the leaflet structure [7, 8, 9] and by creating specific mathematical models of the valve leaflets [10, 11].
In 1983, Sauren developed a theoretical model to gain insight into the factors which govern the mechanical behavior of the natural aortic valve after closing [12].

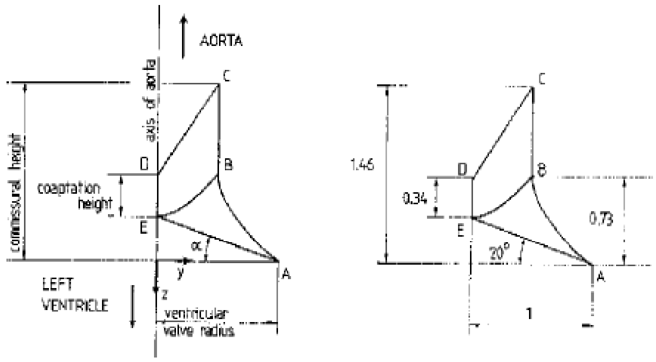

Figure 1.1 *Aortic valve model presented by Sauren in his PhD thesis [12].*

During the 80's a great contribution to the investigation of aortic valve mechanics has been given by several authors, who particularly focused on the modeling of bioprostheses by both a geometrical and constitutive point of view: Christie and Medland (1982) performed non-linear finite element stress analyses of bioprosthetic heart valves [13] while Sabbah et al. (1985, 1986) employed a finite element model of a porcine trileaflet bioprosthesis, paying particular attention to stress localization and its correlation with calcification [14, 15]. Rousseau et al. (1988) included viscoelastic material properties into their closed bioprosthetic model [16].
In 1990, Thubrikar published a detailed book on the aortic valve [17], that is still a reference book, in which he proposed a geometrical model of the valve and also deepened other different aspects such as valve physiology, dynamics and pathology.
In the last twenty years, many other computational studies have been pursued concerning either the aortic valve material modeling or geometrical aspects as well as the impact of valvular pathologies on valve functionality. The leaflets of natural aortic valve are highly non-linear and anisotropic [18]. The effects of anisotropy have been studied to evaluate leaflet stress distribution in polymer composite prostheses [19]. Moreover, finite element

analyses have shown that orthotropy has to be considered during the manufacturing process of bioprosthetic devices, since it can negatively affect both the displacements of the leaflets and their stress distribution [20].
Driessen et al. (2003, 2005) proposed a numerical representation of mechanically induced collagen fibers architectures in aortic leaflet tissue [21, 22, 23] while Freed et al. (2005) developed a transverse isotropic non-linear constitutive model which takes into account the dispersion of collagen fibers experimentally observed [24]. Finally, Koch et al. (2010) performed static finite element analyses of the whole aortic root in diastolic configuration to investigate the influence of non-linear and anisotropic material properties [25].

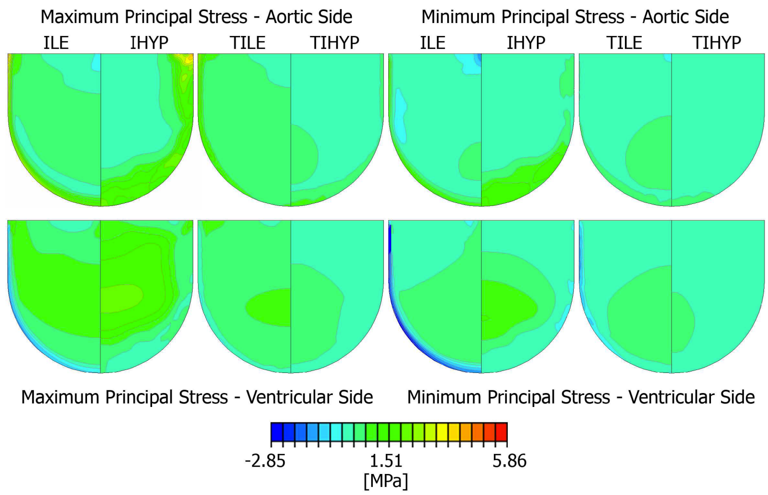

Figure 1.2 *Influence of material properties on stress distribution: contour plots of principal stresses [25].*

In dealing with the geometry of the human trileaflet aortic valve, Labrosse et al. (2006) proposed a new approach to accommodate the wide dimensional variety observed in normal human aortic valves based on fully 3D analyses [26] .
Attention to valve design has been payed also by Clift et al. (1996) who focused on syntetic leaflets [27] while Knierbein et al. used finite element models to improve the design of polyeurethan valves [28]. More recently, Xiong et al. highlighted the importance of leaflet geometry for stentless pericardial aortic valves [29].

Numerical and computational technologies have been adopted to study pathologies of the aortic valve.
In particular, we quote the works by Grande-Allen et al. who used MRI-derived models to associate aortic root dilation with valve incompetence,

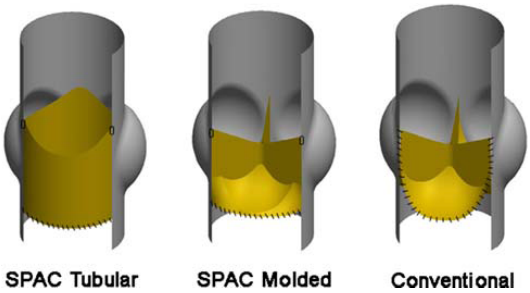

Figure 1.3 *Schematic representation of the SPAC tubular, SPAC molded, and conventional valve models, illustrating differences in implantation approach and leaflet geometry [29].*

stating that dilation leads to higher values of stress and strain in the leaflets [30, 31]. They also investigated the effects of normal aging by increasing both the thickness and the stiffness of the aortic structure, showing that it may result in valvular regurgitation [32].
Conti et al. demonstrated by means of a finite element model that bicuspid geometry per se entails abnormal leaflet stress which may play a role in tissue degeneration [33], while Auricchio et al. developed a new procedure to reproduce the aortic root pathologic dilation on the basis of experimentally measured parameters [34].

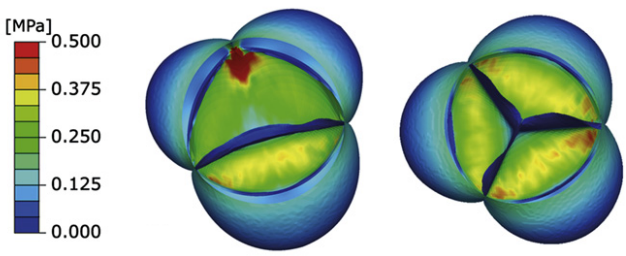

Figure 1.4 *Maximum principal stress distribution on the aortic root for the bicuspid and tricuspid valve at a diastolic pressure gradient of 108 mmHg [33].*

The dynamical behavior of the aortic valve throughout the cardiac cycle has been investigated using numerical models by Gnyaneshwar (2002) who simulated the whole cardiac cycle to analyze the interaction between the aortic root and the leaflets [35]. Dynamic finite element analysis has been performed by Conti et al. (2010) who obtained leaflet stretches, leaflet coaptation lengths and commissure motions, as well as the timings of aortic leaflet closures and openings, all matching with the experimental findings reported in the literature [36] .
Finally, finite element models of the aortic valve have been adopted to predict surgical outcomes. In particular, the aortic valve sparing technique

has received a lot of attentions: Grande-Allen et al. (2001) discussed the influence of graft shape and stiffness on post-operative valve performance concluding that the optimization of both the graft shape and material design may result in improved longevity of the spared valve [37].
Ranga et al. (2006) evaluated aortic reconstruction following valve-sparing operation and validated the simulation results with MRI in vivo data [38].
In Soncini et al. (2009), the aortic root performance after valve sparing procedure is estimated by means of a comparative finite element analysis.

1.4 Aim of the doctoral research

The ultimate goal of our research is to provide heart surgeons and cardiologists with improved technologies to prevent and treat aortic valve diseases, resulting in lower morbidity and mortality as well as reduced re-operative rates and post-operative recovery time.
The proposed aortic valve simulation tool aims at providing a basis for developing predictive patient-specific technology that will help surgeons during the operation planning procedure in choosing the optimal prosthetic device for each specific patient.

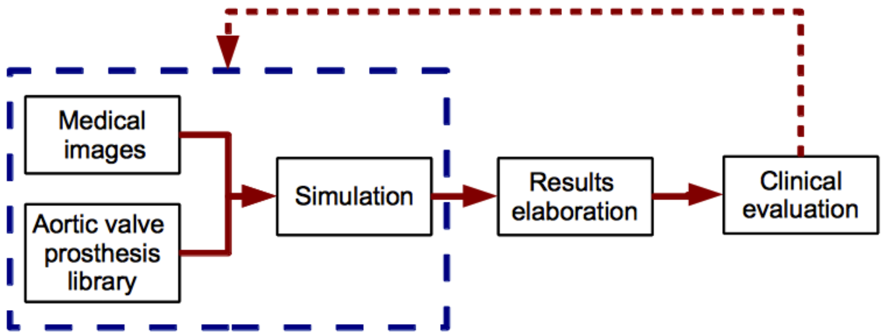

Figure 1.5 *Work-flow of the computational framework to evaluate post-operative aortic valve performance after valve surgery in a patient-specific anatomy: starting from medical images, we create the geometrical model of the aortic root; then, we combine the obtained anatomical region of interest with a given prosthesis model so to simulate the surgical intervention. The elaboration of results leads to the evaluation of post-operative valve performance. The framework allows the investigation of different "What If?" scenarios aiming at supporting the surgeons during the operation planning procedure.*

The flow chart in Figure 1.5 represents the methodological process summarizing the computer-based procedure to support heart surgery.
By means of numerical modeling and simulations is in fact possible to investigate several "What If?" scenarios considering different prosthesis ge-

ometries and materials and evaluate their performance in specific cases.

1.5 Organization of the dissertation

The dissertation is organized as follows:

- Chapter 2: The aortic valve

  Given the aim of predicting the aortic valve performance following a particular surgical operation by means of realistic computer-based simulations, it is essential to understand valve functioning from different points of view. In this first chapter, the basic principles of valve structure are reviewed. In particular, (i) the anatomy is described carefully since it is the unique way to shed some light on the complex valve geometry, (ii) the physiology is delineated to understand valve dynamics, external loads and boundary conditions in general; (iii) the histology is briefly deepened since it is fundamental for properly modeling material behavior; (iv) the main pathologies are then outlined to allow the representation of valve morphological alterations and disfunctioning in case of disease. Moreover, some hints on the diagnostic tools adopted in case of aortic valve disease are provided since their outcome represents the starting point for patient-specific simulations.

- Chapter 3: FEA of the aortic valve

  In this chapter, we move from the basic analysis of physiological valve closure to describe each single ingredient of the finite element simulation. First of all, we describe how it is possible to obtain proper geometrical models directly from medical images of different typologies (CT-A or ultrasound). Then, we go through material modeling and, in particular, we present the anisotropic constitutive equations adopted to describe the fiber-reinforced material behavior. Finally, a description of the considered boundary conditions is given and some analysis aspects used for the simulations are highlighted as well.

- Chapter 4: FEA to support surgical operation planning

  Herein, a numerical and theoretical framework to simulate aortic valve surgery is presented. In particular, three different typologies of interventions are virtually reproduced to anticipate surgical outcomes. Firstly, aortic valve replacement by means of biological stentless valve is simulated investigating the impact of both prosthesis size and implantation site in patient-specific geometries. Secondly, aortic valve sparing procedures are reproduced through computer-based analyses to identify the optimal graft size and type to be adopted in specific cases. Finally, the innovative surgical procedure of trans-catheter aortic valve implantation is simulated with the aim of demonstrating the capability of FEA with a particular focus on the prosthetic device positioning.

- Chapter 5: Conclusions and future works

  In this last chapter, the conclusions are drawn highlighting the original aspects of the doctoral research. Moreover, further research developments are outlined.

Chapter 2

The aortic root

REALISTIC computer-based simulations require an understanding of the aortic valve structure. In fact, it is well-recognized that aortic valve function strictly depends on complex anatomic and dynamic relationship of aortic valve and root, as demonstrated by Kunzelman et al. (1994) who examined the aortic valve structure in cryopreserved normal adult human specimens [39]. For this reason, the study of both valve histology, from a micro-structural point of view, and anatomy, from a macro-structural point of view, as well as the study of valve physiology and pathology, are basic requirements for a computational investigation of aortic valve function.

2.1 The heart

The cardiovascular system is composed of the heart, which pumps the blood, and the network of blood vessels that convey blood to the body and drain it from the body tissues to the heart.
The heart is a muscular organ made of two synchronized pumps in parallel: the right side, which collects deoxygenated blood from the systemic veins and perfuses the lungs, and the left side, which collects oxygenated blood from the pulmonary veins and perfuses the rest of the body.
Each side is made of two chambers, an atrium and a ventricle. As depicted in Figure 2.1, the right atrium receives deoxygenated blood from the body which is pumped by the right ventricle into the lungs. The oxygenated blood coming from the lungs is collected by the left atrium and it is perfused to the rest of the body through the left ventricle, which is the largest heart cavity with the thickest wall. The two ventricles share a septum, which separates the heart into the left and right sides. The heart is surrounded by an inelastic membrane, called *pericardium*, that restricts excessive dilation of the heart and can limit ventricular filling.

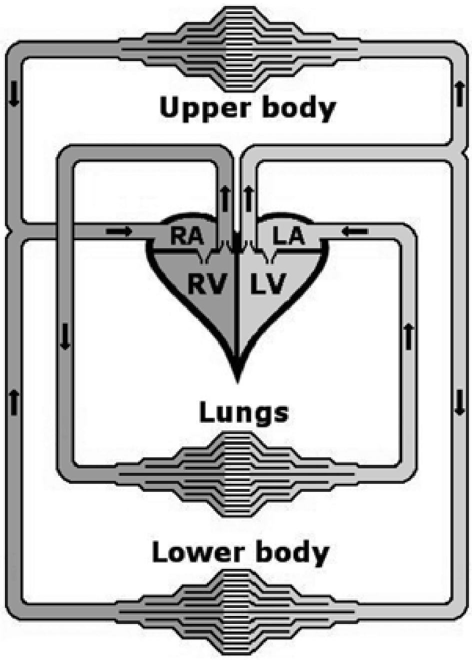

Figure 2.1 *A sketch of the cardiovascular system adapted from [40].*

During the cardiac cycle the heart contracts to allow blood ejection (systolic phase) while it relaxes after contraction in preparation for refilling with circulating blood (diastolic phase).
Four types of valves regulate blood flow through the heart during systole and diastole, as depicted in Figure 2.2:

- The **tricuspid valve** regulates blood flow between the right atrium and right ventricle. The normal tricuspid valve usually has three leaflets connected to the three papillary muscles by the chordae tendineae which lie in the right ventricle.

- The **pulmonary valve** is a semilunar valve made of three cusps. It controls blood flow from the right ventricle into the pulmonary arteries which carry blood to the lungs to pick up oxygen.

- The **mitral valve** lets oxygen-rich blood from the lungs pass from the left atrium into the left ventricle. It has two leaflets and it is prevented from prolapsing by the chordae tendons and papillary muscles running from the cusps of the valve leaflets to the side of the left ventricle.

- The **aortic valve** opens the way for oxygen-rich blood to pass from the left ventricle into the aorta, which is the body's major artery, where it is delivered to the rest of the body.

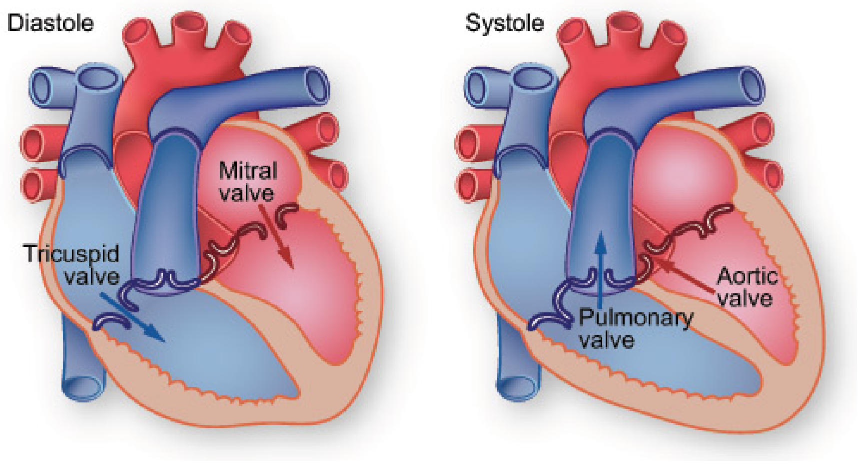

Figure 2.2 *Sketches of the heart cross section showing the gross anatomy: the opening and closing phases of the four cardiac valves are represented during systole and diastole [41].*

Blood is supplied to the heart by its own vascular system, called coronary circulation: the right and left coronary arteries originate from two of the three sinuses of Valsalva, just above the aortic valve.

2.2 Anatomy of the aortic root

The aortic root is a bulb-shaped fibrous structure situated between the ascending aorta and the left ventricle outflow tract which supports the aortic valve leaflets and gives origin to the coronary arteries.
The aortic root consists of different anatomic entities [42]:

- the sinotubular junction,
- the Valsalva sinuses,
- the leaflets,
- the commissures,
- the interleaflet triangles,
- the ventriculoaortic junction.

In Figure 2.3, an external view of the reconstructed aortic root is represented and the principal anatomic constituents are highlighted.

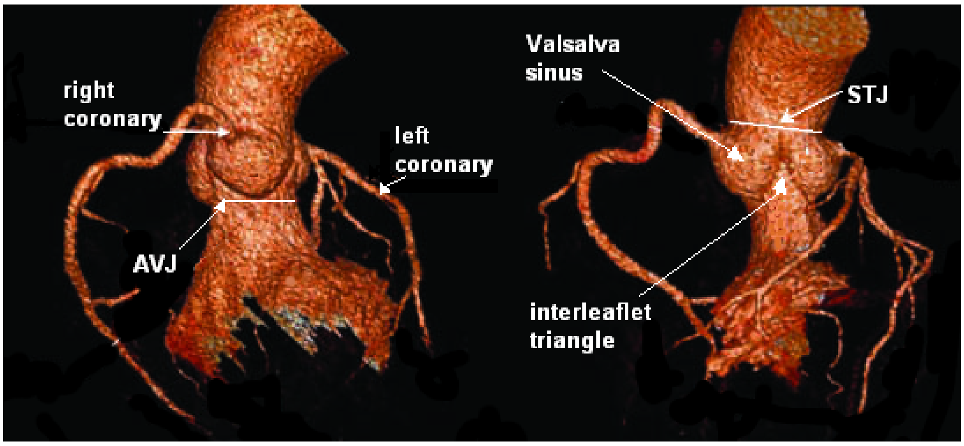

Figure 2.3 *Aortic root reconstructions: the principal anatomic components of the aortic root are highlighted [42].*

2.2.1 The leaflets

Normal aortic valves have three semilunar leaflets (or cusps), which are the most mobile parts of the valve since they open and close during systole and diastole, respectively (see Figure 2.4). They are very thin and flexible so that they may come together to seal the valve orifice during diastole and avoid retrograde blood flow from the aorta to the ventricle.

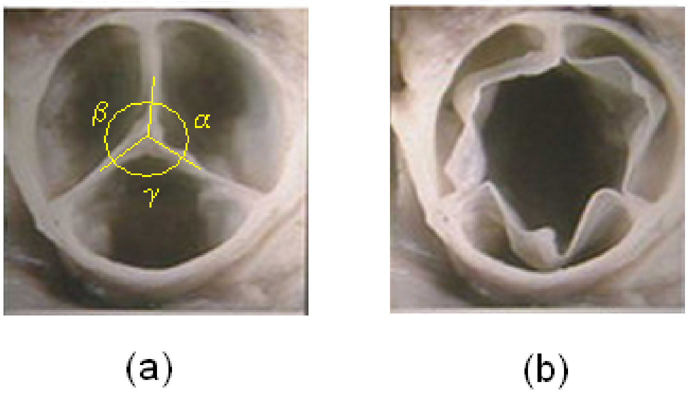

Figure 2.4 *The aortic valve leaflets: (a) in the closed configuration (diastole) they form the angles α, β, and γ; (b) in the open configuration (systole).*

During the diastolic phase, each leaflet coapts against the other two leaflets; the area of the cusps in contact is called *coaptation area* which should not be considered redundant since it does bear a load. The only free boundary of the leaflet, which is also the distal boundary of the coaptation surface, is called *free margin* or *free edge* of the leaflet (it is well-visible in Figure 2.4a

since it forms the *mercedes-like* shape during diastole).
In Figure 2.5a the three leaflets are visible from a cut view of the excised aortic root. A single leaflet is isolated and highlighted in Figure 2.5b.
Finally, in Figure 2.5c, a sketch of a single leaflet is represented and the main components are shown: AL indicates the leaflet line of attachment to the Valsalva sinuses, CL the coaptation line and CA the coaptation surface; FE represents the free edge while RD and CD the radial and circumferential direction, respectively.

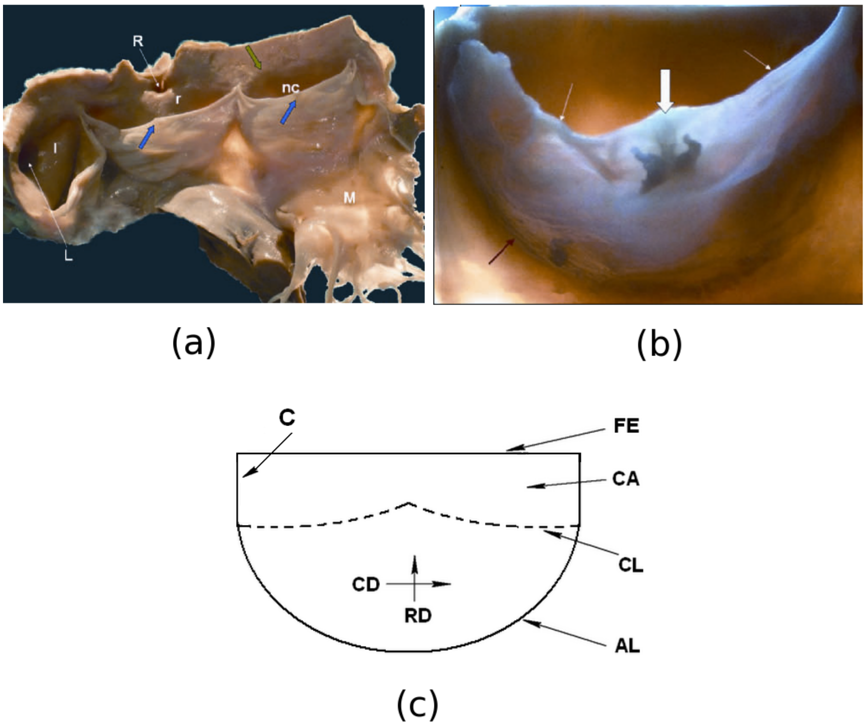

Figure 2.5 *The aortic valve leaflets: (a) an internal view of the excised aortic root highlights the three leaflets adapted from [42]; (b) a single leaflet is isolated [42]; (c) a sketch of the leaflet puts in evidence its main components.*

The leaflet *commissures* (C) are formed by the mural regions where two leaflets insert side by side along parallel lines [17]. As reported by Sutton et al. (1995), there exist at least two definitions for commissure which are pertinent for the aortic valve: (1) a joining together; the place where two bodies touch or unite; (2) the line of junction or angles of the two lips, eyelids, etc... Both of these definitions would fit with the description of the zones of apposition between the leaflets of the aortic valve [43].
The free margin of each cusp shows a central corpus called *nodule of Arantius* highlighted by the white arrow in Figure 2.5b. The aortic leaflets are

named in relation to the coronary arteries: left coronary, right coronary and noncoronary. This latter is usually larger than the other two cusps.

2.2.2 The sinotubular junction

The sinotubular junction (STJ) is a circular ring which separates the tubular portion of the ascending aorta from the aortic root. It lies at the level of the commissural apices and provides most of the support for the valve cusps and commissures. For this reason, its integrity is essential for the proper function of the valve as demonstrated by Thubrikar et al. (2005) [44].

2.2.3 The Valsalva sinuses

The Valsalva sinuses are dilations of the aortic root which are named, as the leaflets, according to the coronary arteries: left coronary, right coronary and noncoronary. In fact, the inlets to the coronary artery system can be found within the sinuses of Valsalva, superior to the leaflet attachments and inferior to the sinotubular junction. The two openings in the aortic sinus that mark the origin of the (left and right) coronary arteries are named "ostia" (see Figure 2.6).

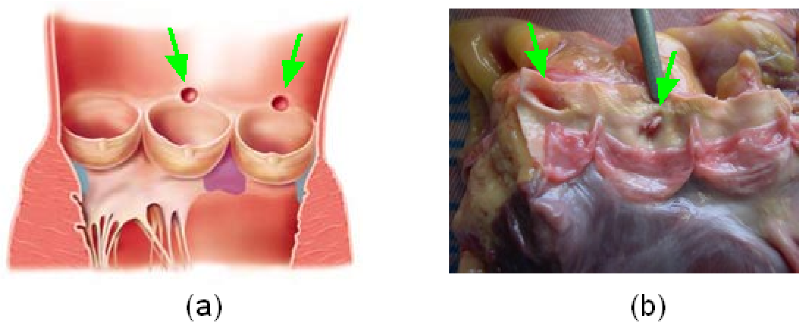

Figure 2.6 *Coronary ostia: (a) sketch of coronary ostia position [45] and (b) excised aortic root in which the two coronary ostia are highlighted [45].*

At the lower margin the sinuses become continuous with the left ventricle while at the upper margin they become part of the ascending aorta. Even though the three sinuses and the related leaflets play an identical function, their anatomical features differ [42]:

- the two coronary sinuses are mainly part of the aortic wall with crescents of ventricular muscle incorporated at the base of each of them, while,

- the noncoronary sinus is only made of fibrous wall. In fact, the base of this sinus is part of the mitroaortic continuity, which is a feature of the outflow tract of the left ventricle.

The Valsalva sinuses play a key role in the local hemodynamic forces that exert their effects on both leaflet motion and coronary flow; they generate a cavity behind the open leaflets preventing occlusion of the coronary orifices. Such a cavity favors the generation of “eddy currents”, described first by Leonardo da Vinci and additionally supported by Henderson and Johnson (1912) with their study addressed using hydrodynamic models to demonstrate that the closure of the aortic valve under pulsatile flow is a gradual process partially determined by the aortic sinuses shape [46].
The sinuses are also important for transmitting the stress from the leaflet to the aortic wall [17].

2.2.4 The interleaflet triangles

Beneath the apices formed by the lines of attachment of the leaflets to the aortic wall, the fibrous components of the aortic root exist. Although these areas are unequivocally a part of the aortic root, they are triangular extensions of the left ventricle outflow tract. Such areas, bounded by the semilunar attachments of the valvar leaflets, are named *interleaflet triangles*.

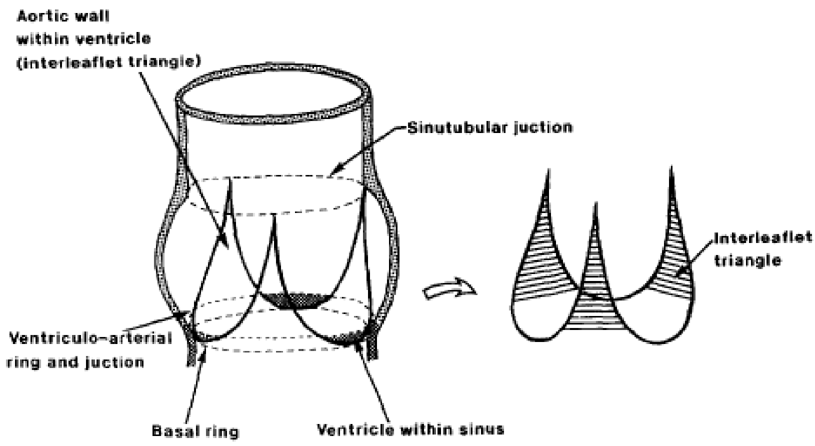

Figure 2.7 *Sketch of the aortic root: the interleaflet triangles are highlighted.*

Figure 2.7 adapted from Sutton et al. (2005) highlights the coronet-like shape formed by the interleaflet triangles.

2.2.5 The ventriculoaortic junction

The ventriculoaortic junction (AVJ) is composed of the cusp bases and the interleaflet triangles; the planar line passing through the inferior point of the attachment line of each leaflet and through the basis of each interleaflet triangle represents the ideal ring that is considered the so-called *aortic annulus*, routinely measured by imaging techniques. All structures that are distal (with reference to the heart) to the aorto-ventricular junction are subjected to arterial pressures, whereas those that are proximal are subjected to ventricular loads.

2.3 Histology and tissue biomechanics of the aortic root

The microscopic anatomy of cells and tissues is an important aspect to understand both the aortic valve physiological behavior and its pathological alterations.

The **aortic leaflets** are composed of three layers, the *ventricularis* and the *fibrosa* separated by a gelatinous *spongiosa*, as represented in Figure 2.8 adapted from [47]. The ventricularis faces the left ventricular chamber and it is composed of radially aligned elastin fibers and collagen fibers randomly distributed. The spongiosa mainly consists of glicosaminoglycans, proteoglycans and mucopolysaccharides that give it a soft consistency together with loosely arranged collagen fibers. Finally, the fibrosa consists of collagen fibers embedded in an elastin matrix and highly oriented in the circumferential direction, i.e., parallel to the annulus. Such a structural arrangement makes the fibrosa considerably stiffer in the circumferential direction giving to the leaflet the ability to withstand high cyclic mechanical loads [48].
The fibrosa and ventricularis are preloaded by virtue of their attachment to each other; the fibrosa under compression and the ventricularis under tension [47]. In general, the valve cusps contain about 50% collagen and only 13% elastin by dry weight [49]. Even though this would suggest that, relative to collagen, the contribution of elastin to valve leaflet mechanics is minimal, during diastolic loading, there is considerable realignment of collagen fibers as the cusps extend beyond 50% strain and recoil elastically. Since collagen on its own is not highly elastic, it has been hypothesized that aortic valve elastin is responsible for their elastic recoil. This implies that collagen extends passively through most of its elongation phase.

The majority of biomechanical measurements of the heart valve leaflets have been performed by means of uniaxial tests. However, biaxial tests are preferable since the effects of multiaxial collagen fiber distributions remain intact and testable. Generally, aortic valve cusps show non-linear behavior, different in circumferential and radial directions. In Figure 2.9, the mechanical

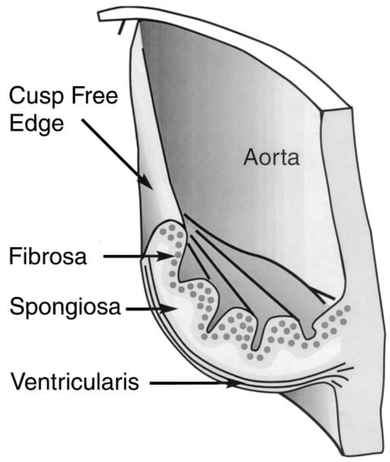

Figure 2.8 *Histology of aortic leaflet: the three layers constituting the cusp are highlighted [47].*

behavior of aortic leaflet tissue is represented in terms of stress-strain relationship [50].

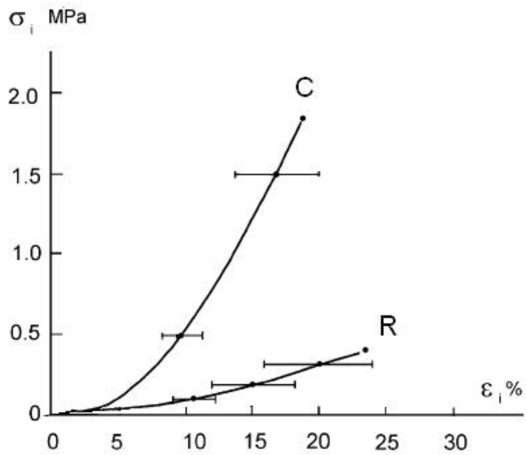

Figure 2.9 *Mechanical behavior of aortic leaflets: the stress-strain curve obtained by testing human specimens in circumferential (C) and radial (R) direction is represented [50].*

At the beginning of the loading of samples at low stress, the tissue extends very compliantly. During loading the wavy structure of tissue becomes straight, more fibers are recruited and, with increasing stress, the strain of the tissue decreases drastically. The high compliance at low strains and the high stiffness at high strains enables the tissue to be optimally flexible during systole and rigid during diastole [51].

The **sinotubular junction** is a circular structure of primarily elastic composition, but with important collagenous supports for the valvar leaflets [43].

The **Valsalva sinuses** are histologically similar to large arteries, with *intima*, *media* and *adventitia* layers. The *intima* is made up of the endothelium attached to a basement membrane and a thin layer of connective tissue; the *media* is formed by layers of smooth muscle cells scattered with elastic lamellae. The outer layer is the *adventitia* consisting mainly of loose connective tissue with some smooth muscle cells.

The biomechanical properties of Valsalva sinuses remain largely unknown, especially due to the fact that measuring their behavior is more challenging due to the non-planar nature of the tissue. Only recently, Martin et al. (2011) tested human aortic sinuses and compared their behavior with the one exhibited by porcine specimens [52]. As the aortic valve leaflets, the Valsalva sinuses show a nonlinear stress-strain behavior in the circumferential and longitudinal directions (see Figure 2.10).

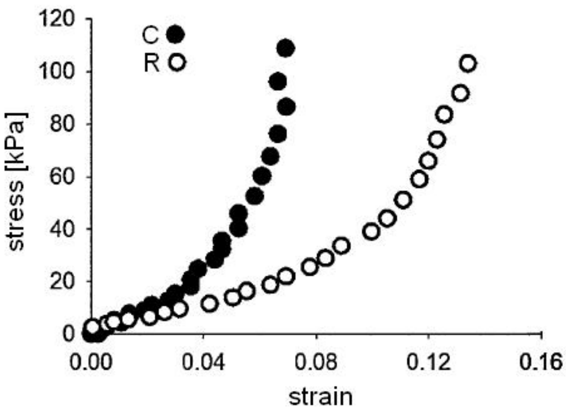

Figure 2.10 *Mechanical behavior of Valsalva sinuses: the stress-strain curve obtained by testing human specimens in circumferential (C) and radial (R) direction is represented [52].*

The **interleaflet triangles** have different characteristics from a microscopic point of view [42]:

- the triangle between the left and right coronary cusps is partially constituted of myocardial tissue;
- the triangle between the right coronary and noncoronary cusps is composed of a fibrous tissue and contains the atrioventricular bundle of the conduction axis;

- the triangle between the noncoronary and left cusps is only made of fibrous tissue.

In dealing with the histology of the **aorto-ventricular junction**, collagen is dense at the hinge point that constitutes the semilunar contour of the leaflet attachment.

2.4 Dynamics of the aortic root

The complex structure of the aortic root is always in motion due to the pumping action of the heart. The aortic valve opens during systole, when the ventricle is contracting and, then, closes during diastole, as the ventricle relaxes. During such motion, the leaflets are not the only actors but all the surrounding structures and valvular components interact in a complex but functionally efficient manner.
Aortic valve dynamics has been studied using different techniques: either injecting a radiopaque dye and visualizing the movement under X-ray [53] or by means of two-dimensional echocardiography [54] or using marker-fluoroscopy technique [55]. Moreover, valve motion has been also studied *in vitro* using pulse-duplicator systems [56].
The aortic valve opens rapidly at the beginning of systole and closes rapidly at the end of systole. The consecutive phases of aortic valve motion during a cardiac cycle can be summarized as follows: a sudden opening of the valve, just a little movement while the valve remains open, a sudden closure of the valve and almost no movement while the valve remains closed. During a cardiac cycle the most of the time is spent to fill the heart with blood during diastole and eject it during systole [17].
Although the leaflets are the most flexible and dynamic parts, the motions of the other components of the aortic valve are also important.
Thubrikar et al. (1986) studied the movement of the commissures in dogs by placing radiopaque markers at appropriate positions of the aortic root and recording their movement under X-ray [55]. The commissures move outward during systole and inward during diastole. As depicted in Figure 2.11, the commissure motion follows the aortic pressure curve closely. They measured the commissural perimeter (i.e., the perimeter of a triangle formed by the commissural markers) recording an increase from diastole to systole of about 12%.
During the cardiac cycle, the aortic valve annulus expands and contracts, too. Both using echocardiography and angiography the base of the aortic valve has been shown to change diameter and dimensions during the cardiac cycle. It is maximally dilated during valve opening and maximally contracted at the time of valve closure. The percentage of change in base perimeter is approximately 20%.

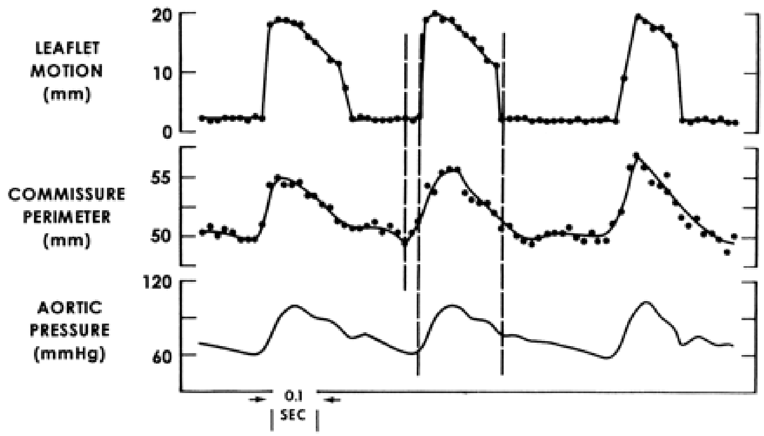

Figure 2.11 Aortic valve dynamics: plot of the leaflet motion, commissural perimeter and pressure in the ascending aorta adapted from [57].

2.5 Pathologies of the aortic root

As previously mentioned, aortic valve function has been shown to depend on the complex anatomic and dynamic relationship of aortic valve and root. As a consequence, any morphological, structural and histological alterations of valve components may lead to valve disfunction. Even though there exist several diseases which can cause malfunctioning of aortic valves, the most common ones being, rheumatic valve disease, infective endocarditis, calcifications, aortic aneurysm and congenital anomalies, we may distinguish two main families of aortic valve pathologies: stenosis, i.e., restricted opening, producing pressure overloading and insufficiency or regurgitation, i.e., inadequate valve closure inducing volume overloading.

2.5.1 Aortic stenosis

Aortic stenosis refers to an obstruction of flow at the level of the aortic valve. In particular, there are mainly three causes of aortic valve stenosis: (i) calcifications related to atherosclerosis, which can be roughly defined as an inflammatory disease impairing valve patency; (ii) endocarditis, that is an infection caused by the presence of bacteria in the bloodstream and bacterial vegetations on valve leaflets; (iii) congenital diseases and, in particular, bicuspid aortic valve, which consists in the fusion of two leaflets.
Congenital bicuspid aortic valve and calcific aortic occlusion account for the majority of aortic stenosis cases.
In the first case, bicuspid valves (see Figure 2.12a) are characterized by the fusion of two of the three leaflets, most commonly the left and right, and they present raphe, leaflet doming and eccentric closure under echocardio-

graphy. There is some variation in incidence from about 0.4% to 2.25% [58]. In the second case, calcific aortic stenosis (see Figure 2.12b), usually referred to as "degenerative" pathology, affects, according to the work by Stewart et al. (1997) approximately 25% of the population older than 65. For these patients, echocardiography showed leaflet thickening or calcification, or both, and the prevalence increased with advancing age [59].

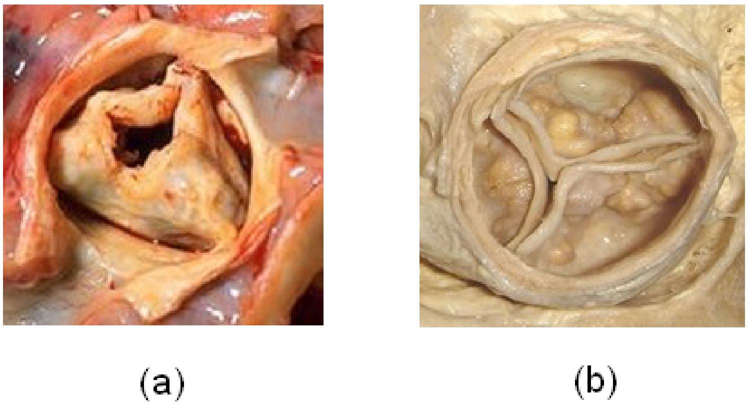

Figure 2.12 *Aortic valve stenosis: (a) due to bicuspid aortic valve degeneration [60]; (b) due to severe calcifications of a trileaflet valve [61].*

Severe aortic stenosis is usually surgically treated. Either biological valves or mechanical valves may be used to replace the stenotic native valve; for elderly patients, innovative transcatheter aortic valves may be implanted which do not require open-heart surgery and cardiopulmonary bypass.

2.5.2 Aortic regurgitation

Aortic regurgitation is defined by incompetence of the aortic valve, in which a retrograde blood flow from the aorta to the left ventricle originates during diastole.
Infective endocarditis involving the aortic valve as well as rheumatic fever associated with chronic inflammatory aortic valve disease may result in aortic regurgitation because of loss of coaptation, leaflet retraction, or perforation. If, on one side, aortic stenosis is only related to diseased valve leaflets, aortic regurgitation may depend either on valve leaflets or on other components of the aortic root. In particular, pathologic dilations of the aortic annulus or of the Valsalva sinuses, or both, as well as an abnormal enlargement of the sinotubular junction (see Figure 2.13) may cause aortic regurgitation.
All of these morphological alterations of the aortic root may be related either to atherosclerotic and/or hypertensive damage of the aortic wall or to

heritable connective tissue disease (like Marfan syndrome or Loeys-Dietz syndrome).

Figure 2.13 *Aortic valve insufficiency may be caused by a severe dilation of the proximal ascending aorta: a significant enlargement of the Valsalva sinuses and of the first tract of the ascending aorta is shown (picture adapted from [42]).*

In presence of aortic insufficiency, a volume overloading of the left ventricle occurs. The volume overload may be slow and well tolerated for long periods. The consequences of aortic insufficiency include left ventricular dilation and hypertrophy, with remodeling of the left ventricle [62].
Severe aortic regurgitations generally require surgical treatments. In particular, if the native aortic leaflets are healthy, aortic valve sparing techniques (which are cardiac surgical procedures involving replacement of the aortic root without replacement of the aortic leaflets) may be adopted. Otherwise, the whole aortic root can be substituted with biological or mechanical valves sewn into appropriate grafts.

2.6 Diagnostic tools for the aortic root

Several imaging techniques may be adopted to investigate aortic root morphology and functionality. Echocardiography, computed tomography and magnetic resonance are the major players in diagnosing, monitoring, and decision making for optimal surgery in aortic root pathology.

2.6.1 Bidimensional echocardiography

Bidimensional echocardiography represents a frequently used and widely accepted imaging methodology to identify and investigate aortic root pathologies [63]. Echocardiography, also known as *cardiac ultrasound*, uses standard ultrasound techniques to image two-dimensional slices of the heart.
At present, echocardiographic investigations may provide both morphologic and hemodynamic information. In addition to 2D pictures highlighting dimensions and morphology of each component of the aortic root, echocardiography can also provide measures of the velocity of blood as well as information about the cardiac tissue at any arbitrary point. Moreover, continuous wave Doppler ultrasound allows the investigation of cardiac valve areas and function so to determine, for example, any leaking of blood through the valves (valvular regurgitation). Additional routine information includes any abnormal communications between the left and right side of the heart and calculation of the cardiac output as well as of the ejection fraction. Peak ejection velocity, effective valve orifice area and mean transvalvular pressure gradient are the three main hemodynamic indices which are combined to determine the severity of valve dysfunction.

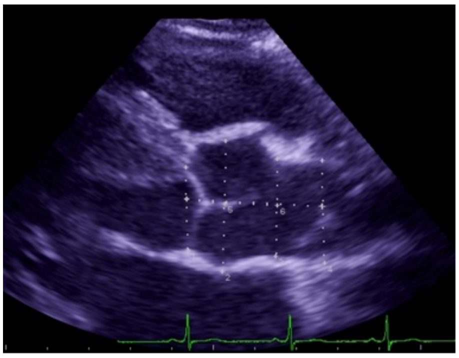
(a)

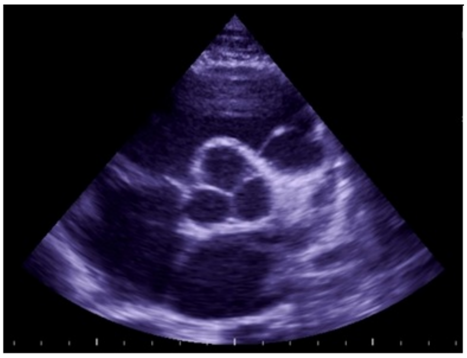
(b)

Figure 2.14 *Transthoracic echocardiography of the aortic root: (a) parasternal long-axis; (b) parasternal short-axis.*

In Figure 2.14 an example of transthoracic echocardiography of the aortic root is represented.
The principal advantages which make echocardiography a standard diagnostic technique in cardiovascular medicine are: (i) safety for the patient since it does not require use of contrast dye and emission of radiations; (ii) high temporal resolution: the image acquisition is fast and allows the documentation of dynamic phenomena as the opening and closing of heart valves.
On the contrary, the main drawbacks associated with cardiac ultrasound lie in the fact that: (i) it is an extremely operator-dependent methodology; (ii)

the accuracy of measurements is not particularly high. Moreover, to reproduce the real morphology of the aortic root under investigation is necessary to look at different views and projections (e.g., long-axis and short-axis).
Two main approaches may be adopted to investigate the aortic root by means of 2D echocardiography: *transthoracic* and *transesophageal* [64].
In the first case, the echocardiography transducer (or probe) is placed on the thorax of the subject, and images are taken through the chest wall. This is a non-invasive, highly accurate technique providing quick assessment of the overall health of the heart.
In the second case, the probe is inserted through the patient's esophagus. Transesophageal echocardiography provides a highly accurate anatomic assessment of all types of aortic regurgitation lesions [65].

2.6.2 Computed Tomography

A computed tomography (CT) scanner uses X-rays, a type of ionizing radiation, to acquire images, making it a good tool for examining tissue composed of elements of a higher atomic number than the tissue surrounding them, such as bone and calcifications within the body.
To study blood vessels and, in general, components of the cardiovascular system, intravenous injections of specific contrast dye are used. Contrast agents for CT contain elements of a high atomic number, relative to tissue, such as iodine or barium.
In Figure 2.15, an example of CT-image of the aortic root is represented.

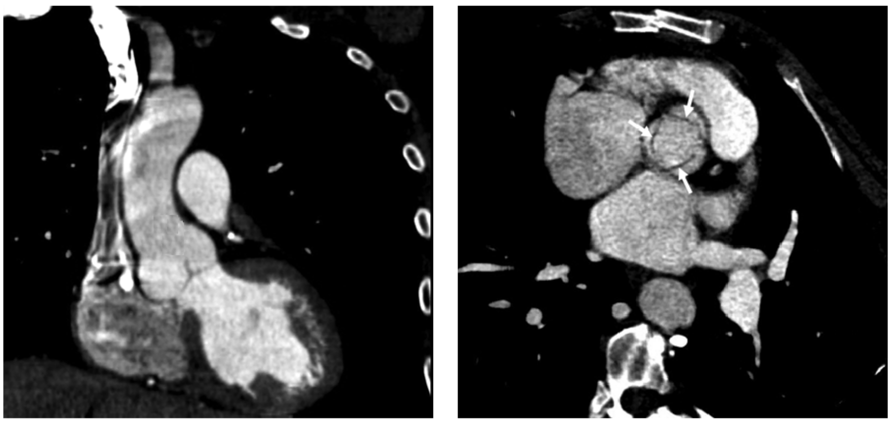

(a) (b)

Figure 2.15 *CT-images of the aortic root: (a) long-axis; (b) short-axis. Both of them are taken from [66].*

A ring incorporating one or more X-ray sources and opposing detectors is rotated rapidly around the patient, producing and, then, reconstructing into

an image the projections from multiple fan beams. The patient is moved axially through the donut-shaped scanner; during the movement, equally spaced two-dimensional cross sections (slices) are taken which allow a volumetric tridimensional reconstruction.
CT measurements of the thoracic aorta should be performed using an electrocardiogram to synchronize detection with the heart-beat. In this way, precise measurements are possible; in particular, CT images provide precise diameters of (i) the ventriculoaortic junction, (ii) root at the level of the Valsalva sinuses, (iii) sinotubular junction, (iv) ascending aorta. Moreover, qualitative information on cusp morphology, symmetry of the sinuses, linearity or tortuosity of vessels may be obtained [42].

2.6.3 Magnetic Resonance

The main difference between CT and magnetic resonance (MR) is that this latter uses non-ionizing radio frequency (RF) signals to acquire images and does not require iodinated contrast procedure. MR is best suited for soft tissue, although it can also be used to acquire images of bones, and other calcium-based body components.
A magnetic resonance imaging (MRI) machine uses a powerful magnetic field to align the magnetization of some atoms in the body, and radio frequency fields to systematically alter the alignment of this magnetization. This causes the nuclei to produce a rotating magnetic field detectable by the scanner and this information is recorded to construct an image of the scanned area of the body [67].
In Figure 2.16 an example of MRI of the aortic root is shown.

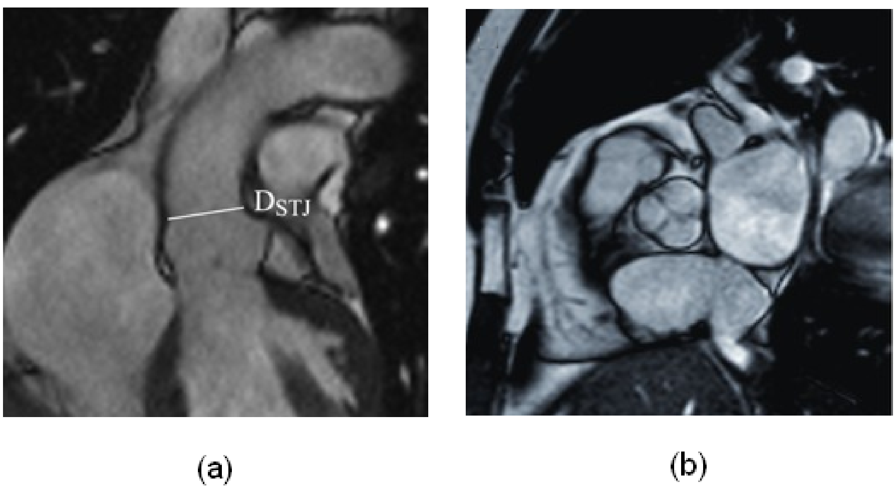

Figure 2.16 *MR-images of the aortic root: (a) long-axis [36]; (b) short-axis [68].*

MR images are acquired in frequency space and images are obtained by inverse Fourier transforms; relatively long time scans are required to traverse the whole frequency space. Patient motion becomes a challenge since it produces non-intuitive artifacts in the transformed image.
Particular care must be taken in choosing the image resolution: too coarse and the blood signal is weakened by phase dispersion caused by the presence of large velocity gradients; too fine and there are not enough protons to return adequate signal, thus necessitating longer scan times and/or thicker slices [40].
With respect to echocardiography, MRI provides more accurate images and, consequently, more precise measurements are possible.

Chapter 3

Finite element analysis of the aortic valve

As previously mentioned in Chapter 1, in the last thirty years, many computational studies have been addressed to investigate the aortic valve and, in particular, finite element analyses have been performed to virtually reproduce its behavior.
Briefly stated, all the physical phenomena are described by partial differential equations (PDE) but, usually, it is not possible to solve them analitically. For this reason, the finite element method (FEM) has been introduced as a numerical technique for finding approximate solutions of PDE.
The basic idea of FEM is to divide a continuum body (e.g., in our specific case, the aortic valve) into discrete *finite elements* connected by nodes (see Figure 3.1). The approximate solution of the entire continuum (e.g., the aortic valve behavior), is then obtained from the assembly of all the individual elements and computed by a computer program.

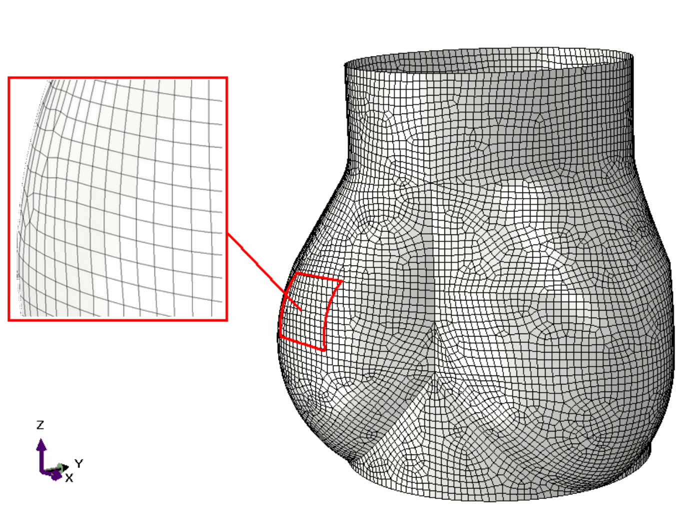

Figure 3.1 *An example of aortic valve mesh made of finite elements and nodes.*

In particular, the ultimate goal of the doctoral research is to predict by means of finite element analyses the postoperative performance of the aortic valve, following different interventional approaches related to different pathologic conditions.
To achieve the goal and obtain realistic results, particular attention has been payed to each aspect of a finite element model. In the following, all the main prerequisites needed to set up a proper finite element model of the aortic valve are discussed. In particular, the geometry of the valve, the material models and the boundary conditions are described in detail.

3.1 Aortic valve geometry

The aortic valve anatomy is quite complex: it is not a trivial issue to obtain appropriate geometrical descriptions of the valve. We may distinguish between two main methodologies leading to a geometrical representation of the aortic valve that we name *partially patient-specific* and *fully patient-specific*. In the first case, the valve geometry is obtained by measuring few characteristic dimensions which represent the input data of predefined geometrical operations while, in the second case, the geometry of the valve is completely reconstructed by processing medical images.

3.1.1 *Partially patient-specific* valve models

The main dimensions of the aortic valve can be measured from all the diagnostic techniques discussed in section 2.6 but only with MRI and echocardiography it is possible to measure the valve leaflets while with CT-A is quite challenging. In particular, echocardiography represents the most routinely adopted methodology mainly due to its advantages such as safety of the patient, reduced execution times, high temporal resolution, absence of significant counter-indications.
Moving from bidimensional echocardiographic images, we may model the whole aortic root; in the following, we treat separately the valve leaflets and the sinuses describing the modeling procedure of both.

Modeling aortic valve leaflets

Recently, the geometric modeling of the aortic leaflets has received considerable attention [17, 26, 29, 69]. In our work, we move from the model by Thubrikar (1990) and Labrosse (2006) to develop a new improved framework which takes into account also valve asymmetry.
Thubrikar explored the geometry of trileaflet valves and proposed a design methodology to ensure optimal performance. Specifically, geometric criteria were defined (i) to guarantee appropriate coaptation of the leaflets in closed position, (ii) to minimize the dead space, (iii) to avoid folds in the leaflets

and (iv) ensure a minimum leaflet flexion to make the use of energy as efficient as possible.
The design of the aortic valve derives from five parameters, all highlighted in Figure 3.2:

- radius of the base, R_b;
- radius of the commissures, R_c;
- valve height, H;
- height of the commissures, H_s;
- angle of the open leaflet to vertical, β.

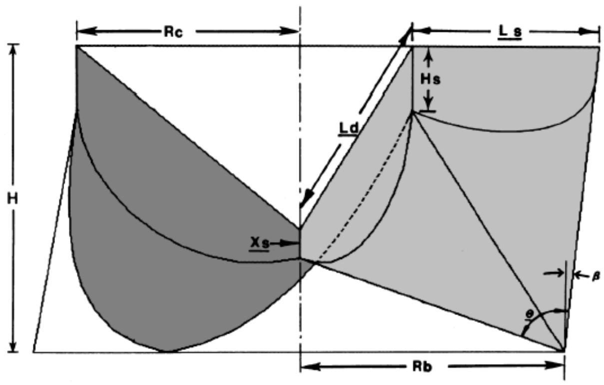

Figure 3.2 *A schematic drawing of the aortic valve highlighting the design parameters of the model by Thubrikar [17].*

The approach proposed by Thubrikar has been considered too rigid to accommodate the dimensional variability observed in normally functioning valves [70].
For this reason, Labrosse et al. (2006) incorporated dimensional variability into their model (after documenting it by means of measurements from silicone rubber molds of normal human adult aortic valves) adopting an analytical approach to implement basic design principles and determine which dimensions are satisfactory and which are not [26].
The model due to Labrosse is based on some simplifying assumptions: (i) the three leaflets are identical in size and properties, and lie at 120° from each other in the circumferential direction of the valve; (ii) the planes going through the base of the valve and the top of the commissures are parallel; (iii) the dimensions of the valve components do not change significantly enough during the cardiac cycle so that their variation should be accounted for in a first-order analysis. According to such a design framework, the fundamental parameters are again five:

- the diameter of the base, D_b;
- the diameter of the commissures, D_c;
- the valve height, H;
- the leaflet free edge (or free margin), L_{fm};
- the leaflet height, L_h.

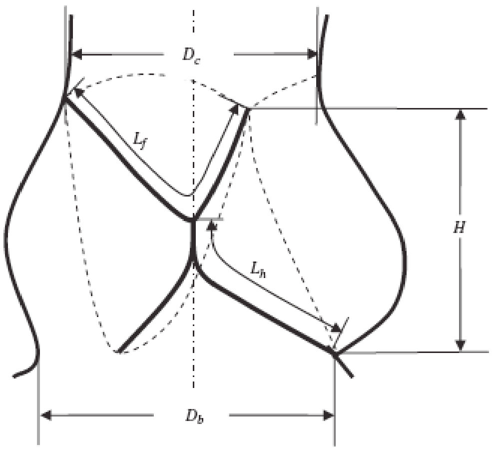

Figure 3.3 *A schematic drawing of the aortic valve highlighting the design parameters of the model by Labrosse [26].*

In Figure 3.3 the design parameters are shown.
The physiologic aortic valve has in the majority of cases an asymmetric geometry [71] which also results in asymmetric stress distributions in the leaflets and root sinus walls [72]. Consequently, the Labrosse model has been improved by removing the first simplifying assumption previously recalled, i.e., including the possibility of modeling three leaflets of different sizes, lying at angles not necessarily equal to 120°.
An asymmetric parametrical model of the aortic valve in both the open and closed configuration has been realized using the CAD software Rhinoceros v.4 (R. Mc Neel & associates, Seattle, WA, USA).
In addition to the parameters required by the Labrosse model, also the three characteristic leaflet angles (α, β and γ in Figure 3.4a) and the three eventually different values of the free margin (L_{fm1}, L_{fm2} and L_{fm3}) represent input values for the improved geometrical model.
The main geometrical operations are briefly listed below.

1. A truncated cone is created whose dimensions are: the diameter of the base, D_b, the diameter of the commissures, D_c, and the height $H-H_s$,

where H is the valve height and H_s is the length of the line connecting the apices of the interleaflet triangles and the commissures (see Figure 3.2). Finding the maximal coaptation height at the hinge point (i.e., H_s) is quite challenging. We choose to obtain that measure by scanning the long-axis projection of the aortic root with the echo scan from one side to the other. The first image in which the coaptation between the cusps is recognized to move away from the Valsalva sinus wall is assumed to be a realistic approximation of H_s.
The truncated cone is represented in Figure 3.4.

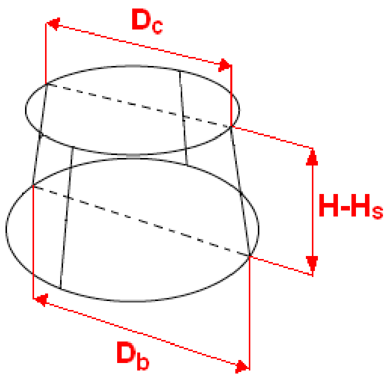

Figure 3.4 *Aortic valve model, first step: a truncated cone is created.*

2. The information about the three characteristic angles of each leaflet is included in the model by drawing three points (blue markers in Figure 3.5) properly spaced on the circumference of the base, which identify the tangency of each leaflet with the annulus and other three points (red markers in Figure 3.5) properly spaced on the circumference at the top, which identify the apexes of three interleaflet triangles.

3. Three planes (e.g., π in Figure 3.6a) passing through three points (e.g., A', B' and A) are created to define the line of leaflet attachment (highlighted in Figure 3.6b) from the intersection between each plane and the truncated cone.

4. The apexes of the interleaflet triangles (A', B', C') are projected vertically to define the three commissures (A'A", B'B", C'C") so that the valve height is equal to H.

5. Three arch of circumference, lying in the plane defined by the three commissures, are drawn; they take origin at the commissural points and their length is equal to L_{fm1}, L_{fm2} and L_{fm3}, respectively. Finally, the surface of each leaflet is defined.

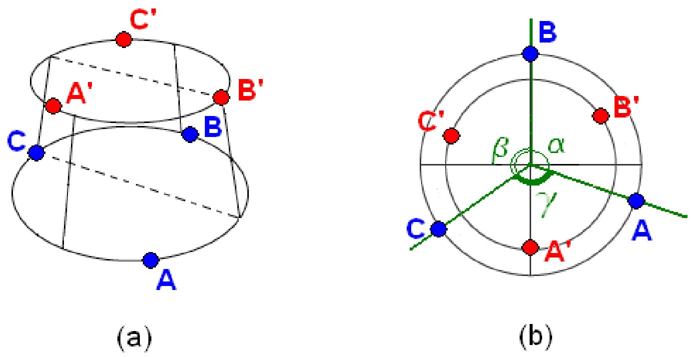

Figure 3.5 *Aortic valve model, second step: properly spaced points are identified to take into account the characteristic angles of each leaflet. (a) Perspective view; (b) top view.*

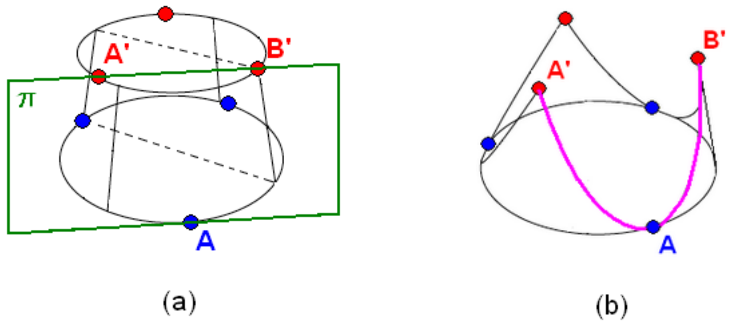

Figure 3.6 *Aortic valve model, third step: the line of leaflet attachment is defined from the intersection between the plane π and the truncated cone. (a) The plane π is represented; (b) the obtained line of attachment is highlighted.*

The closed configuration of valve leaflets moves from the obtained open one and it follows Thubrikar's geometrical guidelines. For the closed valve an additional parameter has to be measured, i.e., the length of central coaptation, X_s.
An example of the geometrical model of the aortic valve in the closed configuration is shown in Figure 3.9a,b.
In the following, we report an example of aortic valve model in the closed configuration which is obtained from measurements of a real case [1]. In Figures 3.10, 3.11 and 3.12 the measured dimensions required for the aortic valve modeling are highlighted on the echocardiographic images.

[1] The transthoracic echocardiographic images have been provided by Dr. Fabiana Gambarin of the Centre for Inherited Cardiovascular Diseases - IRCCS Policlinico San Matteo - Pavia - Italy

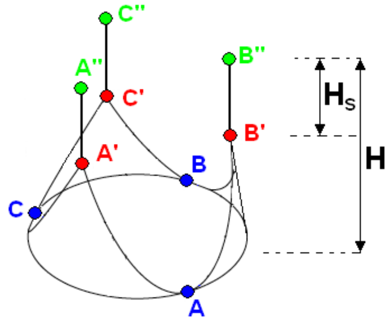

Figure 3.7 *Aortic valve model, fourth step: the apices of the interleaflet triangles are projected vertically to define the three commissures.*

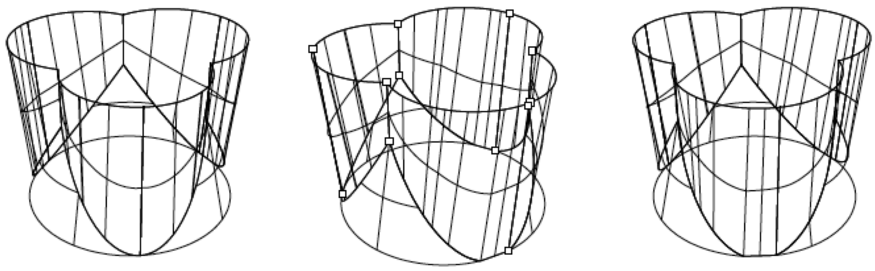

Figure 3.8 *Aortic valve model, fifth step: the leaflet free margins are created and the surface of each leaflet is defined.*

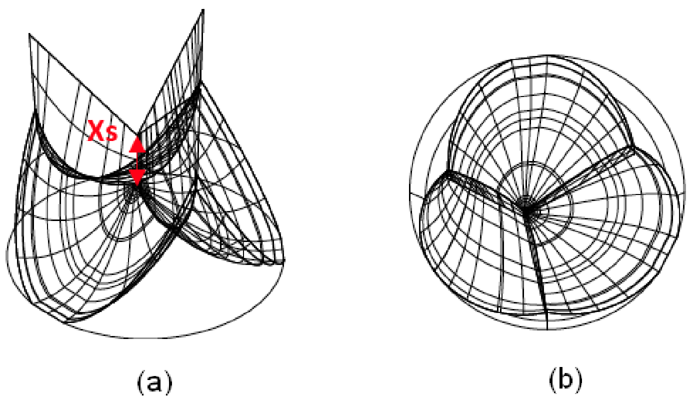

Figure 3.9 *Aortic valve model in the closed configuration: (a) perspective view highlighting the parameter X_s; (b) top view which emphasizes the valve asymmetry.*

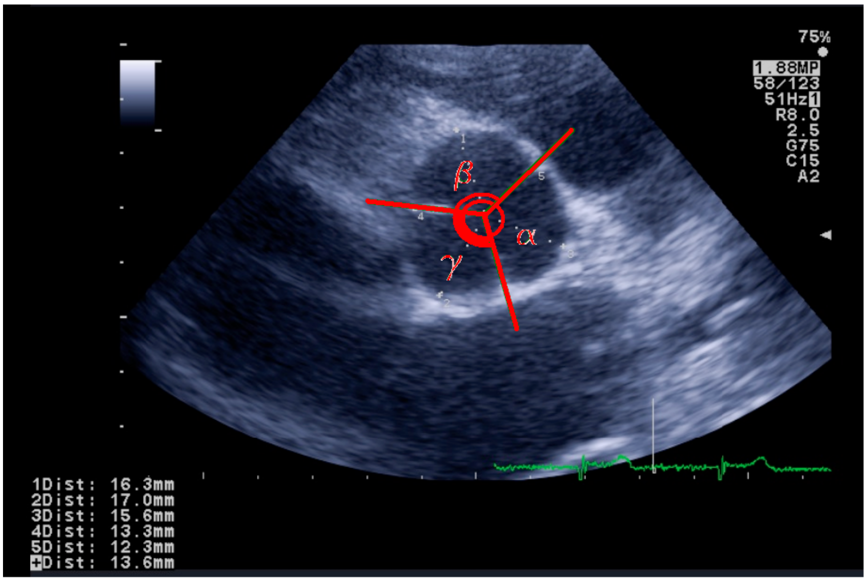

Figure 3.10 *Echocardiography of the aortic valve, short-axis: the three characteristic angles of each leaflet are highlighted.*

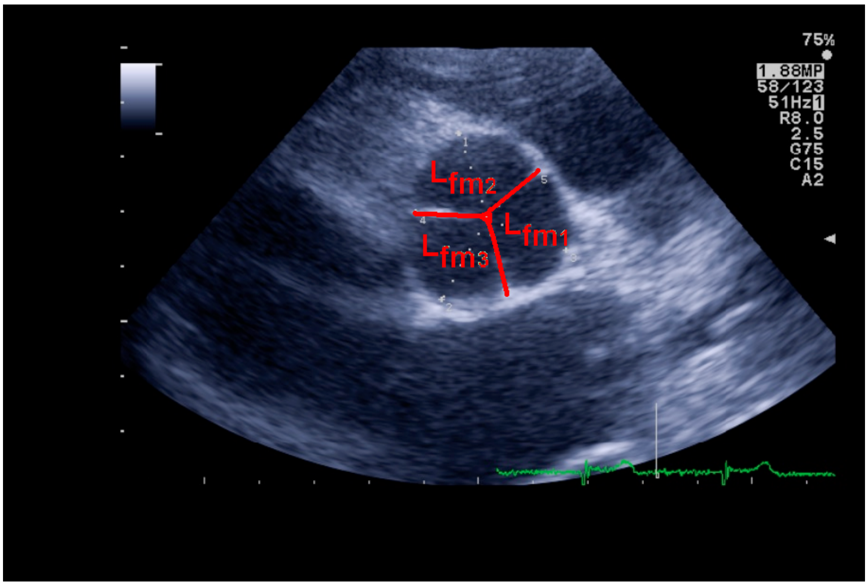

Figure 3.11 *Echocardiography of the aortic valve, short-axis: the leaflet free margins are highlighted.*

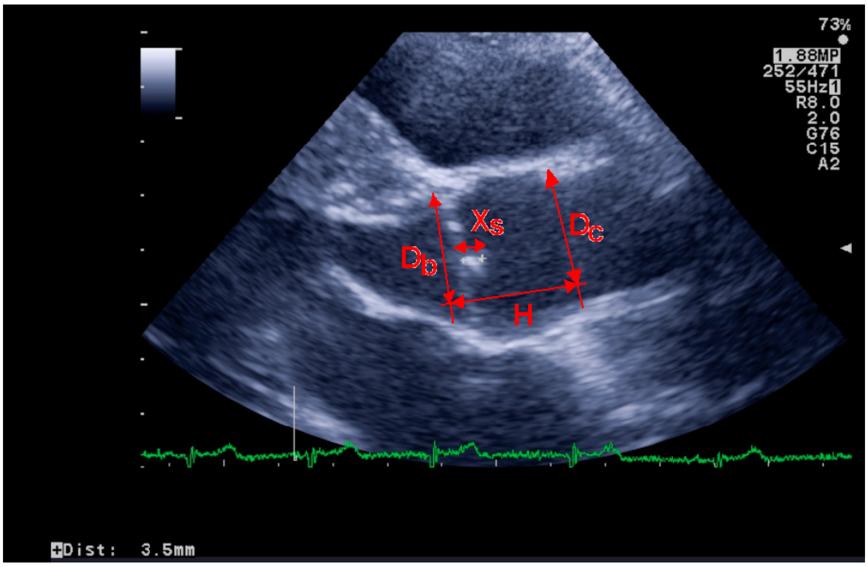

Figure 3.12 *Echocardiography of the aortic valve, long-axis: the base diameter, D_b, the diameter of the commissures, D_c, the valve height, H and, the central coaptation length, X_s, are highlighted.*

The correspondence with the patient's valve can be partially evaluated by overlapping the created model with the echocardiographic image. In Figure 3.13, a top view of the aortic valve model in the closed configuration has been superimposed to the short-axis echocardiographic image.

Modeling aortic sinuses

Starting from few basic measurements of echocardiographic images of the aortic valve, it is also possible to generate an approximated tridimensional geometrical model of the aortic sinuses. The modeling procedure has been performed again within Rhinoceros v.4; as in the case of the aortic leaflets, a program to automatically execute all the geometrical operations have been coded.
The geometrical operations to get a 3D model of the aortic sinuses are briefly described step by step:

1. moving from the simplifying assumption that both the annulus and the sinotubular junction are circular, the first step is to create two circles with a diameter of D_b and D_{STJ}, respectively, placed at a distance of H.

   In Figure 3.14 a sketch of the first step for modeling the sinuses is represented with the correspondent echocardiographic measurements.

2. At the intermediate height of H_{sin} (highlighted in Figure 3.15) the cross-section of the aortic sinuses is created. To complete the second

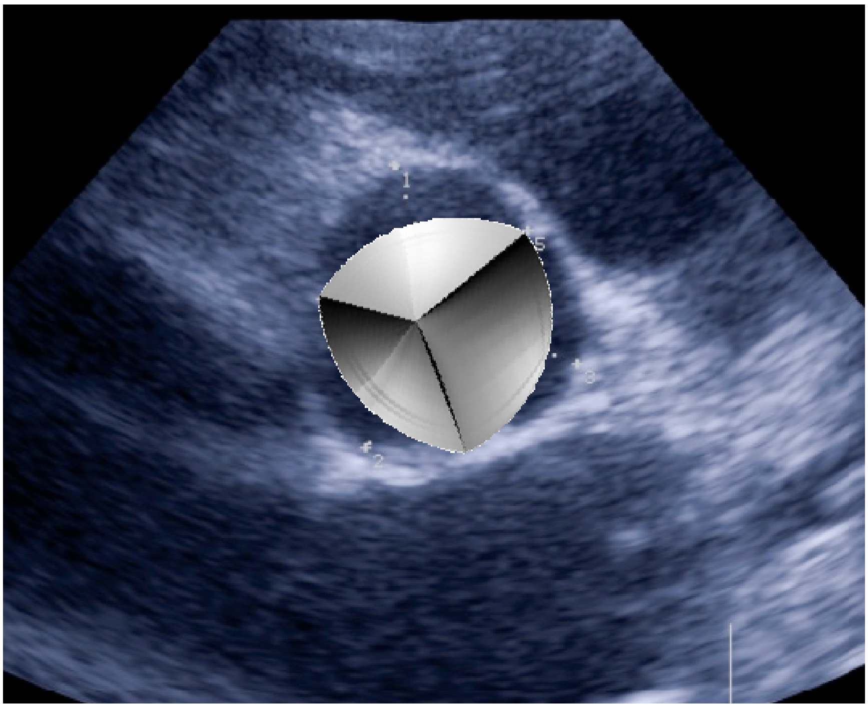

Figure 3.13 *The aortic valve model in the closed configurations obtained from real measurements is overlapped with the correspondent short-axis echocardiographic image: we can speculate that the correspondence is satisfactory.*

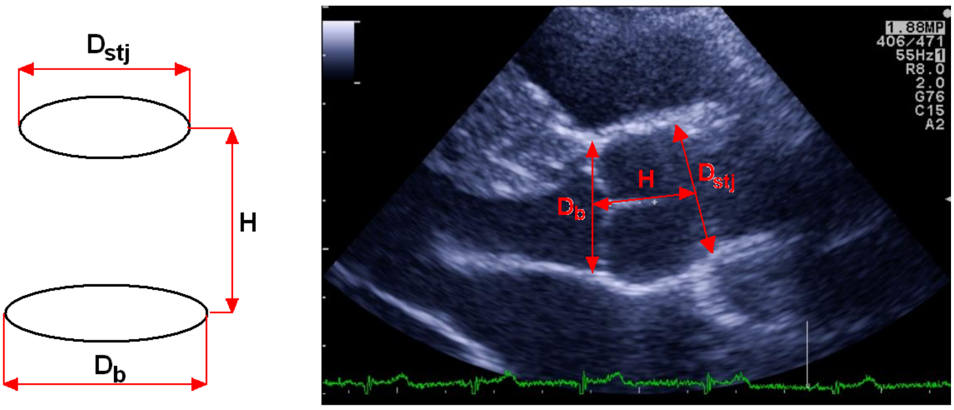

Figure 3.14 *Aortic sinus model, first step: the annulus and the sinotubular junction are assumed as circles lying in parallel planes with a diameter of D_b and D_{STJ}, respectively.*

step, the characteristic angles of the three sinuses (α, β, γ, δ, ε) as well as their main dimensions (A, B, C, D, E, F) are evaluated from the short-axis image (see Figure 3.16).

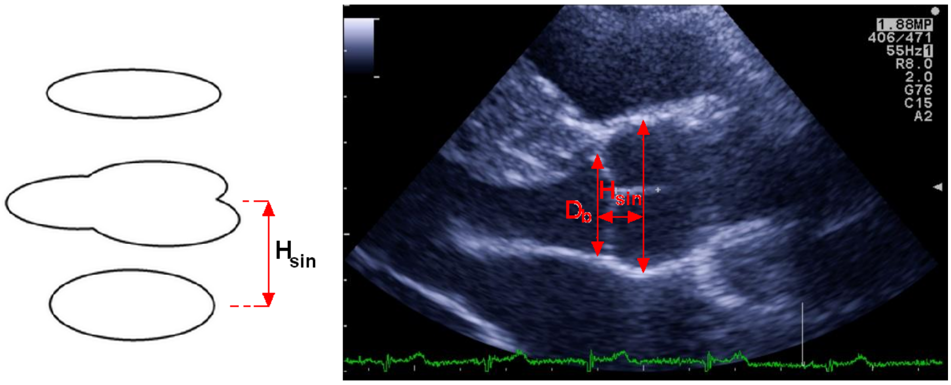

Figure 3.15 *Aortic sinus model, second step: at a distance of H_{sin} the cross section of the three sinuses is created.*

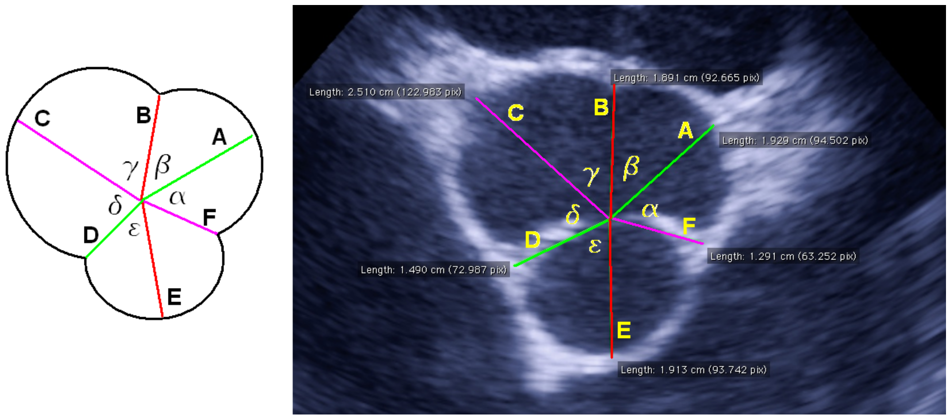

Figure 3.16 *Aortic sinus model, second step: the cross section of the sinuses is based on the measures of the angles α, β, γ, δ, ε and of the length A, B, C, D, E, F.*

3. A certain number of intermediate cross-sections are defined as depicted in Figure 3.17a; in particular, in order to guarantee a smooth and enough regular shape of the sinuses, we assume that the gradual enlargement/reduction from section to section is governed by a quartic polynomial which ensures a null tangent both at the level of the maximum expansion of the sinuses and at the sinotubular junction.

   The sinuses are then created by means of a lofting procedure (see Figure 3.17b).

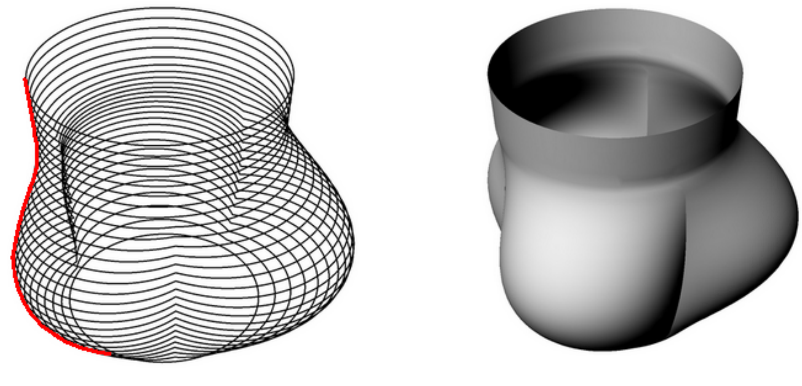

Figure 3.17 *Aortic sinus model, third step: (a) intermediate sections, whose dimensions are controlled by a quartic polynomial (red curve), are generated; (b) the sinuses are then obtained through a lofting procedure.*

4. Finally, the measure of H_s (again computed following the geometrical equations proposed by Labrosse) enables the definition of the interleaflet triangles which are represented in Figure 3.18.

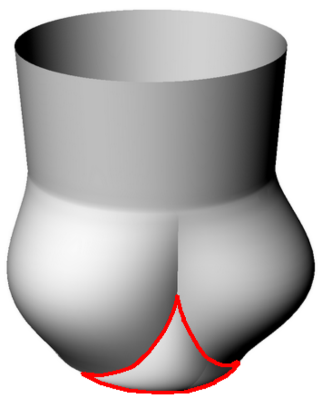

Figure 3.18 *Final 3D model of the aortic root: the interleaflet triangles are highlighted.*

In the following, the results of the described modeling procedure, obtained starting from two real cases, are presented.
The created geometrical models provide an easy and rapid off-line 3D reconstruction of the geometrical relationships of normal aortic root, including the physiologic asymmetry and variability that is seen in the daily clinical practice from case to case. The 3D reconstructions which start from few simple 2D transthoracic echo measures easily available during routine echo

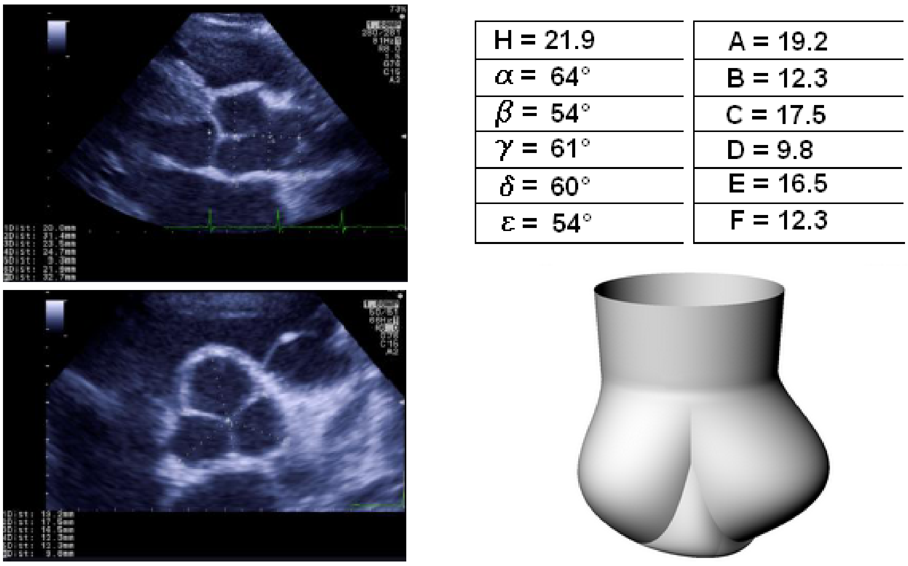

H = 21.9	A = 19.2
α = 64°	B = 12.3
β = 54°	C = 17.5
γ = 61°	D = 9.8
δ = 60°	E = 16.5
ε = 54°	F = 12.3

Figure 3.19 *First example of 3D aortic sinus reconstruction from 2D echocardiographic images: the short and long-axis images, the measured dimensions and the obtained model are represented.*

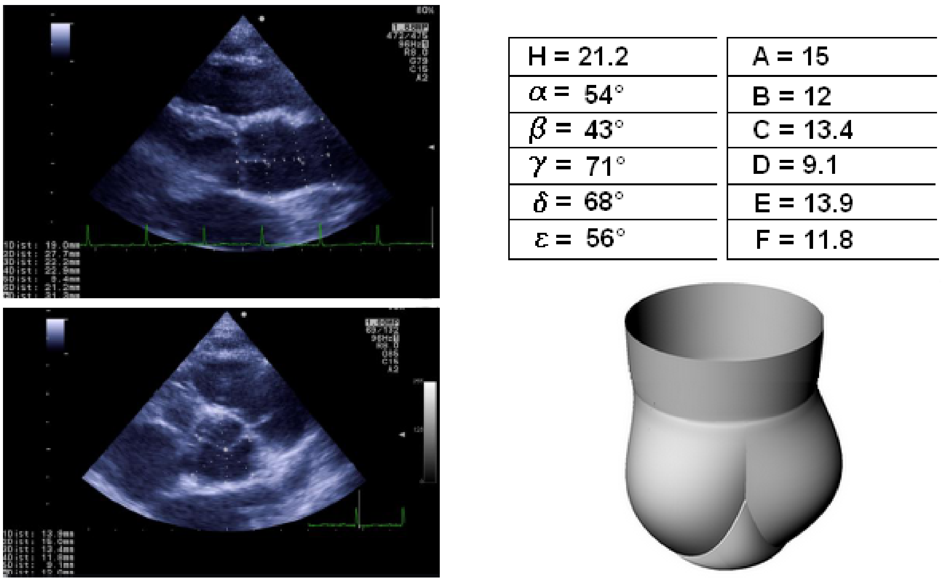

H = 21.2	A = 15
α = 54°	B = 12
β = 43°	C = 13.4
γ = 71°	D = 9.1
δ = 68°	E = 13.9
ε = 56°	F = 11.8

Figure 3.20 *Second example of 3D aortic sinus reconstruction from 2D echocardiographic images: the short and long-axis images, the measured dimensions and the obtained model are represented.*

examination are able to represent a source of information much more accessible to general users and to heart surgeons, independently from echocardiographist's interpretation.
Moreover, the CAD models of the aortic leaflets and sinuses obtained using Rhinoceros may be exported as IGES files which are compatible with finite element softwares. The meshing procedure is performed within the finite element codes and preprocessors (e.g., Abaqus, LS-PrePost, etc...).

3.1.2 *Fully patient-specific* aortic valve models

The development of parametrical models to reconstruct the aortic valve geometry on the basis of few measurements taken from bidimensional medical images carries several advantages such as reduced modeling time as well as high applicability since either CT or MRI or 2D-echocardiography may be used as data-source for the modeling procedure. Most important, the possibility of starting from echocardiographic images represents a key-aspect of such a procedure since echocardiography is the standard, more routinely adopted technique for aortic valve disease.
However, in some cases, the inevitable inaccuracy associated with a model based on few parameters may be not acceptable and a *fully patient-specific* model may be preferable. In fact, in this case, since the achieved 3D model is completely reconstructed from medical images and no predefined geometrical operations are performed, its accuracy is very high.
Both MRI and CT reconstructions are possible while, in this case, 2D-echocardiography cannot be used. We focus on computed tomography-angiography (CT-A), which is a particular CT technique devoted to study blood vessels and the circulatory system in general.
The principle drawback related to CT is that the procedure to obtain 3D reconstructions of the aortic valve leaflets is sometimes impossible or, at least, extremely difficult and time-consuming. On the contrary, 3D models of the aortic root wall are possible and accurate.

Aortic root wall reconstruction

In Figure 3.21 the methodological framework to obtain analysis suitable models (e.g., a finite element mesh for finite element simulations) is summarized.
The outcome of the CT-scan consists of DICOM images which are a standard for handling, storing, printing, and transmitting information in medical imaging.
The DICOM files are then processed to extract a 3D model of the anatomical part of interest. In particular, segmentation, contrast enhancement and filtering operations have to be performed using appropriate tools. In this

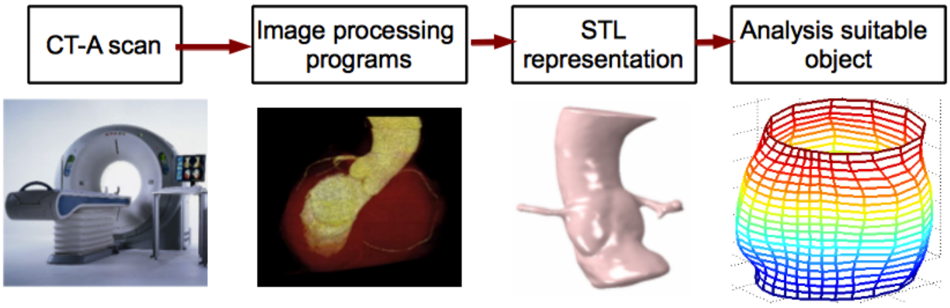

Figure 3.21 *Image processing framework: from CT-scan to computational analysis.*

sense, OsiriX is a free software, available on the web and well-known among physicians, which allows three dimensional volumetric information [73] but many other software are available to generate 3D representations of the anatomical district of interest. Among the others, ITK-Snap is a capable tool which allows 3D reconstructions based on the *snake evolution* technique [74].

Figure 3.22 adapted from [42] shows both the short-axis planes of an aortic root and the reconstructed three dimensional anatomy.

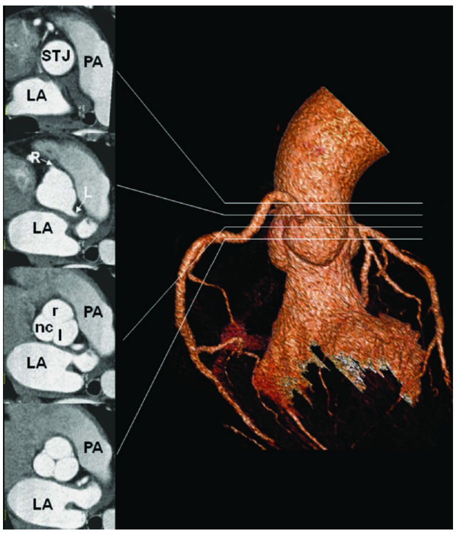

Figure 3.22 *Short-axis slices obtained by a CT-A scan and the reconstructed three dimensional volume of the aortic root.*

The obtained 3D description of the aortic root is then exported as a stereolithographic file (STL) which mainly consists of a triangular mesh not suitable for analysis due to overlapping and distorted elements (as highlighted in Figure 3.23).

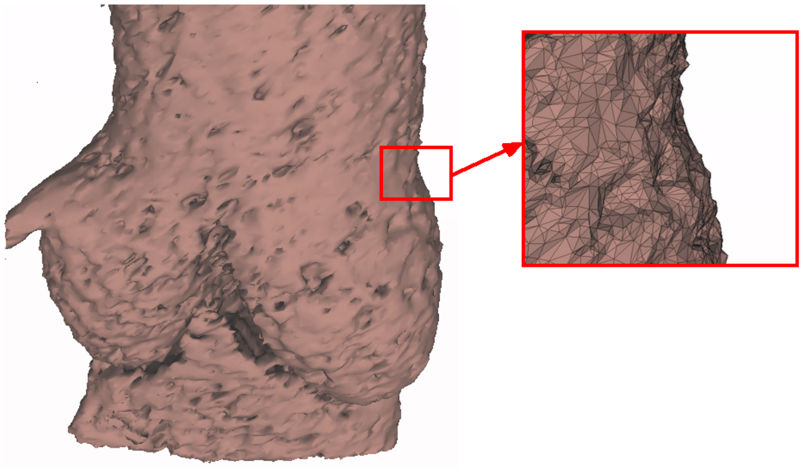

Figure 3.23 *Stereolithographic (STL) description of the aortic root extracted from medical images.*

For this reason, the STL has to be processed to extract an analysis suitable object.
In particular, we focus on two analysis suitable objects: a computational mesh for finite element simulations and a NURBS (Non-Uniform Rational B-Spline) surface for isogeometric analysis [2].
In both cases, the STL file is processed within Matlab v.R2010b (Natick, Massachusetts, U.S.A.).

The **finite element mesh** (either 2D shell or 3D solid) may be obtained following two different strategies:

- by directly selecting the nodes from the whole cloud of points of the STL file and, then, determining the connectivity to define the elements (see Figure 3.24);
- by creating a certain number of splines representing axial sections of the aortic root outer profile, then performing a lofting procedure (i.e., connecting each couple of successive splines), and finally meshing the obtained surface using standard strategies implemented within commercial finite element codes (see Figure 3.25).

On the other hand, in order to achieve a description of the aortic root through a **NURBS surface** (see Figure 3.26), we perform a mapping pro-

[2]Isogeometric analysis is an innovative technology developed and proposed by T.J.R. Hughes which seeks to unify the design procedure and the analysis process. The first paper on isogeometric analysis has been published in 2005 [75]. See Appendix A for the basic concepts of isogeometric analysis.

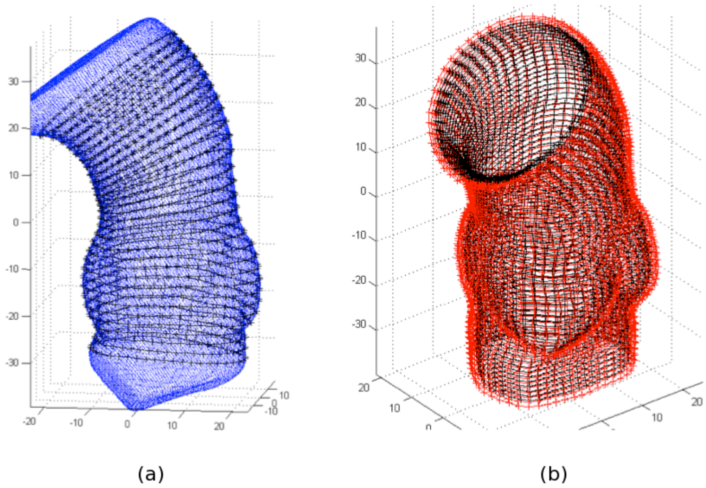

Figure 3.24 *Two steps of the procedure to generate an hexahedral mesh directly from the STL description: (a) the nodes are identified from the cloud of points of the STL file; (b) the connectivity is defined to create a set of elements.*

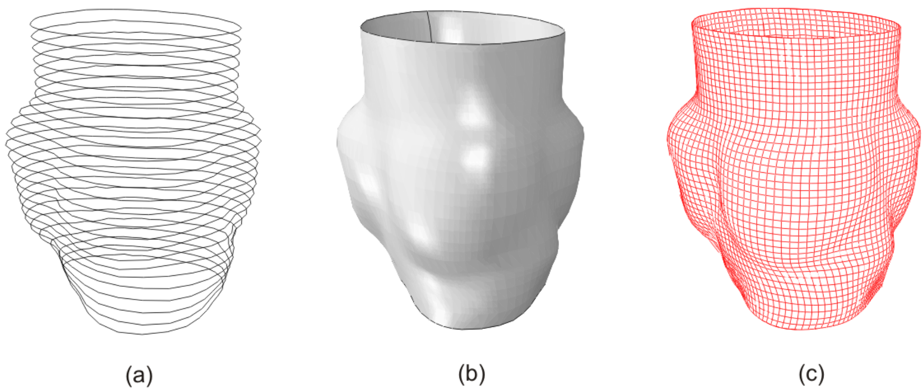

Figure 3.25 *CAD model and mesh generation of the aortic root: (a) splines are extracted by processing the STL file; (b) the CAD model is obtained by performing a lofting procedure; (c) a quadrilateral shell element mesh is defined.*

cedure, i.e., we compute in the least-squares sense the optimal position (in terms of spacial coordinates) of the surface control points so that the error between the real geometry (given by the STL file) and its NURBS representation is minimized. In Appendix A, after briefly introducing the isogeometric analysis concept, we shed some light on the discussed mapping procedure.

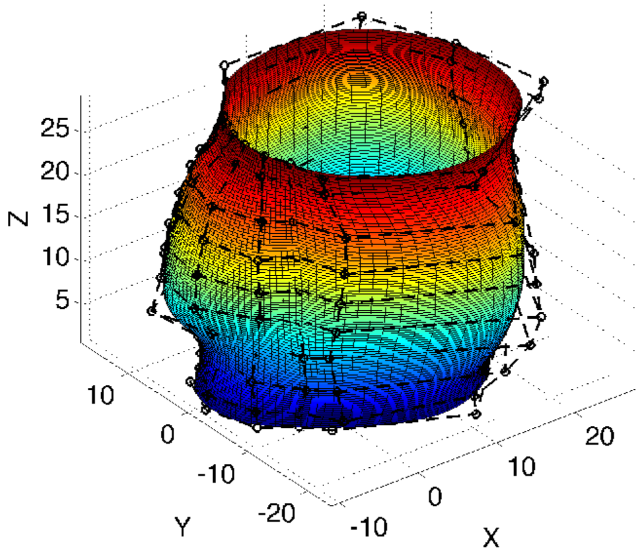

Figure 3.26 NURBS surface of a patient-specific aortic root and its associated control mesh outcome of the mapping procedure.

3.2 Aortic valve material modeling

In the last few years, there has been a significant growth in interest in the mechanical properties of biological soft tissues treated from the continuum mechanical point of view since "there are many problems in physiology whose solutions require a detailed knowledge of the mechanical properties of the tissues involved" [76].
One important motivation for such studies is the belief that mechanical factors may be important in triggering the onset of a wide set of diseases involving soft tissues. Moreover, several pathologies as well as clinical treatments can be studied in detail if reliable constitutive models of biological tissues are available.
In particular, knowing the constitutive equations of the aortic valve tissues, that is knowing the aortic valve mechanical properties, allows realistic numerical simulations able to predict the outcome of a surgical operation as well as to optimize valve prosthesis design.
In this work, two different approaches have been adopted to reproduce material behavior: initially, a simple **hyperelastic isotropic model** has been used, then, the model has been improved adopting an **anisotropic model**.
In this section, details on material testing and modeling are provided.

3.2.1 Mechanical testing

The constitutive equations of a material can only be determined by experiments.

The simplest experiment that can be done on a biological tissue is the **uniaxial tension test**. For this purpose, a specimen of rectangular shape is prepared and stretched uniaxially using a testing machine; the load and elongation are recorded for prescribed loading or stretching histories.
Uniaxial tests are generally conducted to determine tensile strength data and one dimensional elastic properties such as the elastic modulus [77].
However, a single uniaxial test is not able to evidence the complex properties of soft tissues: in fact, they generally consist of oriented networks of fibers embedded in a fluid-like matrix (the ground substance) and, for this reason, often exhibit pronounced mechanical anisotropy, non-linear stress-strain relationships, large deformations, viscoelasticity and strong mechanical coupling.
In order to overcome this limitation, it is common practice to test separately strips excised with different orientation.
Nevertheless, **biaxial tests** are more appropriate for anisotropic tissues but may be difficult to perform and control due to the small size of the specimen far from the loading attachment sites [78].
In the literature, different works dealing with experimental tests on aortic root and leaflet tissues are presented, as summarized in Table 3.1.
With respect to *aortic leaflets*, we recall the pioneristic works proposed by Missirlis et al. (1978) and Sauren et al. (1983) as well as the more recent works of Billiar and Sacks (2000a), Merryman et al. (2006), and Maynewman et al. (2009). On the other hand, with respect to the *aortic root*, the works of Sauren et al. (1980), Sauren et al. (1983), Gundiah et al. (2008) and Matthews et al. (2010) may be mentioned.
However, all these tests have been conducted on specimens of native porcine valves.
To our knowledge few experimental studies on human aortic valve are available in the literature.
In this context, we cite the works of Clark and Butterworth (1971), Missirlis et al. (1973), Christie and Barratt-Boyce (1995), Sim et al. (2003), Stradins et al. (2004), and Martin et al. (2010).
As evidenced in Table 3.1, the mechanical tests used commonly to capture the mechanical behavior of heart valve tissue are the uniaxial and biaxial tensile tests.
Among the experimental tests on human aortic valves, the only suitable for material parameter calibration are the works of Stradins et al. (2004) and Martin et al. (2010).
The results by Stradins et al. (2004) refer to uniaxial tensile tests performed on strips of human aortic leaflets excised in the circumferential and radial directions to capture the transversely isotropic behavior.
On the contrary, recent results by Martin et al. (2010) on human aortic root are obtained by stress-controlled biaxial tests.
In order to use such experimental results for fitting purposes, in the follow-

ing we briefly describe the kinematics and equilibrium equations particularly focusing on biaxial tests.

Table 3.1 *Experimental mechanical tests on porcine and human aortic valve available in the literature*

Author	Test	Specimen	Subject
Sauren et al. (1983)	uniaxial uniaxial	aortic valve sinus aortic valve leaflets	porcine porcine
Mayne et al. (1989)	equi–biaxial	aortic valve leaflets	porcine
Billiar and Sacks (2000a)	biaxial	aortic valve leaflets	porcine
Merryman et al. (2006)	biaxial	aortic valve leaflets	porcine
Stella et al. (2007)	biaxial	aortic valve leaflets	porcine
Gundiah et al. (2008)	biaxial biaxial	ascending aorta aortic valve sinus	porcine porcine
Maynewman et al. (2009)	biaxial	aortic valve leaflets	porcine
Matthews et al. (2010)	biaxial biaxial biaxial biaxial	ascending aorta aortic valve sinus pulmonary artery pulmonary valve sinus	porcine porcine porcine porcine
Author	Test	Specimen	Subject
Christie and Barratt-Boyce (1995)	equi–biaxial	aortic valve leaflets	human
Stradins et al. (2004)	uniaxial	aortic valve leaflets	human
Martin et al. (2010)	biaxial	aortic valve sinus	human

Kinematic and equilibrium in biaxial testing

Consider a thin rectangular sheet of soft biological tissue whose sides are aligned with a rectangular Cartesian coordinate system $\{\mathbf{e}_1, \mathbf{e}_2, \mathbf{e}_3\}$, as shown in Figure 3.27a.
In the reference configuration, see Figure 3.27b, the in-plane dimensions and the thickness of the specimen are denoted as L_1, L_2 and H, respectively. In the current configuration, the related dimensional quantities are denoted as l_1, l_2 and h, see Figure 3.27c.
The markers, as schematically represented in Figure 3.27b,c, define a central region of the specimen wherein the boundary effects are sufficiently dissipated so that the strain and stress fields may be considered homogeneous. Although valvular tissue is known to have heterogeneous layers, the specimen tissue is also assumed to be homogeneous through the thickness [79].

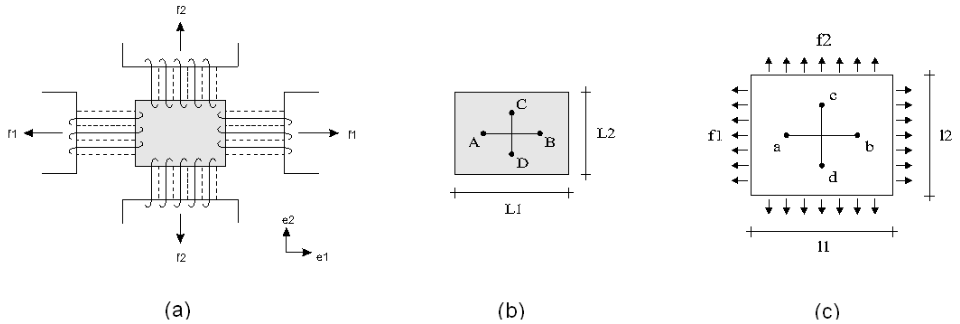

Figure 3.27 *Biaxial testing of the aortic valve tissue: (a) schematic representation of the biaxial testing apparatus; (b) specimen in the reference configuration; (c) specimen in the current configuration.*

Moreover, the material is assumed to be incompressible and the specimen is considered sufficiently thin to avoid stresses through the thickness.
Taking into consideration an homogeneous deformation (i.e., independent of position) with negligible shear strain so that the rectangular form of the sheet is preserved, which maps a material point $\mathbf{X} = (X_1, X_2, X_3)$ in the spatial counterpart $\mathbf{x} = (x_1, x_2, x_3)$ as follows:

$$x_1 = \lambda_1 X_1, \qquad x_2 = \lambda_2 X_2, \qquad x_3 = \lambda_3 X_3, \tag{3.2.1}$$

with the stretch ratios λ_1, λ_2, λ_3 independent of position, the associated deformation gradient $\mathbf{F}$ as well as the right and the left Cauchy–Green strain tensor, $\mathbf{C}$ and $\mathbf{B}$, take a diagonal form:

$$\mathbf{F} = \tfrac{\partial \mathbf{x}}{\partial \mathbf{X}} = \begin{bmatrix} \lambda_1 & 0 & 0 \\ 0 & \lambda_2 & 0 \\ 0 & 0 & \lambda_3 \end{bmatrix}, \qquad \mathbf{C} = \mathbf{F}^T\mathbf{F} = \begin{bmatrix} \lambda_1^2 & 0 & 0 \\ 0 & \lambda_2^2 & 0 \\ 0 & 0 & \lambda_3^2 \end{bmatrix}, \tag{3.2.2}$$
$$\mathbf{B} = \mathbf{F}\mathbf{F}^T = \mathbf{C}^T = \mathbf{C},$$

with principal axes coincident with the Cartesian coordinate directions $\{\mathbf{e}_1, \mathbf{e}_2, \mathbf{e}_3\}$.
The stretch ratios λ_1 and λ_2 may be experimentally calculated from the displacement of the four markers, whereas the stretch ratio λ_3 is computed from the incompressible constraint as $\lambda_3 = \lambda_1^{-1}\lambda_2^{-1}$ since thickness measurements are problematic due to the thinness of the specimen.
Let f_1 and f_2 be the in-plane loads applied to the lateral edges of the sheet and oriented as the unit vectors $\mathbf{e}_1$ and $\mathbf{e}_2$, respectively. On the contrary, no force is applied on the top and bottom faces of the sheet.
From the experimentally measured quantities, the in-plane components of the 1st Piola-Kirchhoff stress tensor $\mathbf{T}$ – which relates forces in the current configuration with areas in the reference configuration – are computed

assuming an homogeneous distribution of force across the cross-sectional thickness of the sheet:

$$T_{11} = \frac{f_1}{L_2 H}, \qquad T_{22} = \frac{f_2}{L_1 H}, \qquad T_{12} = T_{21} = 0, \tag{3.2.3}$$

whereas the non-zero components of Cauchy stress tensor are given by:

$$\sigma_{11} = T_{11} \cdot \lambda_1 = \frac{f_1}{L_2 H} \cdot \lambda_1, \qquad \sigma_{22} = T_{22} \cdot \lambda_2 = \frac{f_2}{L_1 H} \cdot \lambda_2. \tag{3.2.4}$$

3.2.2 Constitutive models

In consideration of the range of declared interest and according to experimental results, the mechanical behavior of the aortic valve tissue can be represented through a nonlinear hyperelastic model based on the existence of a strain-energy function Ψ.
For **isotropic material**, the strain-energy function Ψ depends on the change of configuration only through the deformation gradient $\mathbf{F}$. Material frame indifference satisfaction implies that Ψ is a function of $\mathbf{F}$ only through the right Cauchy–Green tensor $\mathbf{C}$.
On the other hand, for **anisotropic materials**, i.e., materials with preferred directions, the directional dependence on the deformation must be introduced explicitly in the strain–energy function Ψ, so that, if the $i-$th preferred direction in the undeformed configuration is identified by a unit vector $\mathbf{a}_{0i}$, the potential Ψ takes the form:

$$\Psi = \Psi\left(\mathbf{C}, \mathbf{a}_{0i} \otimes \mathbf{a}_{0i}\right), \qquad i = 1, 2, \ldots, N, \tag{3.2.5}$$

with N the number of preferred directions and $\mathbf{a}_{0i} \otimes \mathbf{a}_{0i}$ the so called *structural tensor*.
If the soft tissue is assumed to be incompressible, the constraint $J = \det \mathbf{F} = 1$, or equivalently $I_3 = \det \mathbf{C} = 1$, must be satisfied and included in the strain energy function Ψ as follows:

$$\Psi = -p\left(I_3 - 1\right) + \Psi\left(\mathbf{C}, \mathbf{a}_{0i} \otimes \mathbf{a}_{0i}\right), \tag{3.2.6}$$

with p a Lagrange multiplier determined from boundary conditions.
Following Spencer (1982) and Spencer (1984), the strain energy function Ψ may also be expressed in terms of the three invariants of $\mathbf{C}$, I_1, I_2, I_3:

$$I_1 = \mathrm{tr}\mathbf{C}, \qquad I_2 = \frac{1}{2}\left[I_1^2 - \mathrm{tr}\mathbf{C}^2\right], \qquad I_3 = \det \mathbf{C}, \tag{3.2.7}$$

and in terms of two additional invariants I_{4i} and I_{5i} related to the i-th preferred direction:

$$I_{4i} = \mathbf{C} : \mathbf{a}_{0i} \otimes \mathbf{a}_{0i}, \qquad I_{5i} = \mathbf{C}^2 : \mathbf{a}_{0i} \otimes \mathbf{a}_{0i}, \qquad i = 1, 2, \ldots, N. \tag{3.2.8}$$

It is worth noting that the invariant I_{4i} is the square of the stretch along the i-th preferred direction, but there is no similar simple interpretation for I_{5i}.
Moreover, coupling invariants related to each pairs (ij) of preferred directions should be introduced:

$$I_{6ij} = (\mathbf{a}_{0i} \cdot \mathbf{a}_{0j}) \left[\mathbf{C} : \mathrm{sym}\,(\mathbf{a}_{0i} \otimes \mathbf{a}_{0j})\right], \tag{3.2.9}$$

with i, j=1,2,...,N and $i \neq j$; the term $(\mathbf{a}_{0i} \cdot \mathbf{a}_{0j})$ is included to ensure that I_{6ij} is not affected by reversal of either $\mathbf{a}_{0i}$ or $\mathbf{a}_{0j}$.
Following again Spencer (1982) and Spencer (1984), the strain-energy reported in Equation 3.2.9 rewritten in terms of the invariants takes the form:

$$\Psi = -p\,(I_3 - 1) + \Psi\,(I_1, I_2, I_{4i}, I_{5i}, I_{6ij})\,, \tag{3.2.10}$$

with i, j=1,2,...,N and $i \neq j$. According to standard arguments, the 2nd Piola-Kirchhoff stress tensor $\mathbf{S}$ is calculated by taking the derivative of Ψ with respect to the right Cauchy–Green tensor $\mathbf{C}$:

$$\mathbf{S} = -\,p\frac{\partial I_3}{\partial \mathbf{C}} + 2\frac{\partial \Psi}{\partial \mathbf{C}}, \tag{3.2.11}$$

or equivalently by

$$\mathbf{S} = -\,p\frac{\partial I_3}{\partial \mathbf{C}} + \sum_a 2\Psi_a \cdot \frac{\partial I_a}{\partial \mathbf{C}}, \qquad a = 1, 2, 4_i, 5_i, 6_{ij} \tag{3.2.12}$$

with the position $\Psi_a = \partial\Psi/\partial I_a$ applied for $i, j = 1, 2, \ldots, N$ and $i \neq j$.

The invariant derivatives $\partial I_a/\partial \mathbf{C}$ are given by:

$$\frac{\partial I_1}{\partial \mathbf{C}} = \mathbf{I}, \qquad \frac{\partial I_2}{\partial \mathbf{C}} = I_1\mathbf{I} - \mathbf{C},$$

$$\frac{\partial I_3}{\partial \mathbf{C}} = I_3\mathbf{C}^{-1}, \qquad \frac{\partial I_{4i}}{\partial \mathbf{C}} = \mathbf{a}_{0i} \otimes \mathbf{a}_{0i}, \tag{3.2.13}$$

$$\frac{\partial I_{5i}}{\partial \mathbf{C}} = \mathbf{a}_{0i} \otimes \mathbf{C}\mathbf{a}_{0i} + \mathbf{C}\mathbf{a}_{0i} \otimes \mathbf{a}_{0i}, \qquad \frac{\partial I_{6ij}}{\partial \mathbf{C}} = \frac{1}{2}\,(\mathbf{a}_{0i} \cdot \mathbf{a}_{0j})\,(\mathbf{a}_{0i} \otimes \mathbf{a}_{0j} + \mathbf{a}_{0j} \otimes \mathbf{a}_{0i})\,,$$

with $i, j = 1, 2, \ldots, N$ and $i \neq j$.

Consequently, the 2nd Piola–Kirchhoff stress tensor $\mathbf{S}$ expands as follows:

$$\begin{aligned}\mathbf{S} = &-p\mathbf{C}^{-1} + 2\Psi_1\mathbf{I} + 2\Psi_2\left(I_1\mathbf{I} - \mathbf{C}\right) + \\ &+ 2\Psi_{4i}\left(\mathbf{a}_{0i} \otimes \mathbf{a}_{0i}\right) + 2\Psi_{5i}\left(\mathbf{a}_{0i} \otimes \mathbf{C}\mathbf{a}_{0i} + \mathbf{C}\mathbf{a}_{0i} \otimes \mathbf{a}_{0i}\right) + \\ &+ \Psi_{6ij}\left(\mathbf{a}_{0i} \cdot \mathbf{a}_{0j}\right)\left(\mathbf{a}_{0i} \otimes \mathbf{a}_{0j} + \mathbf{a}_{0j} \otimes \mathbf{a}_{0i}\right).\end{aligned} \tag{3.2.14}$$

The Cauchy stress tensor σ may be obtained from the 2nd Piola–Kirchhoff stress tensor $\mathbf{S}$ by using the following relation:

$$\sigma = J^{-1}\mathbf{F}\mathbf{S}\mathbf{F}^T, \tag{3.2.15}$$

with $J = 1$ for the material incompressibility.
Similarly to the 2nd Piola–Kirchhoff stress tensor, the Cauchy stress tensor expands as follows:

$$\begin{aligned}\mathbf{S} = &-p\mathbf{I} + 2\Psi_1\mathbf{B} + 2\Psi_2\left(I_1\mathbf{B} - \mathbf{B}^2\right) + 2\Psi_{4i}\left(\mathbf{a}_i \otimes \mathbf{a}_i\right) + \\ &+ 2\Psi_{5i}\left(\mathbf{a}_i \otimes \mathbf{B}\mathbf{a}_i + \mathbf{B}\mathbf{a}_i \otimes \mathbf{a}_i\right) + \Psi_{6ij}\left(\mathbf{a}_{0i} \cdot \mathbf{a}_{0j}\right)\left(\mathbf{a}_i \otimes \mathbf{a}_j + \mathbf{a}_j \otimes \mathbf{a}_i\right),\end{aligned} \tag{3.2.16}$$

with $\mathbf{a}_i = \mathbf{F}\mathbf{a}_{0i}$ and $\mathbf{a}_j = \mathbf{F}\mathbf{a}_{0j}$ the *push-forward* of $\mathbf{a}_{0i}$ and $\mathbf{a}_{0j}$ under the action of $\mathbf{F}$.
As evidenced by Equation 3.2.16, the expression of the strain-energy function Ψ defines completely the behavior of an hyperelastic anisotropic material.

3.2.3 Strain energy functions

As previously mentioned, in this work we choose to deal with two constitutive models, i.e. isotropic and anisotropic hyperelastic.
With respect to the **isotropic model**, we use a Mooney-Rivlin formulation [80, 81]:

$$\Psi_{MR} = c_{10}(\bar{I}_1 - 3) + c_{01}(\bar{I}_2 - 3) + \frac{1}{D_1}(J^{el} - 1)^2, \tag{3.2.17}$$

where Ψ_{MR} is the strain energy per unit of reference volume; c_{10}, c_{01} and D_1 are material parameters, J^{el} is the elastic volume ratio while $\bar{I}_1$ and $\bar{I}_2$ are the first and second deviatoric strain invariants defined as:

$$\bar{I}_1 = tr(\bar{\mathbf{C}}), \qquad \bar{I}_2 = \frac{1}{2}[I_1^2 - tr(\bar{\mathbf{C}}^2)], \tag{3.2.18}$$

where:

$$\bar{\mathbf{C}} = \bar{\mathbf{F}}^T\bar{\mathbf{F}} = J^{-2/3}\mathbf{C}, \qquad \bar{\mathbf{F}} = (J^{-1/3}\mathbf{I})\mathbf{F}. \tag{3.2.19}$$

With respect to the **anisotropic model**, in the context of soft biological tissues, the strain energy function Ψ is usually split into an *isotropic* part, Ψ_{iso}, associated with the elastin ground matrix, and an *anisotropic* part,

Ψ_{aniso}, associated with the embedded collagen fibers.
As shown in Table 3.2 many formulations of the strain energy function for biological tissues accounting for anisotropy are available in the literature.
In the following, we focus on the form proposed by Holzapfel et al. (2000) and Gasser et al. (2006) since those formulations are the ones used to simulate the anisotropic aortic valve behavior.
In particular, according to Holzapfel et al. (2000) the strain energy function takes the form:

$$\Psi_H = c_{10}\left(I_1 - 3\right) + \frac{k_1}{2k_2} \sum_{i=1,2} \left\{\exp\left[k_2\left(I_{4i} - 1\right)^2\right] - 1\right\}, \tag{3.2.20}$$

where $k_1 > 0$ is the stiffness module related to the two equivalent fiber sets and $k_2 > 0$ is a dimensionless constant.
It follows that the two-fiber family model is characterized by four independent parameters: c_{10}, k_1, k_2 and γ, being γ the angle defined by the two families of fibers. Sometimes the angle γ may be identified experimentally. If the tissue exhibits a transverse isotropic behavior, being characterized by only one family of fibers, which is the case of aortic valve leaflets, the angle γ is taken equal to 0.
Following Gasser et al. (2006), the anisotropic part of Ψ is modified to take into account fiber dispersion:

$$\Psi_G = c_{10}\left(I_1 - 3\right) + \frac{k_1}{2k_2} \sum_{i=1,2} \left\{\exp\left[k_2\left(\kappa I_1 + (1-3\kappa) I_{4i} - 1\right)^2\right] - 1\right\}, \tag{3.2.21}$$

where the dispersion parameter $\kappa \in \left[0, \frac{1}{3}\right]$ can either be determined experimentally or taken as an unknown parameter. The boundary case $\kappa = 0$ corresponds to no dispersion, (i.e., fibers perfectly aligned), whereas $\kappa = \frac{1}{3}$ to an isotropic distribution in the fiber orientation (i.e., fibers randomly distributed).

3.2.4 Optimization method

Parameter estimation based on the nonlinear least squares method has been widely used to characterize constitutive material parameters from experimental data [82, 83].
With respect to biaxial test, the indirectly measured kinematic quantities are the stretches λ_1, λ_2 (with $\lambda^3 = \lambda_1^{-1}\lambda_2^{-1}$ for the incompressible condition), whereas the indirectly measured static quantities are the stresses σ_{11}^{exp}, σ_{22}^{exp} (with $\sigma_{33}^{\text{exp}} = 0$ for the plane stress condition). The superscript "exp" stands for experiment. Usually, the measured quantities are considered free of errors.

Table 3.2 *Strain energy function for anisotropic materials available in the literature*

Author	Strain energy function for two-fiber reinforced materials	Application
Holzapfel et al. (2000)	$\Psi = c_{10}\left(I_1 - 3\right) + \frac{k_1}{2k_2} \sum_{i=1,2} \left\{\exp\left[k_2\left(I_{4i} - 1\right)^2\right] - 1\right\}$	A[1]
Gasser et al. (2006)	$\Psi = c_{10}\left(I_1 - 3\right) + \frac{k_1}{2k_2} \sum_{i=1,2} \left\{\exp\left[k_2\left(\kappa I_1 + (1 - 3\kappa) I_{4i} - 1\right)^2\right] - 1\right\}$	A[1]
Author	**Strain energy function for transversely isotropic materials**	**Application**
Humphrey et al. (1987)	$\Psi = A\left\{\exp\left[c_1\left(I_1 - 3\right)\right] - 1\right\} + B\left\{\exp\left[c_2\left(\sqrt{I_4} - 1\right)^2\right] - 1\right\}$	M[2]
Maynewmann and Yin (1998) Maynewmann et al. (2009)	$\Psi = c_0\left\{\exp\left[c_1\left(I_1 - 3\right)^2 + c_2\left(\sqrt{I_4} - 1\right)^4\right] - 1\right\}$	ML[3] AL[4]
Prot et al. (2007)	$\Psi = c_0\left\{\exp\left[c_1\left(I_1 - 3\right)^2 + c_2\left(I_4 - 1\right)^2\right] - 1\right\}$	ML
Weinberg and Kaazempur-Mofrad (2006)	$\Psi = c_{10}\left(I_1 - 3\right) + c_0\left\{\exp\left[c_1\left(I_1 - 3\right)^2 + c_2\left(\sqrt{I_4} - 1\right)^4\right] - 1\right\}$	ML
Prot et al. (2010)	$\Psi = c_{10}\left(I_1 - 3\right) + c_0\left\{\exp\left[c_1\left(I_1 - 3\right)^2 + c_2\left(I_4 - 1\right)^2\right] - 1\right\}$	ML

[1] Arteries
[2] Myocardium
[3] Mitral Leaflets
[4] Aortic Leaflets

The related theoretical stresses σ_{11}^{Ψ}, σ_{22}^{Ψ} are computed by derivation of the strain-energy function with respect to the strain measures, see Equation (3.2.11). The superscript Ψ script stands for theoretical value.
According to Equation (3.2.16), σ_{11}^{Ψ} and σ_{22}^{Ψ} may be expressed as functions of the unknown material parameters, denoted with κ, and as functions of stretches λ_1, λ_2:

$$\sigma_{11}^{\Psi} = \sigma_{11}^{\Psi}\left(\kappa, \lambda_1, \lambda_2\right), \qquad \sigma_{22}^{\Psi} = \sigma_{22}^{\Psi}\left(\kappa, \lambda_1, \lambda_2\right). \tag{3.2.22}$$

The standard minimization technique requires the definition of the objective function χ^2 as the squared sum of the residuals, i.e., the difference between the experimental stress data and the corresponding theoretical values:

$$\chi^2\left(\kappa\right) = \sum_{a=1}^{p}\left[w_1^2\left(\sigma_{11}{}_a^{\Psi} - \sigma_{11}{}_a^{\exp}\right)^2 + w_2^2\left(\sigma_{22,}{}_a^{\Psi} - \sigma_{22,}{}_a^{\exp}\right)^2\right], \tag{3.2.23}$$

with p the number of data points and with κ the set of unknown constitutive parameters.
The weighting factors w_1 and w_2 are introduced to assign different weights and to scale properly the two terms in Equation (3.2.23).
The minimization problem becomes:

$$\begin{cases} \min\limits_{\kappa} \chi^2\left(\kappa\right), \\ \text{subjected to:} \quad \kappa \in \mathcal{K}, \end{cases} \tag{3.2.24}$$

with $\mathcal{K} = \{\kappa : \kappa^- \leq \kappa \leq \kappa^+\}$ the solution space and κ^- and κ^+ the lower and upper bounds for the material parameters, respectively.
Commercial codes may be used to accomplish the minimization. In this study, we developed a simple code to implement the objective function (3.2.23), whereas the minimization problem (3.2.24) has been solved using a standard function within Matlab (The Mathworks, Natick, MA, USA).
The normalized mean square root error (NRMSE) as proposed by Holzapfel et al. (2005) is used to evaluate the quality of the fittings:

$$NRMSE = \sqrt{\frac{\chi^2}{p-q}} \cdot \frac{1}{\sigma_{\text{ref}}}, \tag{3.2.25}$$

with q the number of parameters and p the number of data points.
The value σ_{ref} is the sum of all Cauchy stresses for each data point divided by the number of all data points:

$$\sigma_{\text{ref}} = \frac{1}{p} \cdot \sum_{a=1}^{p}\left(\sigma_{11}{}_a^{\exp} + \sigma_{22}{}_a^{\exp}\right). \tag{3.2.26}$$

In addition, in order to provide a good representation of experimental data, the set κ of constitutive parameters must also satisfy some convexity conditions for the strain–energy function Ψ in order to exclude ambiguous numerical solutions of nonlinear problems [84, 85, 86, 87].
The mentioned convexity conditions reflect in a set of constraints for the material parameters κ which restricts the solution space $\mathcal{K}$ making the problem (3.2.24) a constrained minimization problem:

$$\begin{cases} \min\limits_{\kappa} \chi^2(\kappa), & \\ \text{subjected to:} & c(\kappa) \leq 0 \\ & ceq(\kappa) = 0 \\ & \kappa \in \mathcal{K} \end{cases} \tag{3.2.27}$$

with $c(\kappa)$ and $ceq(\kappa)$ vector functions.
Unfortunately, this occurrence could be inconsistent with the ability of the model to fit the experimental data.
Even though the set κ of constitutive material parameters ensures the convexity of Ψ, the objective function χ^2 may be non-convex on the solution space. Consequently, the problem presented in (3.2.24) or (3.2.27) defines a nonlinear and non convex problem of optimization.
From the parameter identification point of view, this is an undesirable property, since for a non-convex optimization problem there may exist several local minima in the solution space and gradient based minimization algorithms cannot guarantee the convergence to the global minimum [88, 89].
A direct implication of this occurrence is the strong dependence of the solution on the initial guess.
Two approaches could be used to overcome these difficulties: (i) to use a global search algorithm, i.e., a method able to identify the unique minimum in the solution space; (ii) to convexify the non-convex optimization problem. However, these two approaches exceed our purposes.
For this reason, the quality of the obtained solution has been tested by perturbing the initial guess. If the convergence is very closed to the same optimum, the found set of material parameters may be considered an acceptable solution [90].
The results of the fitting procedure based on experimental data of both aortic leaflets and sinuses are reported in Figure 3.28 and 3.29, respectively. The obtained material parameters are listed in Table 3.3 and in Table 3.4.

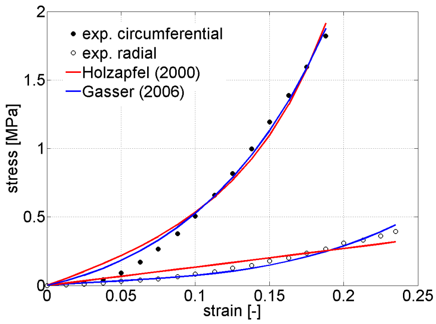

Figure 3.28 *Circumferential and radial stress-stretch response of human aortic leaflets compared with the models proposed by Holzapfel (2000) and Gasser (2006).*

Table 3.3 *Material parameters for human leaflets.*

Ψ	Material parameters				q	NRMSE
	c_{10}(MPa)	$k_1(MPa)$	k_2	κ		
Holzapfel (2000)	0.222	0.641	4.78	–	3	0.1751
Gasser (2006)	0.041	14.71	3.83	0.05	4	0.0898

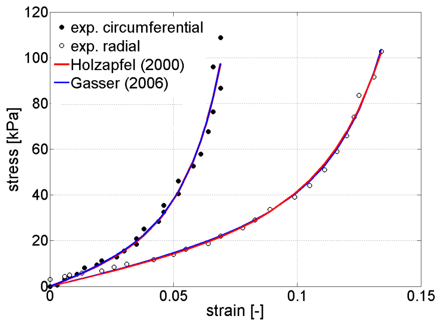

Figure 3.29 *Circumferential and radial stress-stretch response of human aortic sinuses compared with the models proposed by Holzapfel (2000) and Gasser (2006).*

Table 3.4 *Material parameters for human sinuses.*

Ψ	Material parameters					NRMSE
	c_{10}(kPa)	k_1(kPa)	k_2	κ	β(deg)	
Holzapfel (2000)	29.45	148.5	484.2	–	40.90	0.115
Gasser (2006)	38.01	852.5	2245	0.22	38.5	0.105

3.3 Loading conditions to simulate aortic valve behavior

Fluid-structure interaction (FSI) between the solid aortic root and blood would be the more appropriate condition to be considered when simulating aortic valve behavior. FSI analysis of the aortic valve is very complex due to large displacements of the leaflets, contact, and presence of the so-called *added mass effect* (the density of biological tissues are very close to blood density, inducing numerical instabilities); besides these aspects, modeling the interaction between blood and valve structures is not the intent of this work.
However, to correctly reproduce aortic valve behavior, simplified structural boundary conditions may be adopted if properly defined.
The aortic valve deformation is controlled by pressure acting on the aortic system. As in previous studies [35, 36, 91], the leaflets are assumed to be stress-free in the open position.
Three different areas should be defined to properly apply the loads on valve structures: the aortic root wall below the line of leaflet attachment, the aortic root wall above the the line of leaflet attachment and the leaflets (see Figure 3.30a). Blood pressure acting on root structures is modeled using time-dependent pressure loads corresponding to physiologically measured waveforms (see Figure 3.30b). In particular, the load to be sustained by the aortic valve results from the difference between the aortic and left ventricular pressure (i.e., the pressure gradient across the valve).

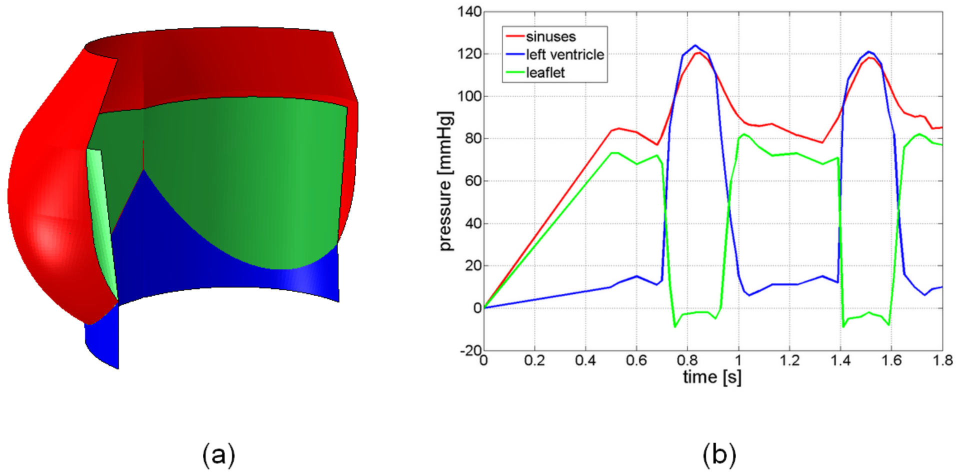

Figure 3.30 *Pressure on aortic valve structures: (a) three different regions are defined; (b) the pressure curves corresponding to each predefined aortic region adapted from [92].*

Chapter 4

FEA of aortic valve surgical operations

Moving from the motivation presented in the Introduction of this work, i.e., aiming at providing heart surgeons with useful information for the decision-making process and operation planning procedure, we have adopted the finite element methodology to simulate three different surgical strategies commonly performed to restore aortic valve functionality. The goal is to predict, by means of virtual computer-based analyses, the potential optimal surgical choice and prosthetic device for a specific patient.
In particular, we have performed realistic simulations (creating appropriate models and defining physiological loads and boundary conditions) which mimic:

1. the implant of prosthetic Dacron grafts for aortic valve sparing operations;

2. the implant of stentless biological valves for aortic valve replacement in case of valve stenosis;

3. the implant of transcatheter aortic valves for the treatment of aortic stenosis when open-chest surgery is not recommended.

4.1 Aortic Valve Sparing Operation

Aortic Valve Sparing (AVS) procedures have been introduced to treat ascending aorta dilatation and aortic valve insufficiency in presence of preserved native aortic valve leaflets. Even though surgical technique has been standardized, the choice of the best type and size of Dacron graft to be used is still a matter of debate. Here we present our results based on a patient-specific finite element model devoted to optimize the choice of the Dacron prosthesis size and shape.
The framework of our finite element study includes four steps: 1) creation of a geometric model of the patient's aortic root; 2) creation of a model for two different Dacron grafts (the standard straight graft and the Valsalva

graft) considering, for each type, sizes ranging from 24 to 30; 3) virtual computer-based simulation of the AVS procedure using each graft; 4) virtual computer-based simulation of the diastolic closure of the repaired valve and evaluation of post-implant physiology based on the measure of three different parameters: the height of coaptation ratio (H_c^R), the length of coaptation ratio (L_c^R) and the distance between the central point of coaptation and the ideal geometrical centre (D_c).
The simulation results of the post-implant performance of the aortic valve reveal that both H_c^R and L_c^R decrease when increasing the graft size while no significant differences are shown between the two types of graft. On the contrary, the Valsalva graft, compared with the standard straight one, leads to a significant reduced Dc. The results in terms of H_c^R, L_c^R and D_c univocally recommend, for the specific case under investigation, size 30 straight graft and size 28 Valsalva graft as the solutions assuring the most physiological valve behaviour for the specific patient under investigation.
In this work, we evaluate the potential of pre-operative prediction of the optimal graft size using FEA: the virtual simulation of the AVS procedure is actually feasible and can be useful in predicting the post-operative physiology of the aortic root. In particular, our finite element model could have a clinical impact since it is able to optimize the surgeon's choice of prosthesis size.

4.1.1 Background

Cardiovascular diseases (CVD) are the major cause of death in Western countries [3, 93] and, currently, research activities are focused on prevention, diagnosis and treatments, exploiting the interaction between different scientific fields, ranging from medicine to engineering.
From a macro-functional point of view, heart and large blood arteries can be oversimplified into two serial elements, the pulmonary circulatory system and the systemic circulatory system, driven respectively by the right ventricle and the left ventricle acting as pumps. Hidden behind such an apparent simplicity, the micro-functionality of each component is extremely sophisticated.
In particular, as highlighted in Chapter 2, the aortic root is a complex body district from both anatomical and functional point of view, where biological structure and physiology are strictly related. The complexity of the aortic root becomes clear in case of valve diseases, when even small functional deviations may decompensate the whole regulatory circuits. In particular, congenital or acquired diseases can lead to aortic root and annulus dilation [39, 94] and, consequently, to aortic valve insufficiency providing a retrograde blood flow from aorta to ventricle due to a central gap between the leaflets during diastole.
It is experimentally proved that dilated aortic roots are characterized by the

following issues: (i) a remarkable increase of the diameter of the sinotubular junction (D_{STJ}) while the annulus diameter does not show obvious change, (ii) a lengthening of the sinuses of Valsalva which become taller and (iii) a stretching of the leaflets which appear to be larger [44].
In case of aortic root dilation, aortic valve sparing (AVS) techniques may be adopted with the aim of restoring the valve competence by a reconstruction of the aortic system maintaining the native leaflets.
As highlighted in Figure 4.1, the procedure can be resumed in three main steps:

1. excision of the dilated aortic root;
2. anchoring of the prosthetic graft;
3. integration of the native valve in a Dacron tubular prosthesis.

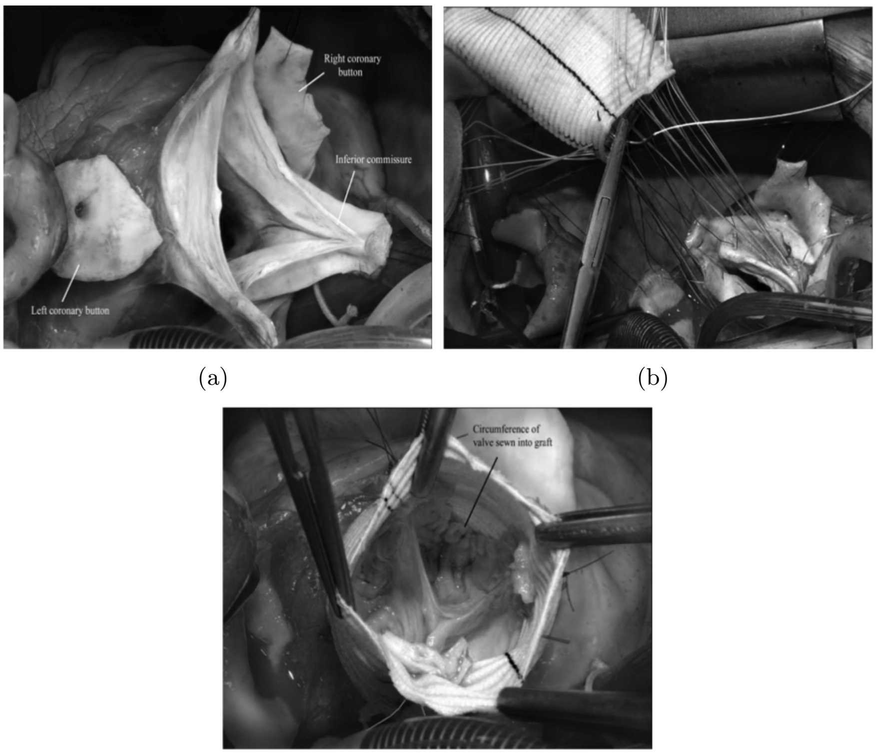

(a) (b)

(c)

Figure 4.1 *Aortic valve sparing procedure: (a) excision of aortic root in order to achieve an ad hoc structure containing the native valve; (b) anchoring of the prosthesis tube, replacing ascending aorta, and excised aortic valve; (c) whole re-implanted aortic valve, within prosthesis tube, presenting* mercedes star *like shape.*

Benefits related to the use of native valves (e.g. anticoagulant avoidance and physiological aspects) have their counterparts in the high level of technical

skills required to perform the procedure. In fact, matching both the shape and the size of valve leaflets and tube prosthesis are critical aspects and they have an impact on the efficiency and durability of the treatment [39, 95, 96]. The original AVS technique presented by David [97] , known as the "reimplantation" technique, included the excision of the aortic root and its replacement by means of a cylindrical straight polyester graft. Several modifications of the original technique [98, 99, 100], as well as different graft types [101], have been proposed to optimize the post-operative physiological function of the reconstructed aortic root.
However, the choice of the best graft type and size to be adopted for specific patients is still a matter of debate and several formulae and methods have been presented to guide the intra-operative surgeon's decision [102, 103, 104, 105]. In this work, we aim at predicting the optimal surgical solution in terms of graft type and size performing virtual patient-specific simulations based on finite element analysis.

4.1.2 Materials and Methods

The FEA model includes four steps which can be summarized as follows:

1. creation of the pathological aortic root model (based on ultrasound measures in 1 patient);
2. creation of the prosthetic graft model (2 Dacron graft types, 4 sizes for each type);
3. computer-based simulation of the AVS surgical procedure (8 different configurations);
4. computer-based simulation of the diastolic valve behaviour for each post-operative configuration.

All the simulations are performed using Abaqus software (v.6.10, Dassault Systèmes, Providence, RI, USA) as finite element solver.

1. The geometrical model of the dilated aortic root is based on direct echocardiographic measurements (diameter of the annulus; diameter of the sinotubular junction; sinus height; leaflet free margin length; leaflet height).
   In particular, we firstly create a healthy aortic root (leaflets+sinuses) based on the Labrosse model [26] (see Figure 4.2a) and then, as depicted in Figure 4.2b, we simulate the process of dilation applying radial displacements to the nodes of the commissures as described in Auricchio et al. [34] so that the resulting dimensions agree with the pathological ones evaluated by means of echocardiography.

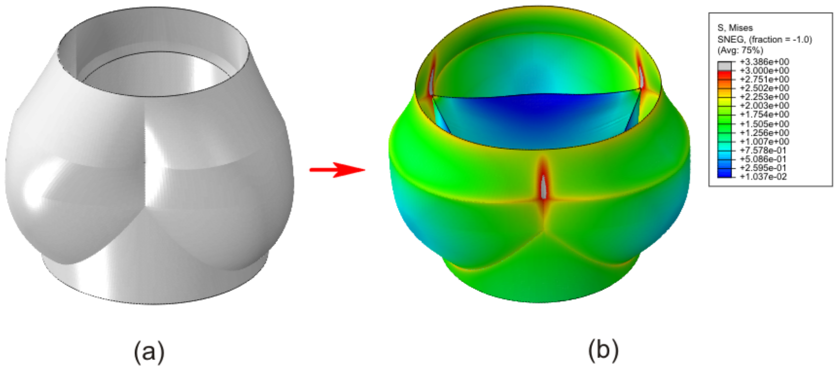

Figure 4.2 *Creation of the pathological dilated aortic valve: (a) an healthy parent model of the aortic root is created based on the Labrosse model; (b) the process of dilation is simulated by FEA. Radial displacements are applied to the nodes of the commissures in order to reproduce the pathologic dilation: the von Mises stress pattern is highlighted.*

The geometrical model of the stretched valve is finally obtained by setting to zero the developed internal stresses (Figure 4.3a) and by removing the Valsalva sinuses (Figure 4.3b).

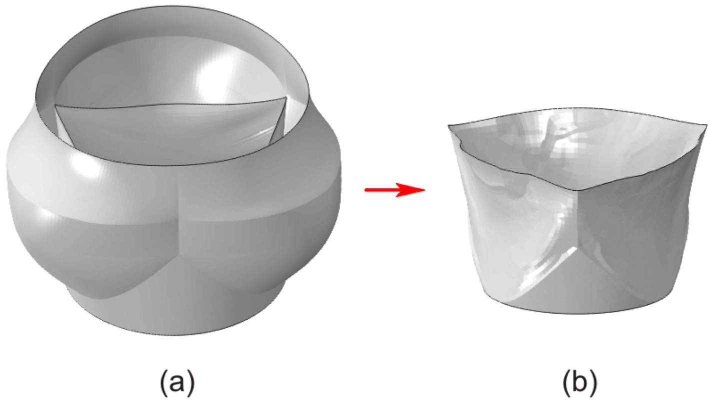

Figure 4.3 *Procedure to get the pathological geometry of the stretched leaflets: (a) the pathologic model of the dilated aortic root obtained through a finite element simulation is characterized by the same dimensions measured with echocardiography; (b) the native aortic valve, stretched due to the dilatation of the aortic root, is extracted from the whole pathologic model.*

Thickness values (1.5 mm for the sinuses and 0.5 mm for the leaflets) and material parameters are based on previously published data [92]: a Mooney-Rivlin isotropic hyperelastic model (density=1000 kg/m^3,

C_{10}=0.5516 MPa, C_{01}=0.1379 MPa) is adopted to represent the material behaviour. Both 4-node membrane elements, M3D4R, and 3-node membrane elements, M3D3, are used to mesh the leaflets while the Valsalva sinuses are meshed with shell elements, S4R.

2. The creation of a finite element model of a possible prosthesis to be used during the surgical procedure is based on company specifications (see Figure 4.4) [106].
   In particular, the prosthesis model is obtained from two different graft types: the standard graft and the Valsalva graft (Vaskutek Terumo, Renfrewshire, UK); the latter is characterized by a peculiar shape which mimics the presence of the Valsalva sinuses [101]. Sizes ranging from 24 to 30 are reproduced for both graft types; the prostheses are modelled as rigid bodies meshed with 4-node surface elements, SFM3D4R.

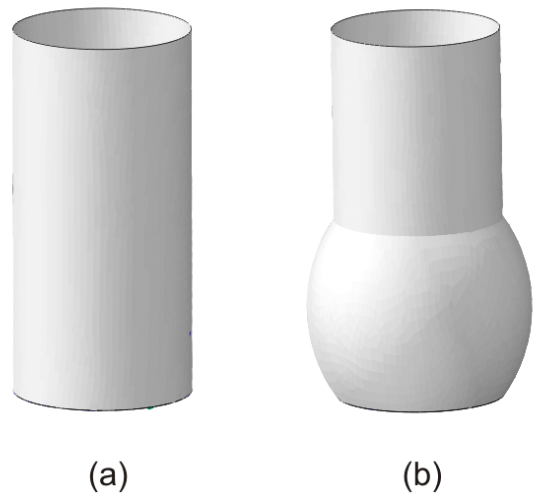

Figure 4.4 *Dacron graft adopted in clinical practice to restore valve functionality in case of dilated root: (a) the Standard Dacron Graft; (b) the Valsalva graft [101].*

3. The native aortic valve model is then combined with the prosthesis model. In particular, the diameter of the prosthetic device, which is, in the initial configuration, intentionally greater than the real one, is gradually reduced without modifying the prosthesis geometry; displacements are applied to the graft nodes to virtually reproduce the effective surgical procedure. The interaction between the graft and the prosthesis was modeled adopting a frictionless algorithm. The constraining effect of the applied graft makes these nodes radially moving through the phases of simulation.

4. Finally, we evaluate the performance of the graft implant by simulating the post-operative valve closure during diastole in terms of the parameters highlighted in Figure 4.5. To model the diastolic loading of the aortic root, an 80 mmHg physiological uniform pressure is applied on the leaflets. The nodes belonging both to the annulus and to the commissures are blocked.

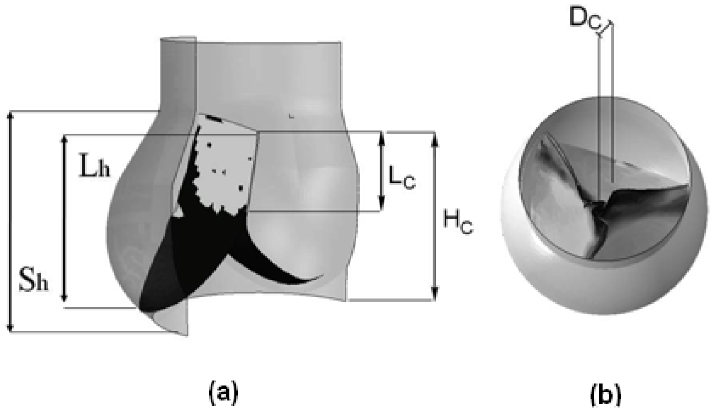

Figure 4.5 *Parameters used for the evaluation of the post-operative valve performance: (a) H_c = Height of coaptation; L_c = Length of coaptation; S_h = Sinus height; L_h = Leaflets height; (b) a third parameter is used to evaluate the post-operative valve performance; D_c= Displacement of coaptation, i.e., distance of the center of leaflet coaptation from the geometrical center of the Dacron tube.*

The numerical analyses of both graft placement and valve closure are non-linear problems involving large deformation and contact. For this reason, quasi-static procedures are used assuming that inertia forces do not dominate the analysis. Kinetic energy is monitored to ensure that the ratio of kinetic energy to internal energy remains less than 10%. Finally, a mass scaling strategy is adopted to reduce computational cost. A frictionless general contact algorithm has been used in order to handle the interactions between the leaflets.
The optimal size and graft type to be implanted are evaluated on the basis of the prediction of three measurable post-operative parameters: (i) height of coaptation ratio ($H_c^R = H_c/S_h * 100$) defined as the level of the sinus height where the coaptation occurs (H_c, highlighted in Figure 4.5a) correlated to the total sinus height, S_h; (ii) length of coaptation ratio ($L_c^R = L_c/L_h * 100$) defined as the effective coaptation length (L_c, highlighted again in Figure 4.5a) correlated to the leaflet height, L_h; (iii) displacement of coaptation (D_c) which should represent a marker of the asymmetric coaptation since it is defined as the distance of the central point of coaptation from the ideal

geometrical centre (see Figure 4.5b).
According to our pre-study trans-thoracic echo evaluation on patients without aortic valve disease we identify the target most physiological postoperative conditions for: a) H_c^R approaching 100%; b) L_c^R approaching 40%; c) minimal D_c.

4.1.3 Results and Discussion

From the obtained results relative to a dilated aortic root of one specific patient, our finite element predictive model shows how the use of a different type and size of graft is able to significantly influence post-operative parameters. Both H_c^R and L_c^R gradually decrease when increasing the graft size (see Figure 4.6(a) and 4.6(b)) and the trend is similar regardless the considered graft type. The value of D_c (see Figure 4.6(c)), and therefore the grade of asymmetric coaptation, is conversely reduced when increasing the graft size.
Furthermore, the Valsalva graft seems to warrant a significant reduced D_c (see Figure 4.7) compared to the standard straight graft (see Figure 4.8) for any size of comparison.
According to the criteria previously described, Valsalva graft size 28 is identified as the optimal solution. Interestingly, it was used by the surgeon, blinded regarding the results of the numerical simulations; even we engineers were actually blinded regarding the surgeon's choice. The comparison between in-vivo post-operative echocardiographic measurements (both H_c^R and L_c^R) reveals a good match with FEA prediction.

Here we report our preliminary experience in the development of a patient-specific application of FEA to optimize the choice of graft size and type during AVS procedure, thus enhancing post-operative results. Introduced by David in 1992 [97] the so-called "valve sparing" procedures were designed to treat aortic valve insufficiency, due to aortic root dilatation, preserving the native valve leaflets. The original technique presented by David included the excision of the aortic root and the suture of the native aortic valve inside a cylindrical straight polyester graft. This technique has been therefore popularized as the *reimplantation* technique in comparison to the *remodeling* technique, introduced by Sarsam and Yacoub [107], which did not include the reimplantation of the valve inside a graft and, consequently, should be reserved to patients without annular dilatation.
The lack of the Valsalva sinuses has been considered as the principal cause of suboptimal post-operative results following reimplantation procedure and, therefore, further evolutions of such a technique have been focused to recreate the physiological function of the Valsalva sinuses.
Cochran et al. [98] and David et al. [99] presented a modified version of original techniques, aiming at restoring the sinuses shape using additional

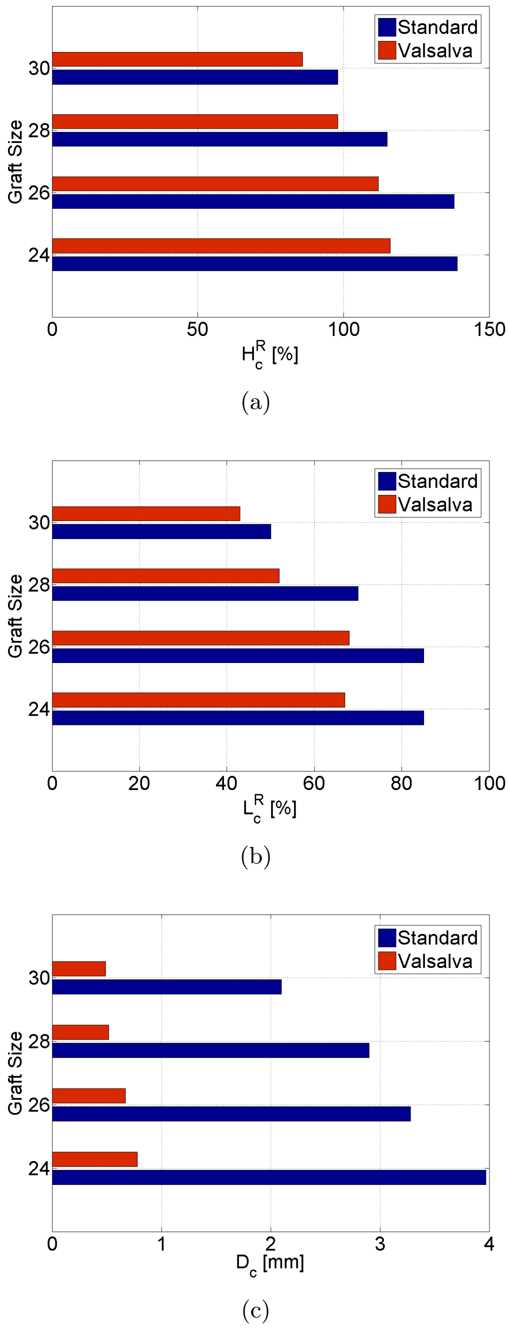

Figure 4.6 *Post-operative predictions: (a) trend of H_c^R (height of coaptation ratio) according to different type and size of graft; (b) trend of L_c^R (length of coaptation ratio) according to different type and size of graft; (c) trend of D_c (displacement of coaptation) according to different type and size of graft.*

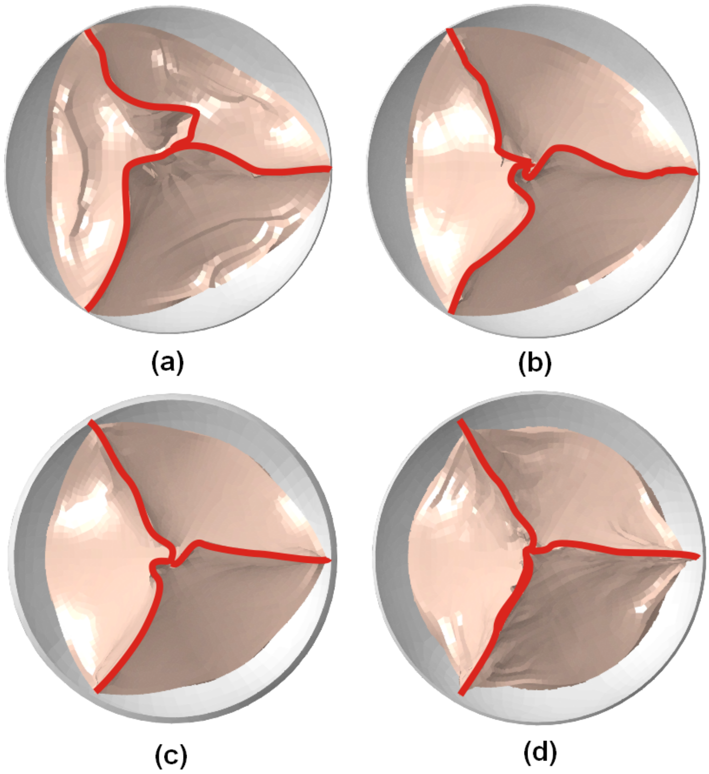

Figure 4.7 *Top-view of the simulation results of the AVS procedure using the Valsalva graft. The leaflet free-margins of the closed valve in the post-operative configuration are highlighted: (a) size 24; (b) size 26; (c) size 28; (d) size 30.*

sutures. Finally, in 2000 De Paulis et al. [101] introduced a technique based on a dedicated graft, which they called Valsalva graft, characterized by a self-expandable region obtained by a 90° rotation of the Dacron corrugations, which recreated the Valsalva sinuses.
Based on satisfactory short and long-term results reported in the literature [108], AVS has been recognized as an effective and extremely useful procedure even in sub-optimal series of patients such as Marfan patients [109].
Some technical aspects related to AVS are, however, still debated such as the choice of the shape and the size of the Dacron graft, choice that David defined “more art than science” [6].
Several studies have been published reporting some pitfalls in selecting the best size of the graft. Svensson et al. [103] proposed a sizing of the graft based on the oversizing of the ideal left ventricle outflow tract size. Maselli et al. [104] introduced a normogram based on a mathematical model taking into account the leaflet size which should be helpful in calculating the grade of graft oversizing with respect to the aortic annulus dimension [110].

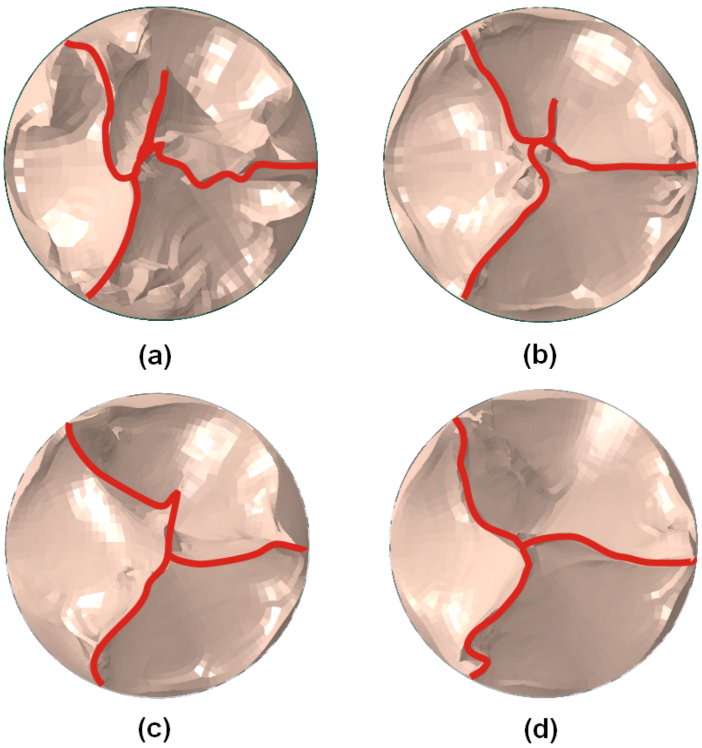

Figure 4.8 Top-view of the simulation results of the AVS procedure using the standard straight tube graft. The leaflet free-margins of the closed valve in the post-operative configuration are highlighted: (a) size 24; (b) size 26; (c) size 28; (d) size 30.

However, all of the above methods, as well as those by Morishita et al. [102] and Kollar et al. [105], were based on intra-operative measurements and allowed only an intra-operative selection of the graft. Therefore, we decided to evaluate the potential of pre-operative prediction of the optimal graft size using FEA.
FEA has been previously applied in cardiovascular medicine since late 90's in order to better understand the aortic valve physio-pathology [35]. Then, it has been focused on the evaluation of the mechanism of aortic insufficiency in complex aortic root pathology [30, 31] and, finally, the application of mathematical models has been tested to evaluate the results of surgical procedures in the treatment of aortic root diseases.
Grande et al. [95] had previously showed, with a FEA study, that the re-creation of sinuses is important following valve sparing procedures. Their study was focused mainly on the stress/strain distribution in the leaflets and in the aortic wall and showed that the re-creation of sinuses bring leaflet stresses closer to normal but did not give any further specification. Their

results are consistent with our findings demonstrating that post-operative physiology is better preserved when using a Valsalva graft.
On the other hand, Soncini et al. [91] compared root physiology following remodeling or reimplantation technique using a model based on both closing and opening phases of the valve and focused also on post-operative leaflet coaptation. Despite showing that a scalloped graft used in the remodeling technique could better preserve the physiological kinematics of leaflets and also the extension of the coaptation area, their model was not designed as a patient-specific model. Furthermore, they did not consider the Valsalva graft in the reimplantation technique. Interestingly they introduced the concept of the dislocation of nodule of Arantius as a marker of non-physiological closure of the valve.
However, to our knowledge, FEA has never been used to obtain a prediction of post-operative patient-specific results. Therefore, the innovative aspect of our study consists in the extension of the application of finite element models from the descriptive and diagnostic area to the extremely more complex and potentially valuable area of prediction of surgical results in a patient-specific relationship.
We do believe that our findings represent an ideal evolution of previous studies as they confirm that a surgical technique which reconstructs Valsalva sinuses, as in our study is the use of Valsalva graft, is preferable since it leads to a more physiological and symmetrical valve closure.
Our study also shows that we can move toward an easy pre-operative patient-specific identification of the best graft size which is not always easy to identify intra-operatively as it can be influenced by many factors related to the native aortic root and valve [111]. Moreover our study is consistent with previous considerations by Maselli et al. [104] regarding the need of optimal graft choice to avoid, on one hand, reduced leaflet coaptation (in case of excessive oversizing) or, on the other hand, the contact between the leaflet and the sinus wall during valve opening (in case of limited oversizing).
In conclusion, our study clearly confirms that application of FEA should move forward to the evaluation of the results of medical procedures. Patient-specific prediction of surgical procedure, as recently showed by cardiology interventional procedures [112, 113, 114], could represent a key factor in the future surgical decision making process in order to optimize post-operative results, and further study in this respect should therefore be encouraged.

Open problems

Our study surely carries some limitation common to other FEA-based studies. First of all, our finite element model does not include specification on tissue anisotropic elastic properties and, especially, any fluid-structure interaction is considered and, consequently, it does not carry any information

about the retrograde blood flow in case of aortic valve insufficiency.
Finally, in the evaluation of post-operative physiology of the aortic root we use some parameters, which were not validated by previous study and this in the attempt to translate in a numeric variable the grade of asymmetry of leaflet coaptation. Of course, future developments are welcome in order to further validate the parameters we introduce in this study.

4.2 Implant of the Freedom SOLO stentless valve

In some cases of aortic valve leaflet disease, the implant of a stentless biological prosthesis represents an excellent option for aortic valve replacement (AVR). In particular, if compared to more classical surgical approaches, it provides a more physiological hemodynamic performance and a minor trombogeneticity avoiding the use of anticoagulants. The clinical outcomes of AVR are strongly dependent on an appropriate choice of both prosthesis size and replacement technique, which are, at present, strictly related to surgeon's experience and skill. Therefore, also this treatment, like most reconstructive procedures in cardiac surgery, remains "more art than science" [6]. Nowadays computational methodologies represent a useful tool both to investigate the aortic valve behavior, in physiologic and pathologic conditions and to reproduce virtual post-operative scenarios. The present study aims at supporting the AVR procedure planning through a patient-specific Finite Element Analysis (FEA) of stentless valve implantation. Firstly, we perform FEA to simulate the prosthesis placement inside the patient-specific aortic root; then, we reproduce, again by means of FEA, the diastolic closure of the valve to evaluate both the coaptation and the stress/strain state. The simulation results prove that both the valve size and the anatomical asymmetry of the Valsalva sinuses affect the prosthesis placement procedure.

4.2.1 Background

Valvular heart pathologies represent a remarkable contribution to CVD, which, as already mentioned, are the major cause of death in the Western countries [3].
With respect to aortic valve, there are two main conditions which impair the native valve functionality: insufficiency and stenosis. In the first case, the valve is not able to close completely during diastole, causing blood regurgitation from the aorta to the left ventricle. In the second case, large calcium deposits on the valve contribute to the narrowing of its opening, thus reducing blood flow ejection.
Different surgical treatments are adopted to restore valve functionality. In the literature many techniques for aortic root recontruction are described, either sparing the valve leaflets [107, 115] or involving the use of mechanical [116], stented [117, 118] or stentless biological prostheses [119] as well as homograft and allograft valves [120, 121].
If the aortic root wall does not show any remarkable pathological dilation so that the valvular leaflets can be considered as the principal cause of disease, the aortic valve is replaced by means of mechanical or biological valves: many comparative studies are reported in the literature [122, 123, 124].
On the one hand, mechanical prostheses assure a long-term solution due to an excellent durability [125], on the other hand, they are associated with a

greater incidence of hemorrhage than bioprostheses which avoid the use of anticoagulants and determine a more physiological hemodynamics as well as a minor trombogeneticity [126]; accordingly, expecially for elderly patients, biological valves assure greater performances than mechanical ones and, in particular, stentless valves are preferable than stented ones, representing an "excellent option for aortic valve replacement" [127].
The use of stentless valves, in fact, appears to potentially increase the long-term survival when compared to stented ones due to improved ventricular reverse remodeling [128]. At the same time, the hemodynamics is closer to physiologic behavior; finally, the use of a continuos suture technique reduces the crossclamp times and cardiopulmonary bypass.
The surgical treatment of the stentless valve implant can be summarized by three main steps as described in Figure 4.2.1 adapted from Glauber et al. (2007):

1. after transecting the ascending aorta for exposure, the diseased valve is excised (Figure 4.9(a));

2. the aortic annulus is sized with a dedicated aortic valve sizer (Figure 4.9(b));

3. stay sutures are placed and, subsequently, the valve is lowered: the prosthesis takes its position supra-annularly (Figure 4.9(c)).

The clinical outcomes of AVR are related to an appropriate choice of both prosthesis size and replacement technique. At present, the performance of the surgical operation is thus strictly dependent on surgeon's expertise, especially in consideration of the fact that the technique is non-trivial. Hence, all these aspects make AVR a strongly surgeon-dependent procedure. Moving from such considerations, in the present study we propose a patient-specific approach to optimize prosthesis sizing to support pre-operative planning of AVR.
Stentless aortic valve replacement has received very limited attention in computational studies and, in particular, to the author's knowledge, the evaluation of the impact of different sizes on coaptation and competence has not yet been dealt with. For this purpose, the technique for implant of a stentless biological aortic valve is studied through FEA, which nowadays represents a valid and spread methodology for biomedical investigation.
In particular, we simulate the implant of three different sizes of the Freedom Solo (Sorin Biomedica Cardio, Saluggia, Italy) stentless valve, starting from a single patient-specific aortic root model. Image processing procedures lead to a patient-specific computer-aided design (CAD) model of the aortic root wall which represents the host structure for the stentless valve. Each prosthesis is placed along three different supra-annular suture-lines, defining thus nine different scenarios. We evaluate, in particular, the coaptation height

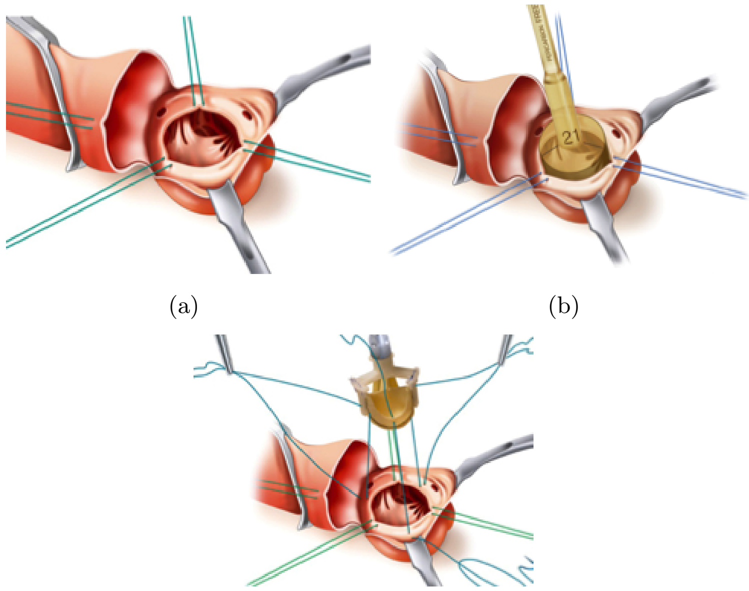

(a) (b)

(c)

Figure 4.9 *The three main steps of the stentless valve placement procedure: (a) excision of the diseased valve, (b) sizing of the aortic root and (c) placement of the prosthesis inside the aortic root.*

and area as well as the stress/strain state of the valve leaflets.

4.2.2 Materials and Methods

The methodological process adopted in this paper and summarized in Figure 4.10 consists of four principal steps:

1. a parametric CAD model of the supra-annular prosthesis is properly created;

2. the CAD model of the aortic root is obtained performing image processing procedures;

3. the AVR operation is mimicked by positioning the stentless tissue valve inside the aortic root through a placement simulation;

4. finally, a second simulation considering both aortic root and valve is performed to evaluate the valve competence during diastole.

In the following, we detail each one of the previous steps.

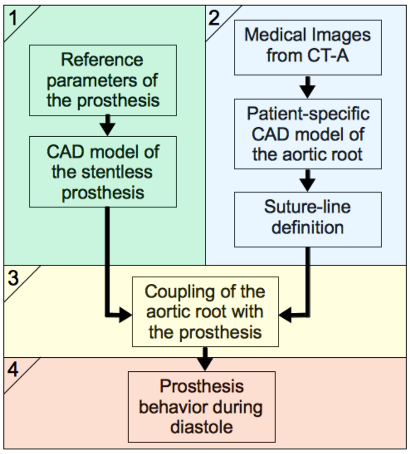

Figure 4.10 *Flow chart representing the logical process of the present work: a CAD model of the stentless prosthesis under consideration is properly created and coupled with the geometrical model of the aortic root, obtained directly from medical images. Once the prosthesis placement has been simulated, the stentless valve performance is evaluated virtually reproducing its behavior during diastole.*

Stentless prosthesis model

As stated by Xiong et al. (2010), the prosthetic leaflet geometry plays a key-role for efficacy and durability in AVR procedures and, for this reason, it is important to accurately reproduce it in order to predict the realistic valve behavior. In our study, in absence of prosthesis technical data from the manufacturer, we generate the model of the stentless valve assuming that the three leaflets to be implanted in the patient's aortic root have the same geometrical features of a healthy aortic valve [129]. Consequently, the Labrosse geometrical guidelines are adopted to define the model [26].
The Labrosse model of the aortic valve is completely described by five parameters as highlighted in Figure 4.11 [34]:

- the diameter of the annulus, D_a;
- the diameter of the top of the commissure, D_c;
- the valve height, H;
- the leaflet free margin length, L_{fm};
- the leaflet height, L_h.

The subcommissural triangles, i.e., the region included between the base circle of the annulus and the line of the leaflet attachment (the white area in Figure 4.11(a)), are properly removed.

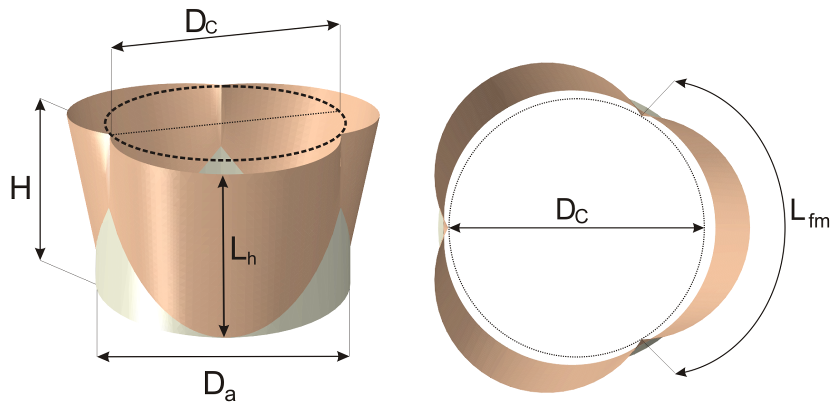

(a) (b)

Figure 4.11 *Geometric model of the valve by Labrosse et al. [26]: (a) the perspective view shows parameters D_a,D_c,H and L_h; (b) the top view highlights L_{fm} and, again, D_c.*

Three different valve models characterized by different sizes are created based on product specifications of the Freedom Solo prosthesis by Sorin Biomedica Cardio (Saluggia, Italy). Two main dimensions are reported in the product technical sheet [1]: the maximum diameter (corresponding to D_a in our model) and the prosthesis height, H_p. On the basis of these data, the whole set of the Labrosse parameters is obtained, as reported in Table 1.
In particular, given the diameter of the annulus, D_a, and the valve height, H, we can properly determine the diameter at the commissures, D_c, which is, in agreement with dimensions measured in normal human valves [44], $5 \div 10\%$ smaller than D_a.
The leaflet free margin length, L_{fm}, is chosen to be approximately $25 \div 30\%$ greater than D_a, according again to the same set of healthy valve data listed in Thubrikar et al. [44]. Finally, in the literature it is highlighted that L_{fm} should be "less than twice" than L_h [26] and also this condition is respected by the values reported in Table 4.1.

Prosthesis ID	D_a [mm]	D_c [mm]	H [mm]	L_{fm} [mm]	L_h [mm]
SIZE 25	25	23	17	31	17
SIZE 27	27	25	18	33	18
SIZE 29	29	27	19	36	19

Table 4.1 *Set of the chosen parameters highlighted in Figure 4.11 adopted to model the stentless prostheses.*

[1]In Appendix B the Freedom SOLO details are reported in terms of dimensions and design parameters

The leaflets are meshed within Abaqus v6.10 (Simulia, Dassáult Systems, Providence, RI, USA) using 4200 four node membrane elements M3D4R with 0.5 mm uniform thickness. A mesh convergence analysis has been performed on a single leaflet to identify the minimum number of elements required to predict the correct behavior during diastole. In Figure 4.12(a) the position of the nodes belonging to the line of symmetry (see Figure 4.12(b)) of the leaflet is reported as convergence analysis result.

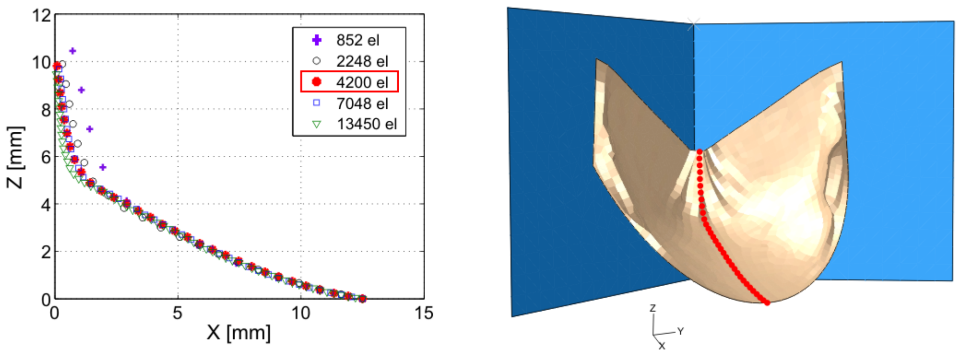

(a) (b)

Figure 4.12 *Mesh convergence analysis for a single valve leaflet: (a) the behavior of the leaflet during diastole is represented in terms of nodes position for different mesh dimensions; (b) nodes belonging to the line of symmetry of the leaflet are highlighted.*

Material

The stentless valve is made of two bovine pericardial sheets without any fabric reinforcement. Even though fresh pericardial tissue is anisotropic, the simplifying assumption of isotropic material is acceptable. in the literature, in fact, it is possible to find that since the prosthetic valve after the fixation process behaves more as an homogeneous isotropic material [130, 131].
Consequently, to represent the material behavior of the stentless valve leaflets we adopt an incompressible isotropic hyperelastic Mooney-Rivlin model, defined by the strain energy potential discussed in Section 3.2.3.
In particular, following the simplified approach proposed by Ranga et al. (2007), we adopt the following parameter values: C_{10} = 0.5516 MPa and C_{01} = 0.1379 MPa. The density is set to 1000 kg/m^3.
However, it is worth noting that material modeling of fixed pericardium is still a matter of debate. For this reason, in Appendix C such an issue is discussed in detail.

Patient-specific model of the aortic root

We base the aortic root model on DICOM images of a cardiac CT-A performed using a iodinate contrast die on a 46 year-old male patient who provided a written informed consent prior to undergoing CT-A. The CT-A scan is performed at IRCCS Policlinico San Matteo, Pavia, Italy, using a SOMATOM Sensation Dual Energy scanner (Siemens Medical Solutions, Forchheim, Germany). The scan data are characterized by the following features: slice thickness: 0.6 mm; slice width x height: 512x512; pixel spacing: 0.56 mm.
We process the resulting DICOM images using ITK-SNAP v2.0.0 [74] in order to firstly enhance the contrast die, then extract a confined region of interest (ROI) from the whole reconstructed body and, finally, apply an automatic segmentation procedure based on the *snake evolution* methodology [132] to obtain a stereolithographic (STL) description of the anatomical region of interest. In Figure 4.13(a) and 4.13(b) the evolution of the *snake* is shown from two different views, axial and longitudinal, together with the rendering of the resulting STL aortic bulb model (Figure 4.13(c)).

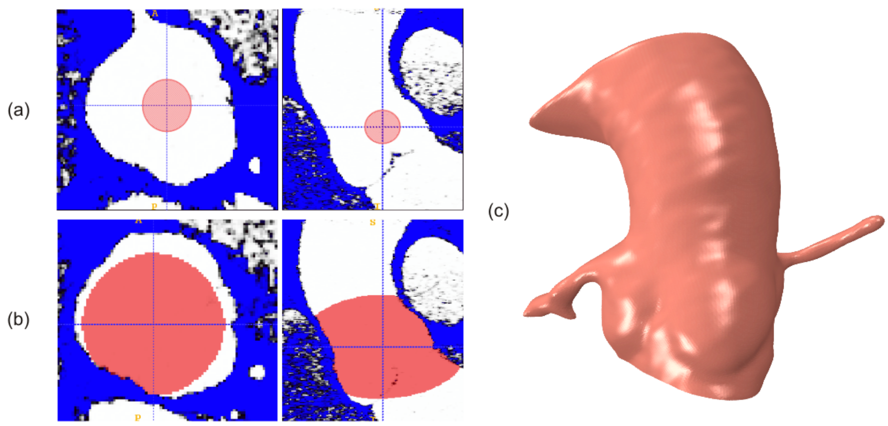

Figure 4.13 *DICOM image processing: (a) a starting snake is initialized as a circular bubble and placed inside the ROI defined by the contrast die; (b) the bubble evolves to take the shape of the aortic root; (c) the STL patient-specific model of the aortic bulb is obtained.*

The STL file is processed within Matlab (Natick, Massachusetts, U.S.A.) to define a set of splines identifying the cross sectional contours of the aortic bulb volume, as discussed in Section 3.1.2. The CAD model is then obtained by means of a lofting procedure from the spline curves imported in Abaqus. Finally, the model is meshed with 43260 linear quadrilateral shell elements S4R. The procedure to obtain the geometrical model and the mesh is summarized in Figure 3.25.

The same material properties already adopted for the prosthetic tissue valve are used also for the aortic root wall [92].

Prosthesis placement

As highlighted in Figure 4.14, the prosthesis implant is simulated by constraining the attachment lines of the leaflet (red lines in Figure 4.14) to overlap the so-called "suture-lines", defined on the patient-specific aortic root model (blue lines in Figure 4.14).

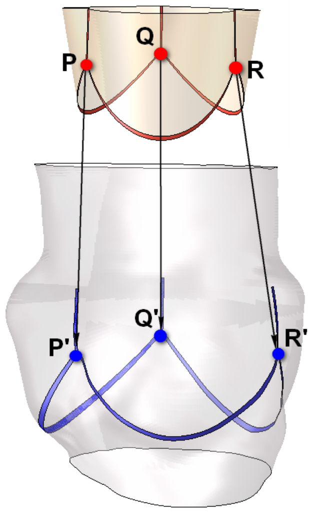

Figure 4.14 *Simulation strategy for the prosthesis placement: the black arrows represent the displacements to be computed and applied to the nodes of the prosthesis line of attachment (red lines).*

To define the suture-line of each leaflet we proceed in three steps:

- definition of the plane α passing through the reference points A, B, C and containing the line of the native leaflet attachment (see Figure 4.15(a));
- definition of the plane β, obtained with a Δs vertical translation of the plane α (see Figure 4.15(b));
- definition of the supra-annular suture-line from the intersection of β with the patient-specific CAD model of the Valsalva sinuses.

This sequence of geometrical operations is repeated for every Valsalva sinus to obtain the whole set of suture-lines (blue lines in Figure 4.15(b)).
A quasi-static FEA of the prosthesis placement is performed using Abaqus Explicit solver; precomputed displacements are imposed to the nodes of the prosthesis attachment line. Inertia forces do not dominate the analysis

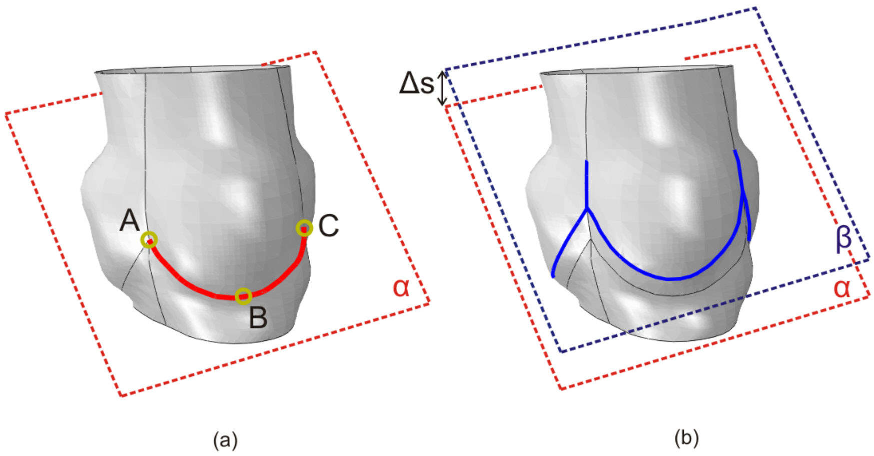

Figure 4.15 *Definition of the suture lines: (a) the plane α containing the native line of attachment and passing through the points A,B and C is created; (b) the plane β is obtained translating α vertically; the line of attachment of the prosthesis leaflet is defined by the intersection of β with the sinus. The blue lines represent the whole set of attachment lines where the nodes of the prosthesis are tied with the nodes of the sinuses.*

since the ratio of kinetic energy to internal energy remains less than 5%. For quasi-static simulations involving rate-independent material behavior, the natural time scale is in general not important. For this reason, a mass scaling strategy, i.e., an artificial increase of the mass of the model, is used to reduce computational costs.
Different values of Δs (0.5 mm, 2 mm and 5 mm) associated with three different labels we refer to in the Result section (suture-line 1, 2 and 3, respectively) are taken into consideration to evaluate the behavior of the valve implanted in different positions.

Prosthesis closure

To evaluate the performance of each valve replacement solution, i.e., each combination of prosthesis size and suture-line position, we simulate the diastolic phase of the cardiac cycle.
The CT-A data adopted to generate the geometrical model of the aortic root wall have been obtained at end-diastole; for this reason, a uniform pressure, $p = 80$ mmHg, is gradually applied on the leaflets, while the pressure acting on the internal wall of the sinuses is taken equal to zero. The nodes belonging both to the top and to the bottom of the aortic root model are confined to the plane of their original configuration.
In Figure 4.16 a representative sketch of the boundary conditions applied to

simulate valve closure is depicted.

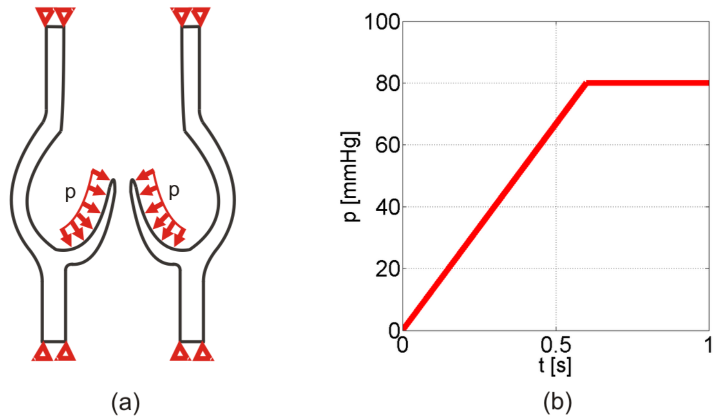

Figure 4.16 *Simulation of prosthesis closure: (a) sketch of the applied boundary conditions; (b) the pressure on the leaflets adopted to reproduce the diastolic phase is represented as a function of time.*

The numerical analysis of the prosthesis closure is a non-linear problem involving large deformation and contact. For this reason, Abaqus Explicit solver is used to perform large deformation analyses; in particular, quasi-static procedures are used again assuming that inertia forces do not change the solution. Kinetic energy is monitored to ensure that the ratio of kinetic energy to internal energy remains less than 10%. Also in this case, a mass scaling strategy is adopted to reduce computational costs.

4.2.3 Results and Discussion

Prosthesis placement

We evaluate the positioning of three different sizes of stentless tissue valves in one aortic root model. Each prosthesis is placed along three different supra-annular suture-lines, defining thus nine different scenarios.
The FEA of the stentless valve implantation into the patient-specific aortic bulb provides the tensional state of each leaflet. As depicted in Figure 4.17, the results of the prosthesis placement in one particular case are reported in terms of von Mises stress pattern.
It is possible to note that the stress distribution is not the same for each leaflet; this is due to the asymmetric morphology of the host aortic bulb, while the stentless valve has a symmetric shape.
To highlight this aspect we compute the von Mises average stress, σ_{av}, properly defined over each leaflet. To neglect peak values of the stress due to local concentration, we consider only the 99 percentile with respect to the original leaflet area (i.e., only 1% of the area has stress above this value, σ_{99}).

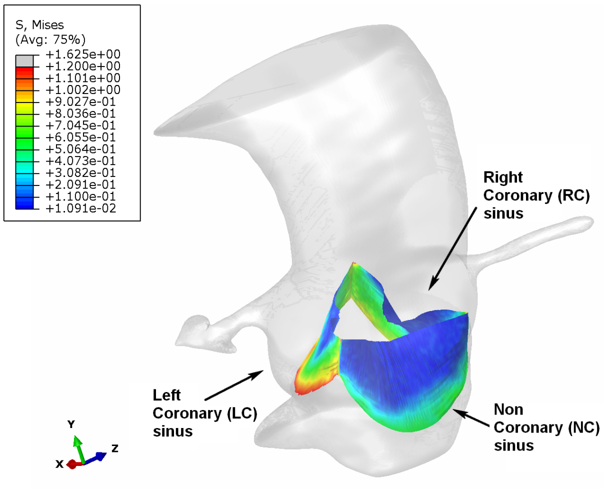

Figure 4.17 *The von Mises stress contour plot, outcome of the simulation of the SIZE 25 prosthesis implant on the suture-line 1 (Δs = 0.5 mm), is represented. The Non Coronary (NC), the Left Coronary (LC) and the Right Coronary (RC) sinuses are shown.*

After excluding the elements with the higher stress values, we compute the average stress, σ_{av}, as:

$$\sigma_{av} = \frac{\sum_{i=1}^{N} \sigma_i A_i}{\sum_{i=1}^{N} A_i} \tag{4.2.1}$$

where σ_i is the stress evaluated at the centre of each element, A_i is the element area and N is the number of elements whose stress value is below σ_{99}. In Table 4.2 all the values of σ_{av} (kPa) obtained from the analysis of the prosthesis placement on different suture-lines are summarized.

Table 4.2 *Stress distribution in terms of σ_{av} (kPa) over the leaflets after the simulation of surgical prosthesis placement. The effect of the suture site and of the prosthesis size is highlighted for each leaflet (left-coronary, LC, non-coronary, NC and right coronary, RC).*

	SIZE 25			SIZE 27			SIZE 29		
	LC	NC	RC	LC	NC	RC	LC	NC	RC
sut.-line 1 ($\Delta s = 0.5mm$)	509	137	390	259	47	175	100	42	63
sut.-line 2 ($\Delta s = 2mm$)	698	212	520	417	77	286	195	11	107
sut.-line 3 ($\Delta s = 5mm$)	945	364	728	632	161	459	370	41	245

In Figure 4.18(a) and 4.18(b) σ_{av} is evaluated in the three leaflets (Non/Left/Right Coronary) and represented as a function of the prosthesis size and suture-line position respectively.

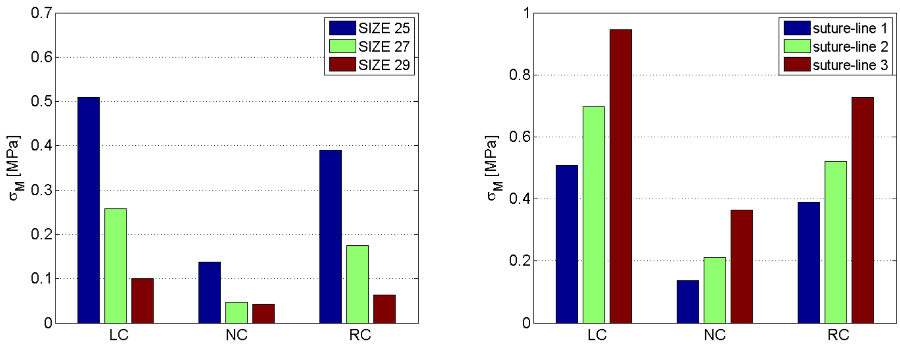

(a) (b)

Figure 4.18 *Stress distribution over the leaflets: (a) as a function of the prosthesis size with fixed suture-line position (suture-line 1), (b) as a function of the suture-line position with fixed prosthesis size (SIZE 25).*

Prosthesis closure

Once the prosthesis is implanted and sutured inside the aortic root, a uniform pressure is applied on the leaflets to evaluate the performance of the surgical solution under consideration. In Figure 4.19, the SIZE 25 valve placed along suture-line 1 is represented at the end of the diastolic phase; the von Mises stress distribution is highlighted.

Two basic parameters are measured to evaluate the prosthesis physiology: the coaptation area, A_C, defined as the total area of the elements in contact, and the coaptation height, H_C, defined as the distance between the plane containing the annulus and the point where the coaptation occurs (see Figure 4.20).

The bar graphs depicted in Figures 4.21(a) and 4.21(b) show the impact of both the prosthesis size and the suture-line position on the coaptation measurements. In particular, Figure 4.21(a) highlights that the increase of prosthesis size leads to the decrease of H_C, while the suture-line position does not affect significantly the coaptation height.

On the contrary, both the coaptation area, A_C, and the average stress, σ_{av} (defined in Equation 4.2.1), increase with the prosthesis size while the suture-line site has a minor impact on such values (see Figure 4.21(b) and 4.21(c)). In Table 4.3 the values of σ_{av} (kPa) are reported for each investigated configuration.

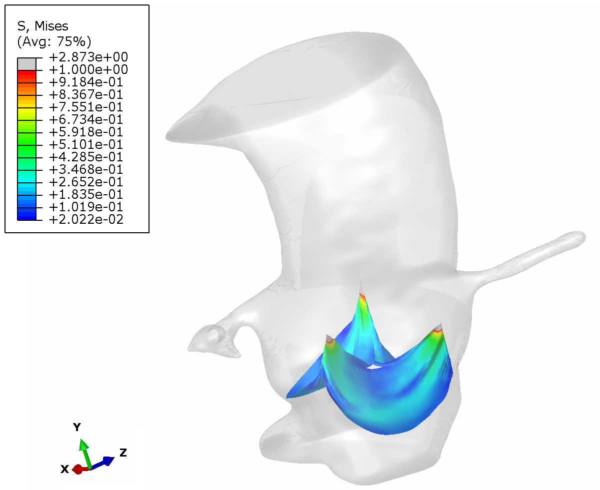

Figure 4.19 *The von Mises stress contour plot is represented at the end of diastole for the SIZE 25 prosthesis implanted on the suture-line 1: a central gap is observable proving that the prosthesis size under consideration is not able to completely close and will allow a retrograde blood flow during diastole.*

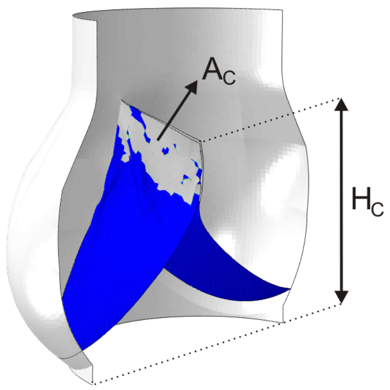

Figure 4.20 *Section view of the prosthesis at the end of diastole: the coaptation area, A_C, highlighted in grey and the coaptation height, H_C, are shown.*

Table 4.3 *The values of σ_{av} (kPa) are reported at the end of diastole for each investigated configuration.*

Prosthesis ID	sut.-line 1 ($\Delta s = 0.5mm$)	sut.-line 2 ($\Delta s = 2mm$)	sut.-line 3 ($\Delta s = 5mm$)
SIZE 25	215	211	212
SIZE 27	228	218	210
SIZE 29	239	234	228

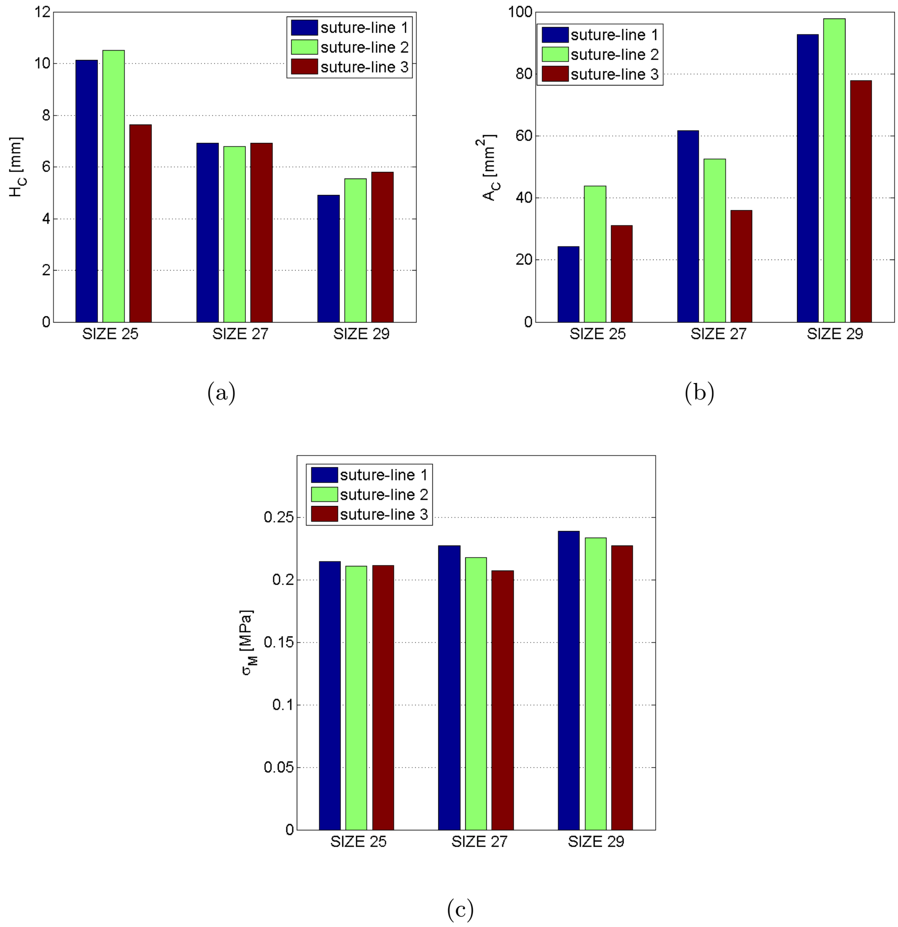

Figure 4.21 *Trend of the coaptation measures and of the tensile state: (a) the coaptation height, H_C, (b) the coaptation area, A_C and (c) the average von Mises stress, σ_{av}, are evaluated as a function of the prosthesis size and the suture-line position.*

The valve closure results show that the coaptation of the three leaflets is not perfectly symmetric due to the physiological asymmetry of the aortic sinuses. For this reason, during the diastolic phase, a central gap is observable (see Figure 4.22, front view) which implies insufficiency of the virtually implanted valve. Consequently, we can speculate that the replacement solution under investigation could fail.

In the literature, several finite element studies of the aortic valve are reported [29, 31, 36, 91] but, to our knowledge, the behavior of stentless valve prostheses with particular attention to the evaluation of the impact of different sizes on coaptation and competence, has not yet been dealt with.
In this work, we simulate by FEA the aortic valve replacement procedure

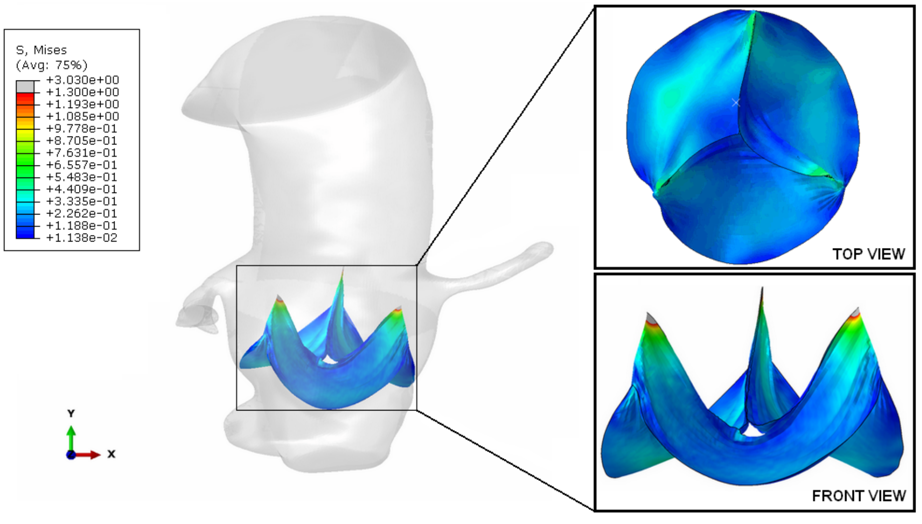

Figure 4.22 *SIZE 29 prosthesis placed on suture-line 2 at the end of diastole: due to the asymmetry of the patient-specific sinuses, the non-coronary leaflet of the virtually implanted symmetric valve closes below the other two leaflets. A central gap is highlighted from the front view which means that the replacement solution fails.*

with a stentless tissue valve. Different prosthesis sizes have been placed on different suture-line positions defined over one patient-specific aortic root model, directly obtained from CT-A images.
The discussion of results of the present study may focus on the following issues.
The first one is the uneven distribution of stresses on the three leaflets (see Figure 4.18(a) and 4.18(b)) due to anatomical asymmetry of the native aortic bulb in spite of uniformity of the prosthetic valve. Consistently, the simulation of valve closure displays a non-uniform coaptation of the leaflets (as depicted in Figure 4.22) during the diastolic phase, which means a potential incompetence of the substituted valve, i.e., the failure of the applied surgery. We highlight that our geometrical solution due to asymmetry is in agreement with the results presented by Sun et al. [133] who studied the implications of an asymmetric trans-catheter aortic valve deployment.
The second issue is the relevance of prosthesis size as to both the coaptation area, i.e., the performance of the prosthetic valve (see Figure 4.21(b)), and the stress distribution over the leaflets, i.e., the durability of the prosthesis (see Figure 4.21(c)), whereas no significant impact has been shown by the suture-line site. This observation highlights importance of the choice of prosthesis size while it seems that suturing the valve in a position slightly more distal or more proximal with respect to conventional suture sites (i.e., at 2-3mm from the host annulus of each sinus [119]) does not affect signifi-

cantly the procedure outcome.
The computational reproduction of the patient aortic root from imaging records (namely CT-A) as well as the reproduction of the candidate prosthetic valve by the same means allows a matching of both, which implies potential surgery choices better tailored to the specific patient.
Conclusively, the computational tools may provide a deeper insight in physiology of heart valves in terms, for example, of stress/strain patterns and adequacy of coaptation, easily moving from native to prosthetic models. Practically speaking, they may help the surgeon improve his technique choosing the optimal devices and they may anticipate the surgery outcome as well. So they are worth moving forward in the direction warranted by the present study.

Open problems

With regard to limitations of the study, the first observation is that the computational model of the aortic root has to be replicated on a number of cases. Confirmatory value has to be searched for in postoperative measured parameters compared to the numerical results.
Even though the geometrical modeling of the tissue prostheses featured as healthy valves is accepted [129], the creation of prosthetic geometries completely based on technical data of valves released on the market would improve the computational outcomes and contributions to support the surgical planning. In this direction, also the consideration of more accurate material models would represent a step forward heading to more realistic simulations.
Finally, a numerical study of the fluid-structure interaction between the prosthesis leaflets and blood could give additional information about the surgical procedure planning and, in particular, it could make possible to evaluate the impact of different AVR solutions on the hemodynamics.
In future works, we are planning to further improve the model including all these aspects.

4.3 Transcatheter aortic valve implant

Heart valve failure represents a considerable contribute to cardiovascular diseases, the leading cause of death in Western countries. Until recently, such a severe pathology has been treated adopting open-heart surgery techniques and cardiopulmonary bypass. However, over the last decade, minimally-invasive procedures have been developed to avoid high risks associated with conventional open-chest valve replacement techniques.
In particular, percutaneous valves are adopted to restore valve functionality: a heart valve, sewn inside a stent, is crimped and properly placed in the patient's heart by means of a catheter. Such a recent and innovative procedure represents an optimal field for investigations through virtual computer-based simulations: nowadays, in fact, computational engineering is widely used to deepen many problems belonging to the biomedical field of cardiovascular mechanics and, in particular, minimally-invasive procedures.
In this study, we focus on a balloon-expandable valve and we propose a novel simulation strategy to reproduce its implantation by means of computational tools. In particular, finite element analysis is performed to simulate the surgical procedure moving from a patient-specific aortic root model obtained by processing medical images. Prosthesis positioning in two different cases (distal and proximal) have been evaluated in terms of coaptation area and average stress.

4.3.1 Background

The increase of life expectancy and, consequently, of population average age has favored the genesis and progression of degenerative cardiovascular disease. In particular, aortic valve stenosis due to calcification is the most frequent aortic valve disorder [3, 134]. In this case, aortic valve replacement represents the most common surgical remedy.
However, open heart surgery with cardiopulmonary bypass is not always recommended: in presence of coexisting conditions such as advanced age, congestive heart failure, coronary artery disease, lung disease and renal insufficiency, the surgical risk becomes very high and, in some cases, unsustainable.
For this reason, since 1986 Cribier et al. [135] introduced percutaneous transluminal valvuloplasty to reduce the aortic valvular gradient and improve left ventricular ejection. Nevertheless, such a treatment provided very poor mid and long-term outcome [136] and the associated risks and follow-up events have been subject of concern since the incidence of restenosis has been found approximately 50% at 6 to 12 months [137].
New developments in cardiothoracic surgery have led to innovative minimally-invasive devices for the treatment of aortic stenosis in patients associated with potential high surgical risk. In 2002, Cribier performed the first clin-

ical implant of a percutaneous balloon-expandable aortic valve at the level of the native valve [138] while, in 2004, Grube implanted for the first time a self-expandable transcatheter valve [139].
In the last decade, different devices have been designed and submitted to clinical evaluation confirming that, on one hand, such an innovative technique represents a promising solution for aortic stenosis even though, on the other hand, at present, it is still an immature procedure due to limited follow-up data and durability evaluation.
The two transcatheter devices currently available consist of either a stainless steel balloon-expandable or nitinol self-expandable stent. A trifoliate bovine/porcine pericardium heart valve is attached inside the cylindrical metallic frame.
In this context, finite element analysis (FEA) represents an innovative computational technique being not only an integral part of the design process, but also a predictive tool able to anticipate the area of localized stress, the post-operative coaptation as well as possible modes of failure, thus representing a support to clinicians during the decision-making process, as highlighted by Fann et al. [140].
In the last decade, many studies have demonstrated that FEA may be successfully used in the field of biomechanics to predict the performance of cardiovascular prosthetic devices implanted in patient-specific geometries [141, 142, 143].
In this work, we focus on the balloon-expandable Edwards SAPIEN valve studying the device by means of FEA with the aim of better understanding its mechanics from crimping to deployment in a patient-specific aortic root and, in particular, we present a novel simulation strategy to investigate crucial aspects of transcatheter aortic valve (TAV) implantation such as the impact of prosthesis positioning on its post-implant performance.
Prosthesis placement can be achieved by either a transfemoral or transapical access. In the first case, the prosthetic device is inserted through the femoral artery and passes retrogradely through the aorta until the aortic root is reached [144] while, in the second case, it is placed directly through the apex of the heart [145].
Once the valve has been positioned, balloon inflation leads to the valved stent expansion which excludes and compresses the native diseased leaflets. Positioning is crucial since it affects post-operative performance: on one hand, the implanted valve must guarantee regular flow through the coronaries while, on the other hand, the prosthesis should not overlap and crush the left bundle branch [146]. Computer-based simulations represent an extremely powerful tool both to anticipate post-implant performance and to evaluate in advance implications of specific placement sites.
To the authors' knowledge, at present, there are no computational works on TAV implant which take into consideration the whole device, even though percutaneous valves have recently received a lot of attention by computa-

tional scientists and many studies are reported in the literature.
Schievano et al. [114] and Capelli et al. [113] proposed a FEA-based methodology to provide information and help clinicians during percutaneous pulmonary valve implantation planning. In these works, the implantation site has been simplified using rigid elements and, at the same time, the presence of the valve has been neglected.
On the contrary, many other studies focus on the leaflets neglecting the stent: for example, Smuts et al. [147] developed new concepts for different percutaneous aortic leaflet geometries by means of FEA; Sun et al. [133] improved the understanding of mechanics involved in TAV devices exploring asymmetric deployment.
Moreover, Sirois et al. [148] provided fluid simulations of TAV deployment into a patient-specific aortic root and, finally, hemodynamics after TAV implantation has been studied using computational fluid dynamics to determine both energy loss [149] and migration forces [150].
Up to now, to the best of our knowledge, as previously mentioned, no structural computational study has been yet addressed to investigate post-implant TAV behavior considering both a realistic stent model and the valve leaflets, which is the intention of this work.
It is not our goal in this work to accurately model the device under investigation, not even to virtually mimic an intervention that has already been performed aiming at comparing our results with postoperative measurements. Instead, we attempt to present a novel computational framework with the main intention of assessing a step-by-step strategy representing a solid base that may be improved in order to reproduce as realistically as possible both the implant procedure and the postoperative performance of a transcatheter aortic device.

4.3.2 Materials and Methods

The simulation procedure is quite complex and can be summarized in seven principal steps:

1. creation of stent model;
2. simulation of stent crimping;
3. creation of the aortic root model;
4. simulation of balloon inflation and stent expansion;
5. creation of prosthetic valve model;
6. simulation of valve mapping onto the deployed stent;
7. simulation of valve closure.

In the following, each step is detailed.

Step 1: creation of stent model

In absence of both a device sample and design data from the manufacturer, we base the creation of the stent geometry on the few data and pictures available on the official web-site of the Edwards Lifesciences [151].
For the sake of simplicity, assumptions are made about the geometry of the prosthesis. We firstly create the net of the stent using Rhinoceros software v.4.0 (McNeel & associates, Seattle, WA, USA) observing that it is made of a primitive geometry, represented in Figure 4.23a, mirrored and replicated. In Figure 4.23b the net of the stent is represented and the main dimensions are reported.

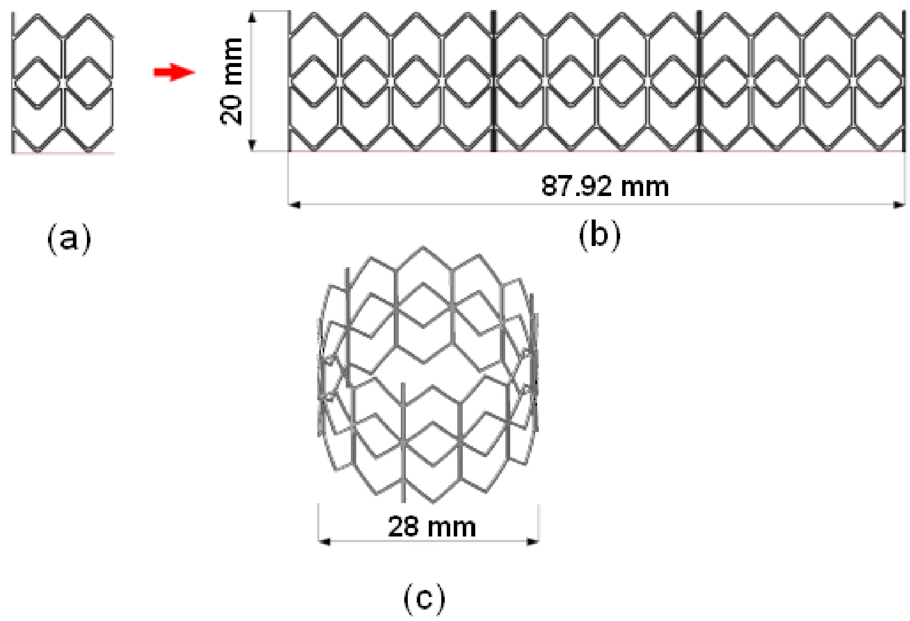

Figure 4.23 *Creation of stent model: (a) a primitive geometry is mirrored and replicated to obtain the (b) whole planar model; (c) the nodes of the planar configuration are then expressed in terms of polar coordinates to get the characteristic circular shape.*

Once the unfolded geometry of the stent has been created, we mesh it using Abaqus software v6.10 (Simulia, Dassault Systéms, Providence, RI, USA) obtaining a list of nodes and elements. To such nodes we can assign proper polar coordinates easily computed from their original cartesian coordinates to obtain the folded geometry depicted in Figure 4.23c.

Step 2: simulation of stent crimping

A cylindrical catheter is gradually crimped leading to stent deformation. The initial diameter of the catheter is 28 mm while the final diameter is 7 mm in agreement with the work of Capelli et al. [113]: the stent undergoes large deformations as highlighted in Figure 4.24 where the first and last crimping phases are shown.

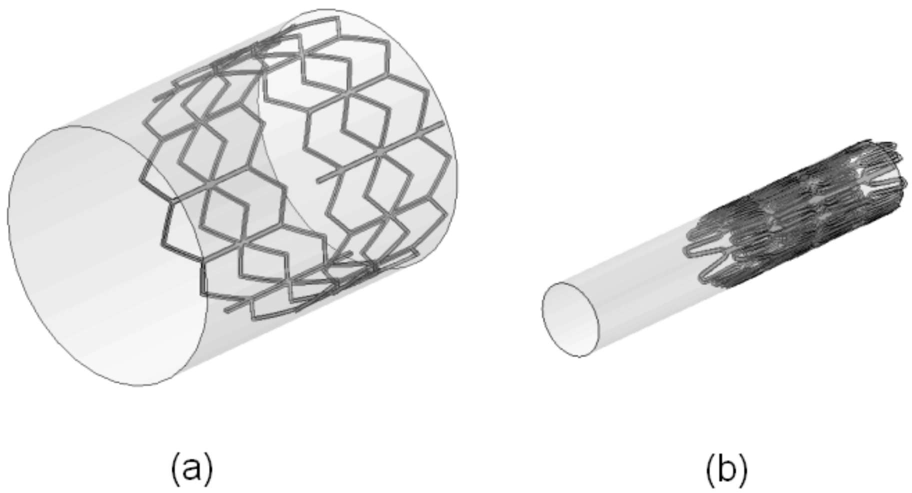

Figure 4.24 *Simulation of stent crimping: (a) at the beginning a rigid catheter is created around the undeformed geometry of the stent; (b) the catheter is gradually crimped leading to the stent deformation.*

A quasi-static simulation is performed using Abaqus/Explicit; the kinetic energy is monitored to ensure that inertial effects do not affect the results. The catheter is meshed using 403 4-node surface elements with reduced integration (SFM3-D4R) and it is modeled as a rigid material; the stent has been discretized using 90279 solid elements with reduced integration (C3D8R). The material used for the balloon-expandable stent is the low carbon 316L stainless steel, whose behavior is described by an elastoplastic model according to the work of Auricchio et al. [152].
A frictionless general contact is used to handle the interactions between the catheter and the stent.

Step 3: creation of the aortic root model

The aortic root model is obtained by processing DICOM images of a cardiac CT-A performed using a iodine contrast die on a 46 years old male patient. The CT-A scan has been performed at IRCCS Policlinico San Matteo, Pavia, Italy, using a SOMATOM Sensation Dual Energy scanner (Siemens Medical Solutions, Forchheim, Germany). The scan data are characterized by the following features: slice thickness, 0.6 mm; slice width x height, 512x512;

pixel spacing, 0.56 mm.
The processing procedure has been performed using OsiriX software v3.9 [73] to extract a stereolitographic representation (STL) of the aortic root under investigation (see Figure 4.25a). The obtained STL file has been elaborated using Matlab (The Mathworks Inc., Natick, MA, USA) to generate the aortic root mesh: we firstly define a set of closed lines representing the cross sectional profile of the inner aortic root wall; the outer profile is then reconstructed imposing a radial shift of the inner profile considering a uniform thickness of 1.3 mm for the Valsalva sinuses [153] (see Figure 4.25b). The final step consists in defining the hexaedral-element mesh between the inner and outer boundaries as depicted in Figure 4.25c.

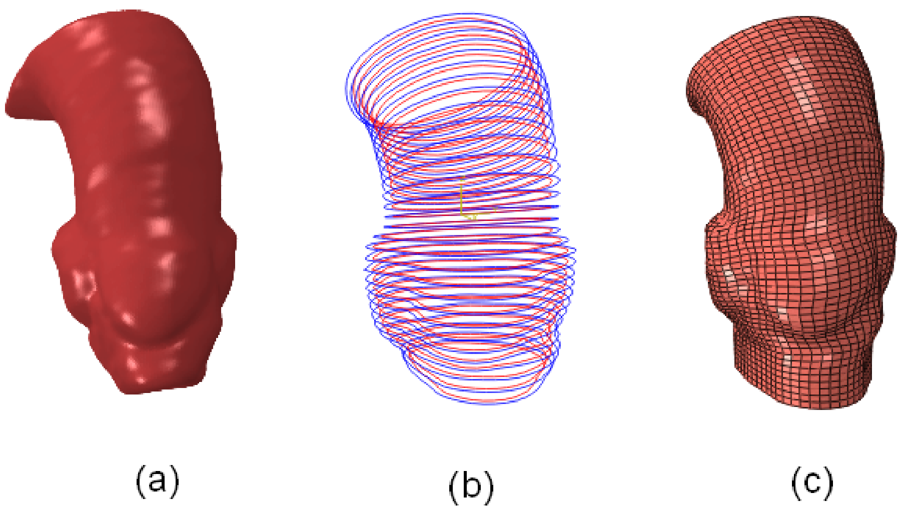

Figure 4.25 *Creation of aortic root model: (a) an STL file is extracted by processing the DICOM images; (b) the inner (red) and outer (blue) splines identifying the aortic root wall are defined from the STL file; (c) an hexaedral-element mesh is then created.*

The aortic root wall has been modeled adopting realistic constitutive laws accounting for non-linearity and anisotropy: the aortic sinuses are, in fact, made of a fiber-reinforced material where the fibers, corresponding to the collagenous component, are embedded in an isotropic hyperelastic matrix of elastin.
Several constitutive laws of arterial tissue are available in the literature based on large deformation theory and accounting for fibers. In this work, as previously discussed in Chapter 3, we adopt the model proposed by Holzapfel et al. [154] since it is available in the material library of Abaqus [81].
The dispersion of the fibers is assumed to be negligible, i.e. $\kappa = 0$, which means that the fiber are perfectly aligned. Since the two fiber–families are mechanically equivalent, we have $k_{11} = k_{12} = k_1$ and $k_{21} = k_{22} = k_2$.

As no information on the collagen fiber orientation is available for the investigated material, we also assume the angle β defining such an orientation to be an unknown parameter.
The calibration is carried out through a standard optimization technique which requires the minimization of the objective function χ^2 defined as the squared sum of the differences between the experimental data and the related model prediction variable.
The results of the fitting procedure have been shown in Section 3.2.4 and reported in Table 3.4 (first row).

Step 4: simulation of balloon inflation and stent expansion

The simulation of stent apposition is performed assembling (i) the crimped stent, whose tensional state is imported from the crimping simulation and it is assumed as a predefined field, (ii) the balloon modeled as a cylindrical folded body with two conical tapered ends and (iii) the patient-specific aortic root. The whole assembly is shown in Figure 4.26.

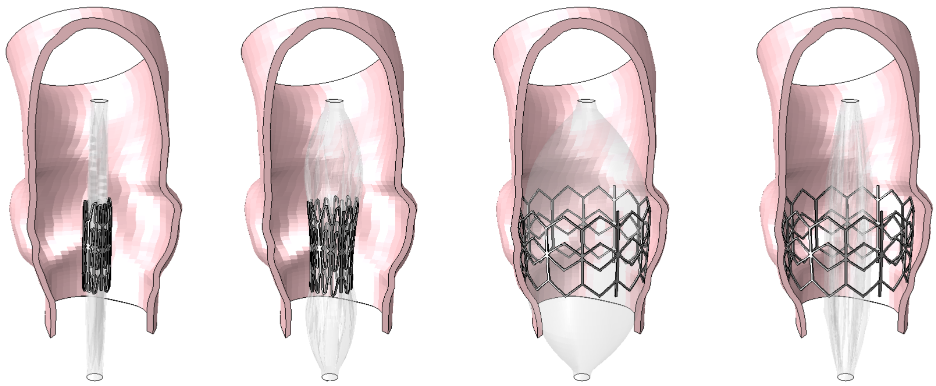

(a) (b) (c) (d)

Figure 4.26 *Different frames of balloon expansion and stent apposition: (a) initial configuration; (b) the balloon starts to deploy the stent; (c) the balloon is fully expanded and the stent fully deployed; (d) final configuration after balloon deflation.*

The balloon model is discretized with 13680 3-node membrane elements (M3D3); the Duralyn material properties are assigned [155].
Once the balloon-stent system has been properly placed inside the aortic root model, Abaqus/ Explicit solver is again used to perform the expansion simulation: a uniform pressure of 1 MPa is gradually applied to the inner surface of the balloon while its fixation to the catheter is virtually reproduced by constraining the displacements in each direction of the proximal and distal balloon tips. The complex contact problem of the balloon interacting

with itself and the stent is described by a Coulomb friction model with a friction coefficient of 0.2.

Step 5: creation of prosthetic valve model

The prosthetic valve model is generated through a lofting procedure starting from the circular line of the bottom and the peculiar line of the top of the valve extracted from the real device picture (see Figure 4.27a). The two closed lines have to be concentric and, in particular, the top line has to be inscribed into the circular base whose radius is equal to the inner radius of the stent as shown in Figure 4.27b.

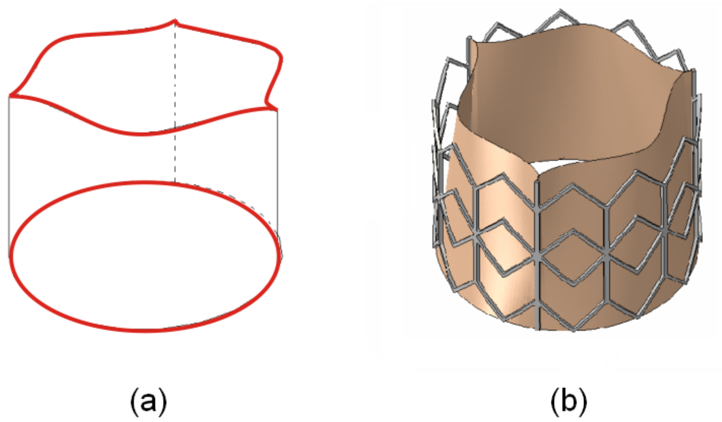

Figure 4.27 *The Edwards SAPIEN model: (a) the valve is created by means of a lofting procedure performed between the bottom and top curve highlighted in red; (b) the whole device model made of the stent and the valve is shown.*

The valve leaflets are made of glutaraldehyde-treated bovine pericardium that we model as an isotropic material following the theses proposed by Lee et al. [130] and Trowbridge et al. [131].
In particular, we consider a simple isotropic nearly-incompressible hyperelastic material exploiting a linear relationship between the Cauchy stress and the logarithmic strain measures and characterized by a Young modulus of 8 MPa, a Poisson ratio of 0.49, and a density of 1100 kg/m^3: such values are within the statistical range of the fixed pericardial tissue [29, 156].

Step 6: simulation of valve mapping onto the deployed stent

Once the simulation of balloon expansion has been completed and the stent is placed within the aortic root, we perform a quasi-static simulation to map the valve onto the implanted stent. In particular, we compute the displacement field of two different sets of valve nodes: (i) the nodes lying on

the line of attachment with the stent and (ii) the nodes of the circular base of the valve.
Finally, the overlapping nodes of the stent-valve system are tied together. The result of the mapping operation is shown in Figure 4.28.

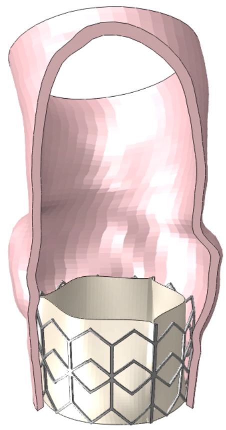

Figure 4.28 *The implanted Edwards SAPIEN device: after performing a mapping procedure to map the valve leaflets onto the stent, we obtain the model of the whole transcatheter device implanted in the patient-specific aortic root.*

Step 7: simulation of valve closure

The last step of the procedure to simulate TAV implantation consists in the simulation of valve closure with the aim of evaluating its performance. The diastolic phase of valve closure has been reproduced by gradually applying a uniform pressure to the leaflets. The nodes of the aorto-ventricular junction and of the sinotubular junction belonging to the patient-specific aortic root model have been constrained; the displacements of the nodes at the base of the valve are constrained as well.
The numerical analysis of the prosthesis closure is a highly non-linear problem involving large deformations and contact. For this reason, the Abaqus/Explicit solver is used to perform the simulations; in particular, quasi-static procedures are used, assuming that inertia forces do not affect the solution. Kinetic energy is monitored to ensure that the ratio of kinetic to internal energy remains below 10%.

4.3.3 Results and Discussion

The simulation procedure described in the previous section has been performed in two different cases: in particular, we have explored the implications related to the Edwards SAPIEN positioning by focusing on two different implantation sites.

Moving from the same patient-specific aortic root model, we have simulated TAV implantation both proximally and distally, which means, in the first case, immediately below the coronary ostia and, in the second case, 7 mm below the distal position.

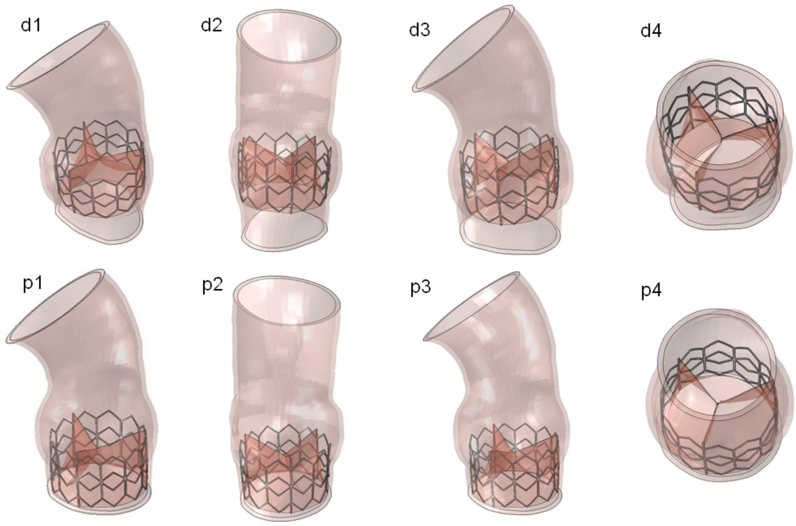

Figure 4.29 *Different views of the implanted transcatheter valve: (d1-d4) the distal positioning; (p1-p4) the proximal positioning.*

Different views of the two configurations are represented in Figure 4.29. The post-operative valve performance is then evaluated in terms of coaptation area and stress distribution on the leaflets, as highlighted in Figure 4.30a,b.

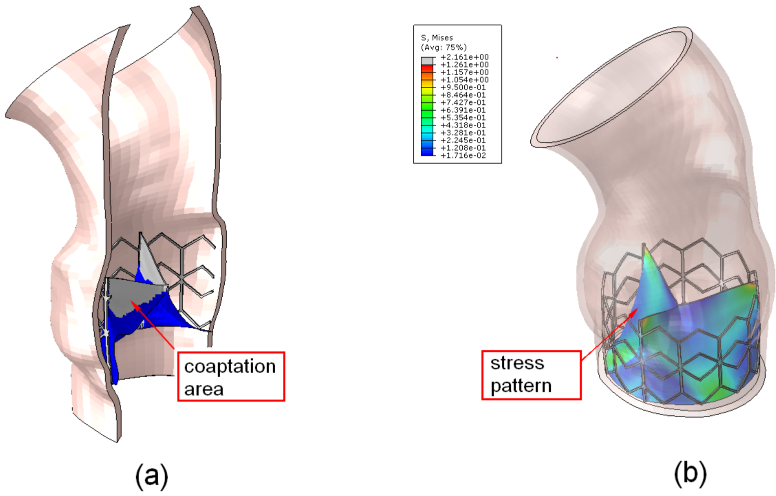

Figure 4.30 *Simulation results: (a) the coaptation area is highlighted; (b) the leaflet tensional state (MPa) is reported.*

To neglect peak values which can be affected by local effects we consider only the 99 percentile with respect to the original leaflet area (i.e., we neglect the 1% of the area characterized by the highest stress values) and we compute the average stress, σ_{av} according to Equation 4.2.1. The value of σ_{av} in the proximal position results equal to 229 kPa versus an average von Mises stress value in the distal position of 260 kPa.
On the contrary, we measure a coaptation area of 340.5 mm^2 for the closed valve placed in the proximal position while the valve positioned distally shows a reduced coaptation area of 258.2 mm^2.
The obtained results in the two investigated configurations are summarized in Table 4.4.

Table 4.4 *Results of prosthesis performance simulation.*

	Coaptation Area [mm^2]	Average stress [kPa]
Proximal	340.5	229
Distal	258.2	260

Valve replacement following open-heart surgery is nowadays the gold standard procedure in case of aortic valve disease even though the whole field of surgery is heading towards minimally-invasive techniques which hold many advantages such as: (i) less trauma on the patient's body due to avoidance of general anesthesia with long-acting drugs, (ii) smaller incisions and, consequently, less post-operative pain, (iii) shorter hospital stays and recovery time.
In the last decade, valved stent which can be implanted percutaneously have been also developed for heart surgery to repair stenotic valves. Both advanced age and related pathologies and comorbidities make such an innovative approach recommended and, sometimes, essential since, for these patients, the surgical risk is prohibitive.
Inevitably, the implant of a trans-catheter valve, which is a relatively young technique, has some limitations. At present, the durability of the procedure is a critical aspect as well as the high surgical risk in case of an eventual re-intervention.
Safety, reliability, and efficacy are goals for the immediate future as well as essential prerequisites to promote minimally invasive procedures (i.e., valved stents) with respect to standard surgical treatments to restore valve functionality.
In this context, advanced computational techniques may play a crucial role, not only as an integral part of the design process but also to predict post-operative prosthesis performance and, consequently, to help surgeons in identifying the optimal device for a specific patient. Anatomical variability and morphological alterations due to pathology would warrant specific devices tailored to specific patients. In our work, we use finite element anal-

ysis to obtain realistic representations of the surgical intervention directly moving from medical images.
Computer-based simulations allow the prediction of valve performance which can be evaluated in terms of coaptation area and stress/strain field. The former gives a direct anticipative indication of the efficacy of the non-invasive repair procedure while the latter highlights localized stresses/strains on the prosthesis, identifying the weakest point of the implanted device, as well as on the aortic root, giving a direct indication of vessel injury. Both of them may guide surgeons during operation planning and may support them in choosing the optimal device for a specific patient.
The results presented in our work represent a possible application of virtual simulations. In particular, we focus on the impact of different implantation sites on valve performance. To the best of our knowledge, no computational studies are available in the literature taking into account patient-specific geometries as well as the whole transcatheter aortic device made of both the stent and the valve.
The obtained values of coaptation area and average stress demonstrate that there are not significant differences in placing the valved stent either proximally or distally, even though we can speculate that the proximal implant should be preferable since it leads to a greater coaptation area, preventing retrograde blood flow, and a lower stress, indicating a minor tensional state which can be correlated to prosthesis failure.

Open problems

The computational framework to simulate TAV implant is not trivial and already quite close to reality. However, in order to achieve a better representation of the performed clinical procedure so to get more reliable predictive results, many limitations should be overcome:

- we should create more accurate models of the aortic root; in particular, we may include the native leaflets which will be crushed and compressed by the valved stent. Moreover, we know that is mechanically incorrect to adopt root dimensions from CT-A, recorded under physiological pressure and combined with constitutive equations where the material is supposed to start from the unloaded configuration: the evaluation of the pre-stress exceeds the purposes of this work even though it should be considered.

- We should create also more accurate models of the SAPIEN device, properly modeling all its structural and geometrical details.

- Studying fluid dynamics would further improve our model; in particular we may evaluate the post-operative hemodynamic performance which is of significant interest for clinicians.

- Finally, the adopted methodology based on finite element analysis should be validated comparing our preliminary results with in-vivo post-implant measurements. Once the modeling strategy has been refined, a clinical protocol should be set up to compare, possibly for a large number of patients, simulation results with post-implant measurements.

Besides the intrinsic limitation related to the complex system under investigation, we conclude that the proposed methodology offers a useful tool to evaluate a balloon-expandable valve implant aiming at anticipating surgical operation outcomes.

Chapter 5

Final remarks

Recently, a new era in medical research has been initiated in which prediction by means of computer-based simulations has been used to support physicians' experience and skill.
Within this work, a computational framework to analyze postoperative outcomes of aortic valve surgery is presented.
In particular, finite element analysis (FEA) has been used to simulate different surgical strategies to restore aortic valve function moving from patient-specific models and with the aim of giving in advance useful information to clinicians to support the decision-making process.
Hence, the doctoral research activity may be collocated in the field of computational biomechanics, which is based on a multidisciplinary approach, as it involves at the same time physiology and mechanics, anatomy and image processing procedures, histology and numerical analysis.
Collaborations with different structures representing different disciplines (ranging from structural engineering to medicine) and, in particular, interactions with surgeons and physicians turn out to be essential for proceeding towards realistic applications in clinical practice.
Therefore, during the doctoral program different working relationships have been established; in the following, a brief list of the main active collaborations is reported:

- Department of Cardiothoracic Surgery of IRCCS Policlinico San Matteo, Pavia, Italy (headed by Prof. M. Viganó);
- Centre for Inherited Cardiovascular Diseases of IRCCS Policlinico San Matteo, Pavia, Italy (headed by Prof. E. Arbustini);
- Institute of Radiology of IRCCS Policlinico San Matteo, Pavia, Italy (headed by Prof. F. Calliada);
- Heart Surgery Division of IRCCS Policlinico San Donato, Milano, Italy (headed by Prof. A. Frigiola);

- Cardiovascular Engineering Group of the Institute of Computational Engineering and Science (ICES), University of Texas at Austin, Texas, USA (headed by Prof. T.J.R. Hughes);

In this chapter, we briefly look back over the work carried out during the doctoral research resuming the obtained results and also highlighting the open problems and future developments.

5.1 Conclusion

Chapter 2 puts in evidence the complexity of the object of the study, i.e., the aortic valve. Generally, in fact, in dealing with anatomical regions, structure and function are strictly related: in particular, each component of the aortic valve is characterized by a complex and peculiar geometry which can be also subjected to alteration due to pathology.
Different imaging techniques can be adopted to accurately capture the valve morphology: echocardiography, magnetic resonance and computed tomography are the most commonly used diagnostic tools, each of them carrying advantages and drawbacks to be carefully evaluated during the geometric modeling procedure.
Realistic geometrical models obtained from appropriate diagnostic tools, in fact, represent the starting point for realistic simulations.
Moreover, material models able to reproduce anisotropy, thus including histological information, as well as physiological boundary conditions have to be considered aiming at virtually mimicking the (preoperative, diseased but also postoperative) aortic valve behavior.

In **Chapter 3**, the finite element method is introduced with particular focus on aortic valve models. The whole modeling procedure is described in detail: first of all, the methodology adopted to create patient-specific geometries and meshes is discussed. In dependence on the imaging source, different models characterized by a different grade of accuracy may be obtained elaborating and processing the recorded data.
Then, we go through the material modeling procedure both highlighting some basic theoretical aspects and describing the anisotropic model elected for the computer-based analysis.
Finally, the simplified boundary conditions considered to mimic the interaction between the aortic valve and blood are presented.

Within **Chapter 4**, three different applications of the finite element method in the field of aortic valve surgery are presented.
A patient-specific computational strategy (summarized in Figure 1.5) has been developed with the aim of predicting surgical outcomes, thus supporting surgeons during the operation planning procedure.

- Aortic valve sparing (AVS) is a surgical technique proposed for the first time by Tirone David in 1992 which restores aortic valve function maintaining the native leaflets of the patient. Tirone David himself stated in 2002 that valve sparing procedures remain *more art than science.*
  The proposed methodology provides an innovative tool based on computational analysis to identify in advance (i.e., preoperatively) the optimal surgical solution for a specific patient.
  In particular, we create the pathologic dilated valve of one specific patient and we simulate eight different operative configurations (2 graft types and 4 sizes).
  The simulation results, reported in terms of clinical parameters (length, height and distance of coaptation), highlight the optimal solution based on physiological values clinically identified by transthoracic echo evaluations.

- In case of aortic valve stenosis due to calcific and diseased leaflets, aortic valve replacement (AVR) represents a common surgical remedy: the leaflets are excised and substituted by a prosthetic valve which can be either mechanical or biological.
  The second application of FEA presented in this work deals with AVR with stentless biological valves and, even in this case, aims at optimizing the clinical choice of prosthesis size, highlighting, at the same time, the effects of different positioning.
  DICOM data from CT-scan have been processed to get the aortic root geometry enabling the simulation of prosthesis implant which has been performed for three different prosthesis sizes placed along three different supra-annular sites, thus defining 9 scenarios.
  The coaptation parameters as well as the stress/strain patterns have been evaluated and considered as comparison terms for the predictive election of the optimal stentless device to be implanted.

- Finally, transcatheter aortic valve implant (TAVI) is a recent minimally-invasive technique which can be performed in case of severe aortic stenosis in patients at high surgical risk.
  In this work, a novel computational methodology has been proposed allowing simulations of the stented device implantation in a patient-specific aortic root obtained by processing CT-A images.
  The application of the finite element approach to investigate TAVI is very recent (2010) and, to our knowledge, there are no studies mimicking by means of FEA the implant of the whole prosthetic device (stent+valve).
  We have found that positioning, which is a crucial aspect of this procedure, affects the postoperative performance of the implanted valve,

evaluated in terms of average stress on the leaflets and length of coaptation during diastole.

5.2 Future work

"*All models are wrong, some are useful*" (G. Box).
In dealing with models, it is of fundamental importance the identification of a trade off between model accuracy and result reliability. Our aortic valve models can be certainly improved even though the adopted simplifying assumptions may be considered acceptable for the outlined goal.
Within this work, we have realized a complex simulation strategy to simulate aortic valve surgery, able to predict operation outcomes moving from patient-specific data. From the performed finite element analyses, qualitative and quantitative information have been obtained which may guide surgeons during the decision-making process.
However, removing some simplifying assumptions may lead to models able to approach reality more closely.
In the following, the main future developments for the present work are summarized.

- **Geometrical models**
  The performed procedure to get patient-specific models of the aortic valve provides accurate geometries. Anyway, an improvement in this direction is represented by making it completely automatic. So far, in fact, the segmentation, contrast enhancement and filtering operations are made manually using OsiriX. Even though, once the know-how has been acquired, the time required by the procedure remains acceptable (less than 1 hour when starting from good quality images), automatic image processing procedures would help in reducing the total time necessary to assess the computational methodology, which is a very important aspect for the optimization of the decision-making process. With respect to prosthetic models, we tried to reproduce their geometry moving from the few data reported on the specification sheet. Of course, the possibility to obtain either more technical details or a sampling device from the manufacturer would warrant more realistic results.

- **Material models**
  During the research program, we moved from simplified isotropic material models for both the root and the leaflets to more complex anisotropic constitutive laws. In particular, to model anisotropy, we took into consideration the model proposed by Holzapfel in 2000 for mainly two reasons: 1) it has been proven to be accurate for vascular walls; 2) it is already implemented within the adopted finite element solver.

This choice carries some drawbacks. First of all, as discussed in Chapter 3, the Holzapfel model is able to accurately capture the anisotropic behavior of the aortic sinuses while it seems that it is not the optimal solution for modeling the aortic leaflets. Consequently, different models for the two constitutive elements of the aortic valve should be used.
Moreover, the considered model has been calibrated from experimental data on human aortic specimens and does not account for residual stresses and *in-vivo* loading due to blood pressure; such conditions are frequently referred to as pre-stress.
Future developments would focus on the study of the pre-stress effects on the aortic root anatomy.

- **Boundary conditions**
  In dealing with the boundary conditions defined to simulate aortic valve behavior, the major limitation to our work consists in reproducing the interaction between blood and aortic structure by simply applying a uniform gradient of pressure. No fluid-structure interaction (FSI) has been performed.
  However, simulation results in terms of coaptation parameters and stress/strain patterns may be considered reliable even though the action of blood on both the leaflets and the root is simply modeled applying a distributed load.
  In the literature, few works proposing an FSI study of the aortic valve have been published and, in our opinion, the challenge of reproducing the interaction between blood and leaflets has not been solved yet due to the complexity of the problem involving large deformations, contact and added mass effects.
  In future works, we are planning to further improve the model including this aspect.

Despite modeling improvements, another crucial aspect deserves a specific discussion, i.e., the validation of the performed simulations.
Within the field of biomechanics and, in particular, in dealing with the aortic valve behavior, it is not trivial to validate the results obtained by means of numerical analyses. In vitro tests of a particular surgical procedure are almost impossible so that postoperative in vivo measurements represent the main direction in order to validation.
Our results demonstrate that it is possible to predict through FEA different postoperative configurations of the aortic valve and preliminary measurements in very few real cases seem to confirm the validity of the computational approach. Of course, this is not sufficient to state that the procedure is validated: large scale studies involving a large number of patients, need to be addressed. A strict and efficient collaboration with surgeons and radiologists is required and *ad hoc* protocols have to be defined.

To prove the intention of proceeding in this direction, in Appendix D we report the three protocols defined together with the doctors and submitted to our medical collaborators which might provide a validation of the methodological computer-based process developed in the doctoral research.

Appendix A

Isogeometric analysis

THE concept of Isogeometric Analysis has been firstly introduced by Hughes et al. in 2005 in order to integrate CAD and FEA. In particular, "a primary goal is to be geometrically exact no matter how coarse the discretization. Another goal is to simplify mesh refinement by eliminating the need for communication with the CAD geometry once the initial mesh is constructed. Yet another goal is to more tightly weave the mesh generation process within CAD" [75].
As already mentioned in Chapter 3, NURBS are basic concepts invoked by isogeometric analysis since they are the industry standard for design and geometric representation. NURBS are special cases of rational B-spline curves which, being piecewise polynomial, overcome the inadequacy of curves consisting in just one polynomial [157]. In the following, we aim at introducing the basic notions and definitions dealing with such a new analysis technique.

A.1 Basic concepts

Let firstly define a *knot vector* as a nondecreasing sequence of real numbers: $\Xi = \{\xi_1, ..., \xi_{n+p+1}\}$, where $\xi_i \leq \xi_{i+1}$ for $i = 1, ..., n+p+1$, p is the polynomial order, n is the number of basis functions used to construct a B-spline curve. The ξ_i are called *knots*; their multiplicity has direct implications on the properties of the bases.
A knot vector is called *open* if its first and last term have multiplicity $p+1$. Repeating the first and last knot $p+1$ times means that the basis is interpolatory at the boundary of the domain and, moreover, fully discontinuous resulting in C^{-1} continuity.
The i-th basis function of order p is defined recursively according to the Cox - de Boor formula. Details are widely discussed in [1].
A tensor-product NURBS surface of order p in the ξ-direction and q in the η-direction is defined by:

$$\mathbf{S}(\xi,\eta) = \frac{\displaystyle\sum_{i=1}^{n}\sum_{j=1}^{m} N_{i,p}(\xi)M_{j,q}(\eta)w_{i,j}\mathbf{B}_{i,j}}{\displaystyle\sum_{i=1}^{n}\sum_{j=1}^{m} N_{i,p}(\xi)M_{j,q}(\eta)w_{i,j}} \qquad 0 \leq \xi,\eta \leq 1, \tag{A.1.1}$$

where the $\mathbf{B}_{i,j}$ are the *control points*, vector-valued coefficients of the basis functions forming a bidirectional *control net*, the $w_{i,j}$ are the weights, while $N_{i,p}(\xi)$ and $M_{j,q}(\eta)$ are the basis functions corresponding respectively to the knot vectors:

$$\begin{aligned} \Xi &= \left\{ \underbrace{0,...,0}_{p+1},\ \xi_{p+2},...,\xi_i,...,\ \xi_n, \underbrace{1,...,1}_{p+1} \right\} \\ \mathcal{H} &= \left\{ \underbrace{0,...,0}_{q+1},\ \eta_{q+2},...,\eta_j,...,\ \eta_m, \underbrace{1,...,1}_{q+1} \right\} \end{aligned} \tag{A.1.2}$$

A.2 Mapping procedure: NURBS patient-specific models

In the field of biomechanics, the creation of patient-specific geometries of the anatomical district of interest is a very important task in order to carry out simulations as close as possible to reality. This is the reason why we need to perform a mapping operation.
The mapping procedure aims at finding the best choice of the control points involved in the definition of a target surface evaluated, for example, at a set of N sampling points (N must be greater than or equal to the total number of control points, $n \cdot m$).
From Eq. A.1.1 derives the matrix formulation for each component of the N points:

$$S^r(l) = \frac{\mathbf{N}_\xi(k,:) \cdot \mathbf{B}^r \mathbf{w} \cdot \mathbf{M}_\eta^T(:,h)}{\mathbf{N}_\xi(k,:) \cdot \mathbf{w} \cdot \mathbf{M}_\eta^T(:,h)}, \tag{A.2.1}$$

where $k = 1,...,nx$, nx is the number of sampling points along the ξ-direction; $h = 1,...,ny$, ny is the number of sampling points along the η-direction; $l = k + (h-1)nx$; $r = 1,2,3$ indicates the three spatial components of sampling and control points.
$\mathbf{N}_\xi$ and $\mathbf{M}_\eta$ are the collocation matrices containing the values of the basis functions along ξ and η-direction. In particular, the j-th column of the collocation matrix contains the values of the j-th basis function at all the entries of a pre-defined vector t. The i-th row contains the value of all the basis functions computed at $t(i)$. As a consequence, the dimensions of $\mathbf{N}_\xi$

and $\mathbf{M}_\eta$ are respectively (nx, n) and (ny, m).
Due to the simplifying assumption of constant weights, the denominator is just a known constant for each equation.
Taking advantage of:

$$\mathbf{N}_\xi(k,:) \cdot \mathbf{B} \cdot \mathbf{M}_\eta^T(:,h) = (\mathbf{N}_\xi(k,:) \otimes \mathbf{M}_\eta^T(:,h)) : \mathbf{B} = \mathbf{C}(l,:) \cdot \mathbf{B}_{vec} \quad \text{(A.2.2)}$$

where $\mathbf{B}_{vec}$ is the column vector containing the homogeneous control points (obtained from $\mathbf{B}$ proceeding row-wise) and $\mathbf{C}(l,:)$ is the row vector containing the elements of:

$$\mathbf{N}_\xi(k,:) \otimes \mathbf{M}_\eta^T(:,h) \quad \text{(A.2.3)}$$

obtained proceeding again row-wise. From Eq. A.2.2 we may write the system:

$$\mathbf{S}^r = \mathbf{C} \cdot \mathbf{B}_{vec} \quad \text{(A.2.4)}$$

where $\mathbf{C}$ is the matrix whose rows are $\mathbf{C}(l,:)$.

Finally, solving the rectangular system for $\mathbf{B}_{vec}$ in the least-square sense, we obtain the r-th component of the control points.
The procedure described here above is now illustrated in the case of an aortic root mapping.
For this example, a NURBS cylinder is probably the best choice to start. The cylinder surface is obtained by sweeping a circle along a distance h, i.e., by the tensor product of a circle and a straight line. One possible way to construct the NURBS circle to be swept is piecing together three arcs of 120° using a seven-point triangular control polygon [157].

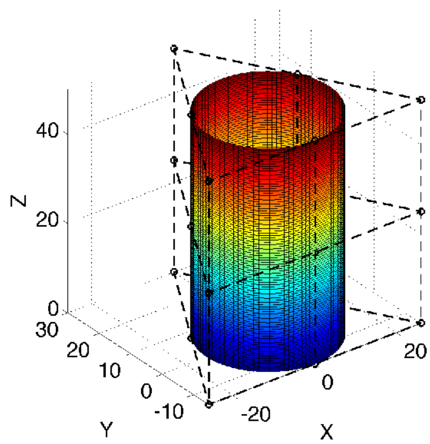

Figure A.1 *A seven-point triangle-based NURBS cylinder (R = 15, h = 50): the control mesh is shown*

In Figure A.1 a NURBS cylinder example is shown with the associate control polygon. In order to get a better reproduction of the patient's aortic root we firstly increment the number of basis functions defining the NURBS surface (and consequently the number of control points) by a knot insertion. The original knot vectors $\Xi = \{\xi_1, \xi_2, ..., \xi_{n+p+1}\}$ and $\mathcal{H} = \{\eta_1, \eta_2, ..., \eta_{m+q+1}\}$ are extended to $\bar{\Xi} = \{\bar{\xi}_1 = \xi_1, \bar{\xi}_2, ..., \bar{\xi}_{n+\bar{n}+p+1} = \xi_{n+p+1}\}$ and $\bar{\mathcal{H}} = \{\bar{\eta}_1 = \eta_1, \bar{\eta}_2, ..., \bar{\eta}_{m+\bar{m}+q+1} = \eta_{m+q+1}\}$ such that $\Xi \subset \bar{\Xi}$ and $\mathcal{H} \subset \bar{\mathcal{H}}$ [1]. In Figure A.2 the result of the knot insertion operation is highlighted.

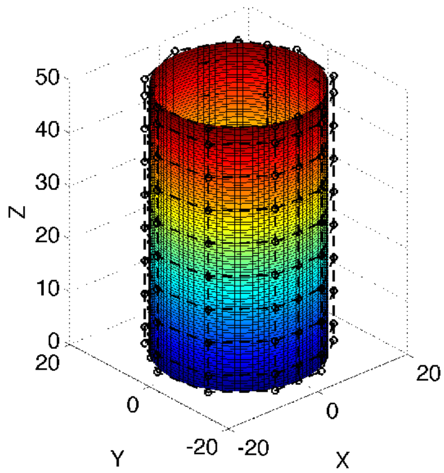

Figure A.2 *The same cylinder of Fig. A.2 obtained after performing a knot insertion procedure increasing the number of control points both along ξ and η direction*

The final result of the mapping operation is shown in Figure A.3.

A.2.1 The aortic valve leaflet model

Proved that the mapping procedure does work even in case of complex geometry we now want to focus our attention on a possible way to perform isogeometric analysis. Hence, we take into account the geometry of an aortic valve leaflet which is a simpler model than the whole aortic root.
From CTA images is extremely difficult to catch the leaflet geometry; for this reason we substitute the cloud of points coming directly from DICOM files with the nodes of a finite element mesh defined over the leaflet model constructed following Labrosse geometrical guidelines [26]. The model due to Labrosse takes into account two main simplifying assumptions:

- the three leaflets are identical in size and properties, laying at 120° from each other in the circumferential direction;
- the planes going through the base of the valve and the top of the commissures, which are formed by the mural regions where two leaflets insert side by side along parallel lines, are parallel.

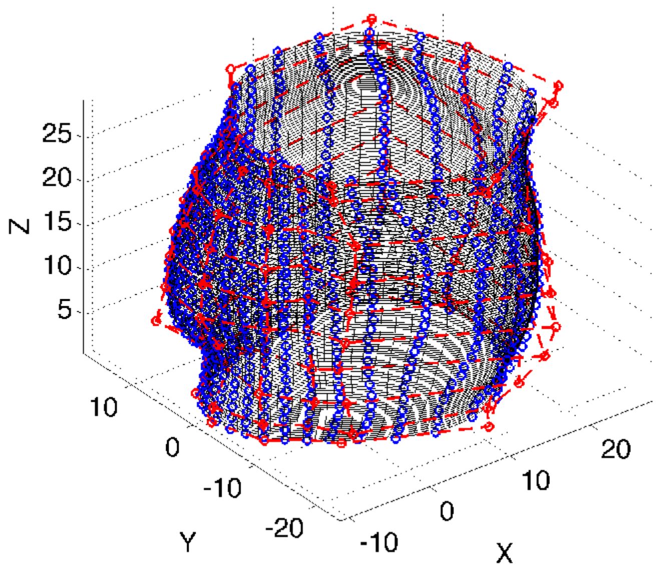

Figure A.3 *The NURBS surface of a patient-specific aortic root and its associated control mesh resulting from the mapping procedure starting from the DICOM data treated in Section 3.1.2*

In Figure A.4 a finite element mesh of the Labrosse leaflet is shown.

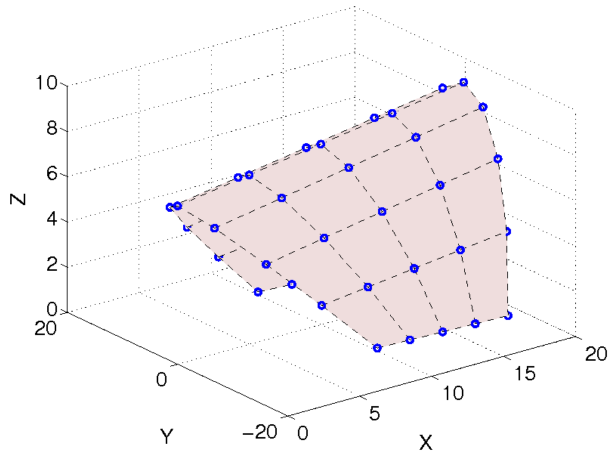

Figure A.4 *Finite element mesh of the aortic valve leaflet due to the Labrosse model: the nodes are involved in the mapping operation to get a NURBS leaflet surface*

Figure A.5 represents the NURBS model of the aortic valve leaflet obtained by means of the mapping procedure starting from a simple primitive rectangle.

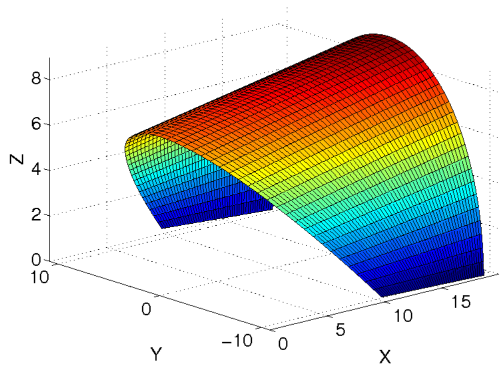

Figure A.5 *NURBS model of the aortic valve leaflet*

A.3 The analysis input

Given a NURBS surface (e.g., the aortic valve leaflet), one possible way to perform isogeometric simulations is to write an appropriate input file for LS-Dyna (Version 971-R4.2, Livermore Software Technology). Within its structure, in fact, a generalized Reissner-Mindlin shell element [158] has already been implemented. Such a formulation allows to separate the generation and evaluation of the basis functions (to be defined through the input file) from the analysis processes [159].
The creation of the input-file mainly needs to fulfill two requirements:

1. the definition of the parent generalized element

2. the definition of the interpolation nodes and elements.

1. In dealing with isogeometric analysis is important to observe that each element has its own parent element instead of standard finite elements which refer to a unique element. For the definition of the parent generalized element, after choosing an appropriate number of quadrature points, we have to compute and write in the input-file for each Gauss point both its weight and the values of all the basis functions and their derivatives along the two directions ξ and η.

2. Moreover, the interpolation nodes and elements have to be defined for contact and visualization. In particular, with respect to the contact, the necessity to approximate the surface involved in the contact with bilinear quadrilateral interpolation elements is a consequence of the lack of an explicit definition of the geometric boundaries of the generalized elements. Additionally, bilinear interpolation elements have to be defined in order to view the results of the simulations since the most of the finite element visualization software only display linear elements. Details are discussed in

[159].
A simple way to define such nodes and elements is based on Bezier extraction of NURBS surfaces [160].
Bezier elements and control points are computed by means of proper extraction operators which map a piecewise Bernstein polynomial basis onto a B-spline basis.
Recalling notation used in Section A.2, let $\bar{\Xi}$ and $\bar{\mathcal{H}}$ be the global knot vectors in the ξ and η direction (in our case uniform and open), eventually extended by a knot-insertion, defining the parametric mesh of the NURBS surface.
Each Bezier element corresponds to each element on the bivariate parametric domain; consequently, the number of Bezier elements will be equal to $ns\xi \cdot ns\eta$, where $ns\xi$ and $ns\eta$ are the number of knot spans in $\bar{\Xi}$ and $\bar{\mathcal{H}}$, respectively.
The A-th ($A = 1, ..., ns\xi \cdot ns\eta$) bivariate element extraction operator to compute the control points of the A-th Bezier element is accomplished by the tensor product of the i-th and j-th univariate element extraction operators, $\mathbf{C}_\xi^i$ and $\mathbf{C}_\eta^j$:

$$\mathbf{C}_A^e = \mathbf{C}_\eta^j \otimes \mathbf{C}_\xi^i, \tag{A.3.1}$$

where i and j are mapped to the element number such that $A = ns\xi(i-1)+j$.
How compute the univariate Bezier extraction operators is discussed again in [160].
The Bezier control points represent the extra-nodes defining the quadrilateral elements that interpolate the results of the computations.
In Figure A.6 an example of Bezier extraction for the aortic valve leaflet is presented: the Bezier control mesh (red markers) and the original control mesh (blue circles) are shown.

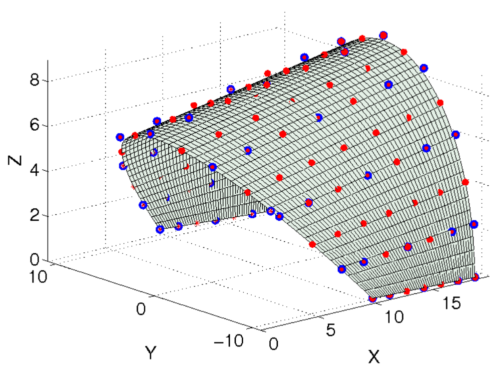

Figure A.6 *The Bezier control points (red markers) are obtained by extracting the NURBS leaflet surface. The original control points (blue circles) are highlighted as well*

In Figure A.7 the whole procedure leading to the writing of the LS-Dyna input-file is summarized through a flow chart.

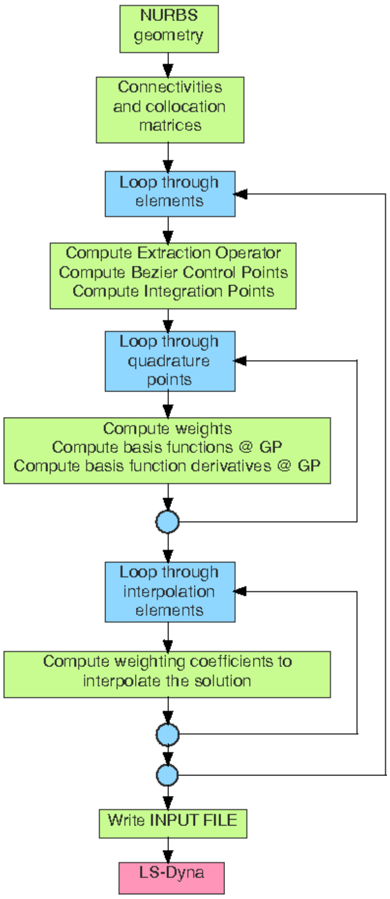

Figure A.7 *Flow chart summarizing the steps to achieve all the data to be written in the LS-Dyna input-file*

Appendix B

Freedom SOLO details

In Table B.1 the dimensions of the Freedom SOLO valve reported on the prosthesis technical sheet are presented.

REF.	ART 23 SG	ART 25 SG	ART 27 SG
Ordering Code	ICV0902	ICV0903	ICV0904
A [mm]	25	27	29
H_p [mm]	21	22	23

Table B.1 *Set of the Freedom SOLO dimensions from the manufacturer.*

Figure B.1 highlights how such dimensions refer to the prosthesis geometry.

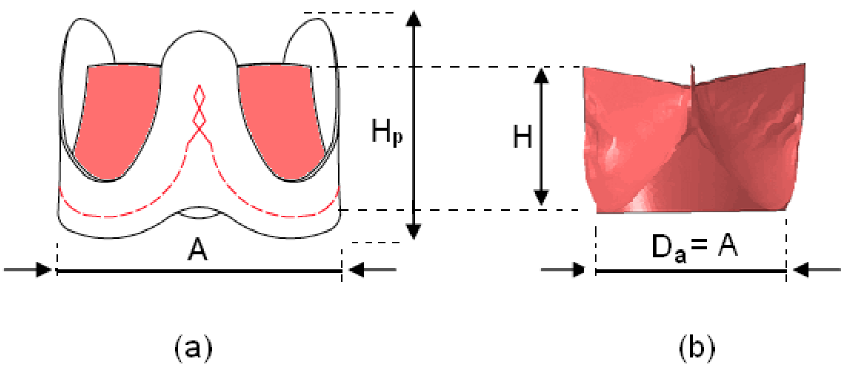

Figure B.1 *(a) The geometrical model of the prosthesis as reported in the technical sheet is showed; (b) the two basic dimensions of our closed valve model with reference to the technical sheet data are highlighted.*

Appendix C

Modeling fixed pericardium

BIOPROSTHETIC heart valve leaflets are essentially made of glutaraldehyde-treated bovine pericardium. Even though, on one hand, it is well accepted that the bovine pericardium behaves as an anisotropic material [161, 162, 163], on the other hand, there are different beliefs concerning the characteristics of the bovine pericardium after the fixation process which was introduced to minimize antigeneticity and maximize biochemical stability of the tissue, preventing in this way autolysis and degradation [164]. Moreover, cross-linking induced by fixation is strictly dependent on both the methods of fixation, particularly on the initial stress condition [165], and on the mechanical properties of the native, unfixed bovine pericardium.

Langdon et al. [166] carried out experimental tests on glutaraldehyde-treated bovine pericardium subjected to an equibiaxial load, obtaining stress-strain curves qualitatively showing anisotropy in all testing conditions. Even Arcidiacono et al. [20], who performed uniaxial tensile tests on thirty glutaraldehyde-fixed bovine pericardial specimens, stated that the tissue presents different mechanical response depending on the direction of the applied force.

On the contrary, Lee et al. [130] suggested that, even if fresh pericardial tissue exhibits anisotropy, it may be considered fully isotropic after the fixation process. The same thesis has been proposed by Trowbridge et al. [131], who considered fixed bovine pericardium to be isotropic.

Herein, we analyze the impact of an anisotropic model on both the stress patterns and post-operative coaptation parameters. In particular, the effects of the use of an isotropic hyperelastic material model for the valve leaflets are compared with those of a fiber-reinforced orthotropic one [154] taking into account oriented fiber distributions calibrated on experimental curves from tensile tests on glutaraldehyde-treated bovine pericardium [166]. In particular, for the valve leaflets we consider two different material models in order to evaluate the influence of the considered constitutive law on the performance of the replacement technique.

C.1 Isotropy vs anisotropy

In the first case (material A), we consider a simple isotropic nearly-incompressible hyperelastic material exploiting a linear relationship between the Cauchy stress and the logarithmic strain measures and, in particular, characterized by a Young modulus of 8 MPa, a Poisson ratio of 0.49, and a density of 1100 kg/m^3: such values are within the statistical range of the treated pericardial tissue [29, 156].
In the second case (material B), we model the leaflets using the incompressible anisotropic model proposed by Holzapfel et al. [154] already discussed in Chapter 3.
The material parameters are extracted from the biaxial tests on glutaraldehyde-fixed bovine pericardium tissue carried out by Langdon et al. [166] using a nonlinear least square method. Such an optimization technique requires the identification of both the experimental stress data and the related theoretical values. The experimental data are obtained from the literature [166] where the material response is reported in terms of Cauchy stress versus engineering strain.
From the best fitting procedure (see Chapter 3), the coefficient c_{10} results equal to 0. Since the use of null values of c_{10} leads to unstable, non-physiological phenomena during the numerical simulations, we force such a parameter to assume non-null values by imposing an appropriate boundary constraint. The introduced expedient implies a non-optimal correspondence between experimental data and fitted values for low stretches.
The trade-off between an accurate result from the fitting procedure and a physiological stable solution of the finite element analyses leads to the estimated parameter values reported in Table C.1. The associated curve fitting is shown in Figure C.1.

Table C.1 *Material parameters obtained fitting the experimental data on bovine pericardium reported by Langdon et al. [166]*

	c_{10}(kPa)	k_1(kPa)	k_2(−)	β(deg)
pericardium	20.10	54.62	30.86	29.8

The obtained orientation angle β highlights that the collagen fibers are preferentially oriented along the base-to-apex direction of the pericardium, in agreement with experimental evidences, making this the least extensible direction (see Figure C.1). In fact, it is known that valve leaflets are much stiffer in the circumferential direction, i.e., collagen fibers are preferentially oriented in the circumferential direction [18, 23]: consequently, the base-to-apex direction of the bovine pericardium corresponds in our prosthesis model to the circumferential direction of each leaflet, as shown in Figure C.2.

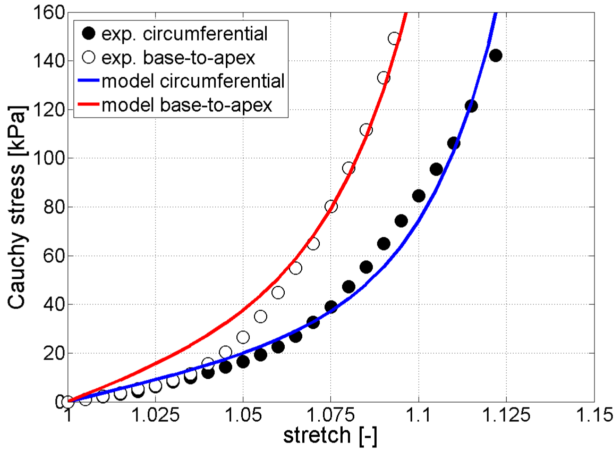

Figure C.1 *Circumferential and base-to-apex stress-stretch response of bovine pericardium [166] compared with numerical results obtained by using the model proposed by Holzapfel et al. [154].*

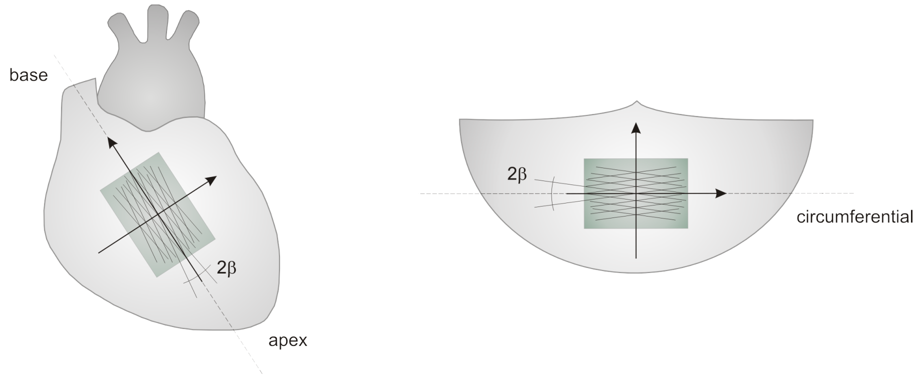

(a) (b)

Figure C.2 *Orientation of the two families of fibers: (a) in the bovine pericardium; (b) in the valve leaflet.*

C.2 Results

FEA is first performed to reproduce the implant of the aortic valve prosthesis and, then, once the prosthesis is virtually implanted and sutured inside the aortic root, a uniform pressure is applied to the leaflets in order to evaluate the performance of the reproduced surgical solution with particular focus on the effect of the chosen material model.
First of all, it is possible to observe that the adopted anisotropic material model produces reduced stress values on the leaflets with respect to the isotropic material model. Just comparing the maximum von Mises stress values, we have: $\sigma_M^A = 3.85$ MPa, $\sigma_M^B = 3.42$ MPa.
In Figure C.3, the von Mises stress patterns are represented for each investigated case using the same color scale.

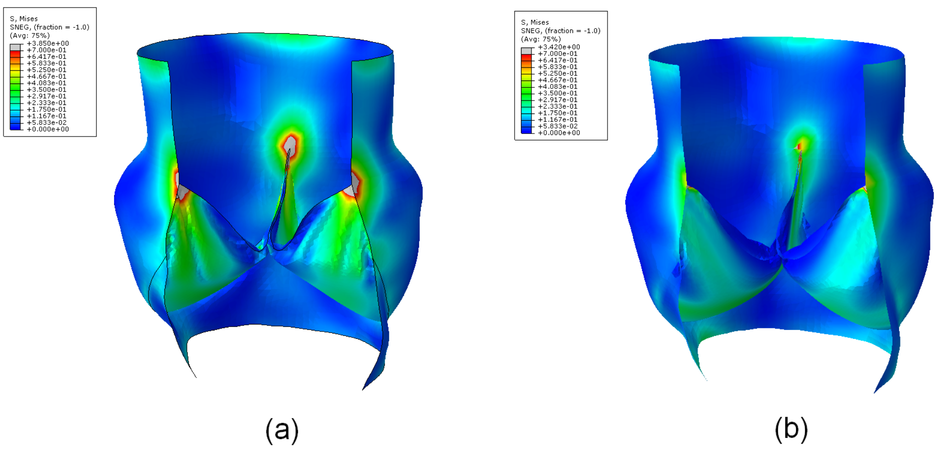

Figure C.3 *Von Mises stress pattern at the end of diastole: (a) isotropic material model and (b) fiber-reinforced model. A cut view is adopted to highlight the coaptation.*

To neglect peak values which can be affected by local effects we consider the average stress, σ_{av}, as defined in Equation 4.2.1.
The obtained values of σ_{av} are: $\sigma_{av}^A = 0.21$ MPa and $\sigma_{av}^B = 0.14$ MPa.
In Figure C.4 the stress distribution on the leaflets is shown from a top view.

Measures of coaptation are other important outcomes of our simulations since they explicitly indicate whether the simulated surgical intervention fails or not. In particular, we are able to measure (see Figure C.5): (i) the coaptation length, L_c, defined as the maximum effective length of coaptation; (ii) the height of coaptation, H_c, which is the distance between the plane where the annulus lies and the point where coaptation occurs; (iii) the coaptation area, A_c, defined as the total area of the elements in contact.

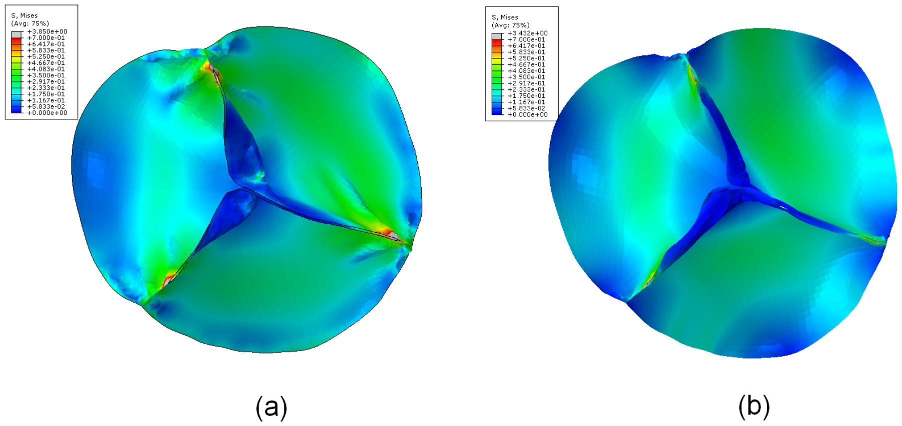

Figure C.4 *Von Mises stress distribution of the closed leaflets at the end of diastole: (a) isotropic material model; (b) anisotropic Holzapfel material model.*

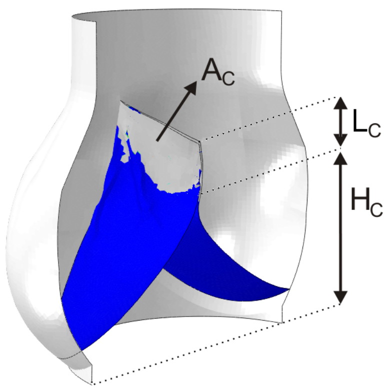

Figure C.5 *Measured coaptation parameters: area of coaptation, A_c, coaptation length, L_c, and coaptation height, H_c.*

In Table C.2 the measured values are summarized highlighting significant differences between an isotropic valve behavior and an anisotropic one.

Table C.2 *Length L_c, height H_c, and area A_c of coaptation obtained from each simulation.*

mat ID	L_c (mm)	H_c (mm)	A_c (mm^2)
A	2.75	16.8	277.5
B	7.57	13.03	609.4

C.3 Discussion

Through patient-specific FEA we are able to reproduce the post-operative behavior of a stentless valve, which means identifying the optimal surgical solution better tailored to the specific patient. Once the procedure has been developed, in fact, it is possible to investigate the impact of different factors (e.g., prosthesis type, prosthesis size, suture-line position) on the valve performance. In particular, herein we evaluate the influence of the adopted material model for the valve leaflets.
In the literature, several studies on the bovine pericardium are reported [163, 167, 168, 169]. Stated that the bovine pericardium is certainly an anisotropic material, there is no univocal opinion on the glutaraldehyde-treated pericardium, which for some authors exhibits an isotropic behavior [130, 131], while for others behaves as an anisotropic material [20, 166]. For this reason, in this paper we analyze the differences of considering an isotropic or a fiber-reinforced anisotropic model for the valve leaflets.
First of all, we may observe that the stress distribution on the closed valve leaflets is more homogeneous in case of anisotropic material model (see Figure C.4b). On the contrary, the isotropic leaflets present stresses predominantly aligned in the circumferential direction (see Figure C.4a). We may speculate that this result is due to the greater extensibility in the radial direction than in the circumferential one of the fiber-reinforced leaflets. This aspect leads also to the reduced stress values obtained adopting an anisotropic material model with respect to an isotropic model.
Moreover, the performed simulations confirm that anisotropic leaflets exhibit a smoother, more physiological closure (see again Figure C.4) and have a significantly greater coaptive area as reported in Table C.2. Furthermore, the coaptation length increases while the coaptation height decreases when moving from an isotropic to an anisotropic model. The results of this study demonstrate that the choice of the material model represents a tricky issue when performing numerical simulations.

Appendix D

Validation protocols

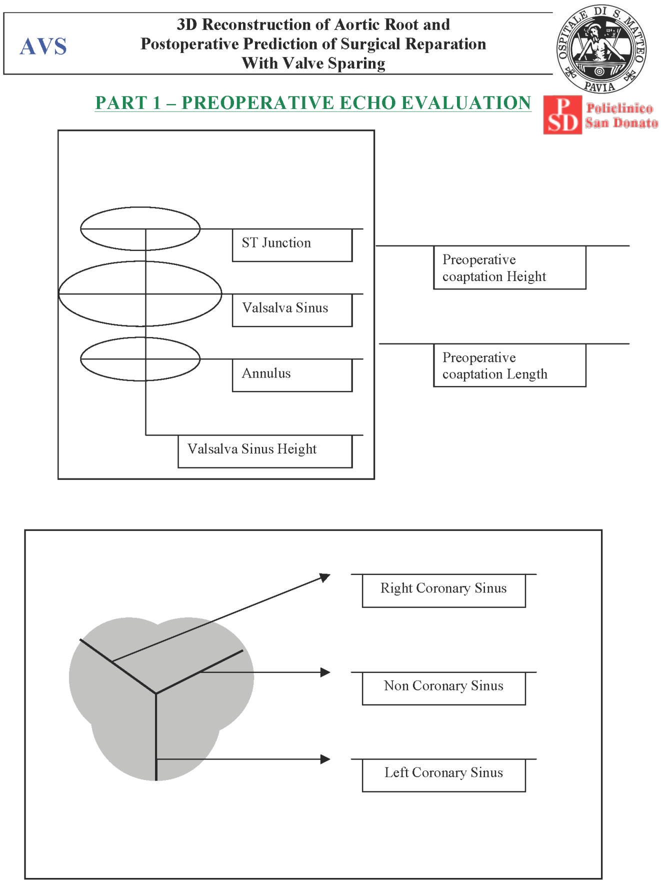

Figure D.1 *Preoperative echo evaluation for Aortic Valve Sparing*

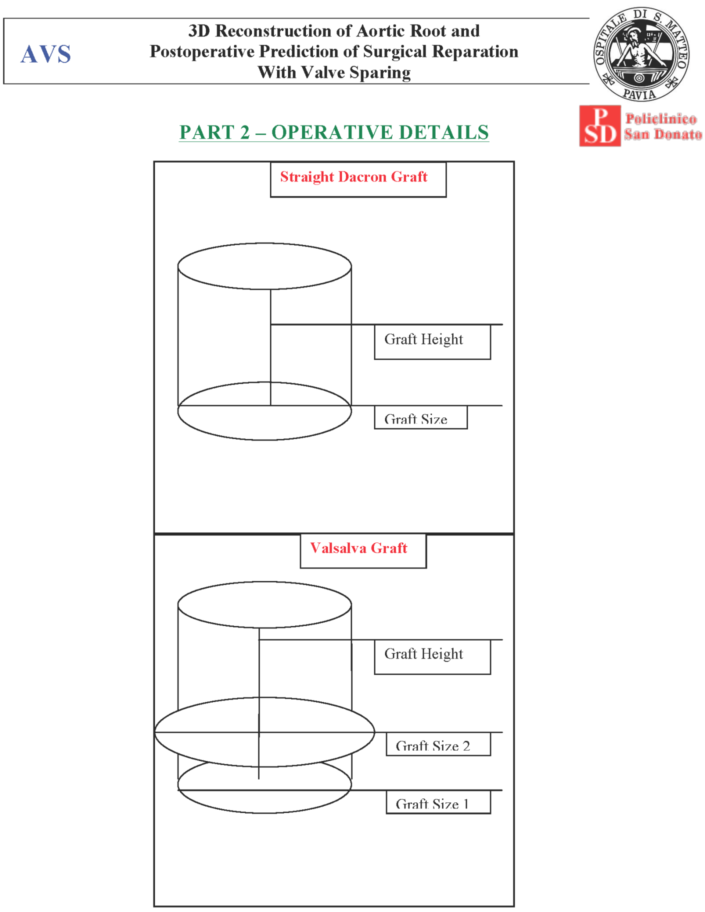

Figure D.2 *Operative details during Aortic Valve Sparing: graft type and dimensions*

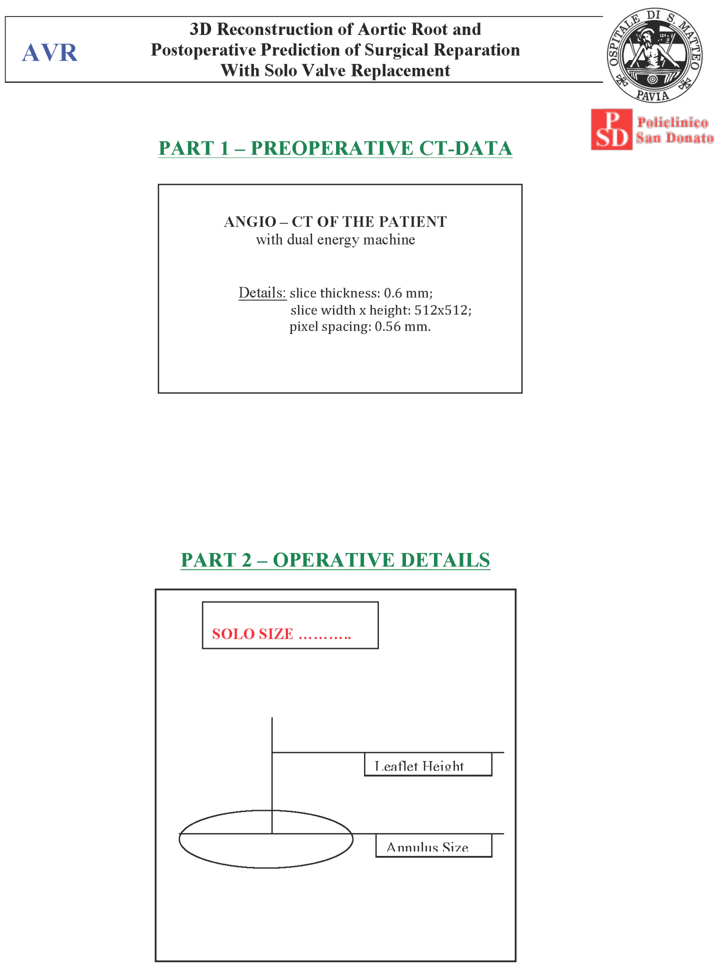

Figure D.3 *Preoperative requirement and operative details for Aortic Valve Replacement with a stentless valve*

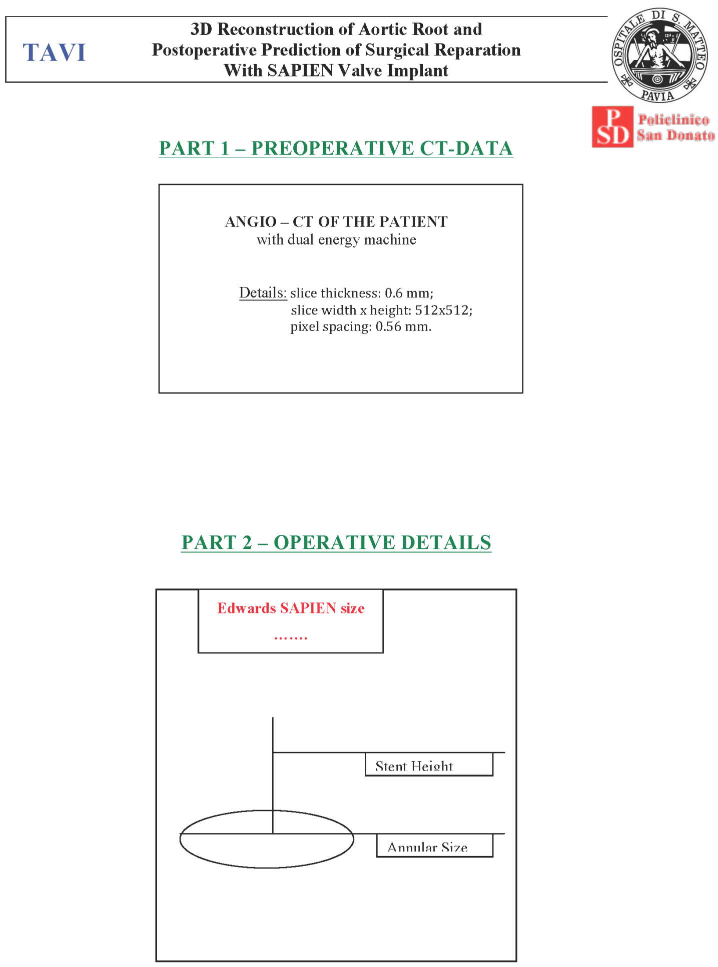

Figure D.4 *Preoperative requirement and operative details for Transcatheter Aortic Valve Implant*

AVS
AVR
TAVI

3D Reconstruction of Aortic Root and
Postoperative Prediction of Surgical Reparation
(in all cases)

PART 3a – POSTOPERATIVE ECHO EVALUATION

Coaptation Height

Coaptation Length

PART 3b – POSTOPERATIVE COMPUTER PREDICTION

Coaptation Height

Coaptation Length

Figure D.5 *Postoperative echo evaluation and simulation results*

List of Figures

List of Tables

Bibliography

[1] J.A. Cottrell, T.J.R. Hughes, and Y. Bazilevs. *Isogeometric Analysis: Toward Integration of CAD and FEA*. John Wiley and sons, 2009.

[2] S. Allender, P. Scarborough, V. Peto, M. Ryner, J. Leal, R. Luengo-Fernandez, and A. Gray. European cardiovascular disease statistics, 2008. University of Oxford.

[3] AHA committee. Heart disease and stroke statistics 2010 update: A report from the american heart association. *Circulation*, 121:e46–e215, 2010.

[4] V. T. Nkomo, J. M. Gardin, T. N. Skelton, J. S. Gottdiener, C. G. Scott, and M. Enriquez-Sarano. Burden of valvular heart diseases: a population-based study. *The Lancet*, 368:1005–1011, 2006.

[5] D. Messika-Zeitoun, L.F. Bielak, P.A. Peyser, P.F. Sheedy, S.T. Turner, V.T. Nkomo, J.F. Breen, J. Maalouf, C. Scott, A.J. Tajik, and M. Enriquez-Sarano. Aortic valve calcification : Determinants and progression in the population. *Arteriosclerosis, Thrombosis and, Vascular Biology*, 27:642–648, 2007.

[6] T.E. David. Aortic valve sparing operations. *Annals of Thoracic Surgery*, 73:1029–1030, 2002.

[7] R.E. Clark and G.A.M. Butterworth. Characterization of the mechanics of human aortic and mitral valve leaflets. *Surgical forum*, 22: 134–136, 1971.

[8] R.E. Clark. Stress-strain characteristics of fresh and frozen human aortic and mitral leaflets and chordae tendineae. *Journal of Thoracic and Cardiovascular Surgery*, 66:202–208, 1973.

[9] P.L. Gould, A. Cataloglu, G. Dhatt, A. Chattophadyay, and R.E. Clark. Stress analysis of the human aortic valve. *Computers and structures*, 3:377–384, 1973.

[10] P.L. Gould, A. Cataloglu, and R.E. Clark. Mathematical modelling of human aortic valve leaflets. *Applied Mathematical Modelling*, 1:33–36, 1976.

[11] A. Cataloglu, P.L. Gould, and R.E. Clark. Validation of a simplified mathematical model for the stress analysis of human aortic heart valves. *Journal of Biomechanics*, 8:347–348, 1975.

[12] A.A.H.J. Sauren. *The mechanical behavior of the aortic valve.* PhD thesis, Technische hogeschool Eindhoven, 1983.

[13] G.W. Christie and I.C. Medland. *Finite Element in Biomechanics.* John Wiley and Sons, 1982.

[14] H.N. Sabbah, M.S. Hamid, and P.D. Stein. Estimation of mechanical stresses on closed cusps of porcine bioprosthetic valves: Effects of stiffening, focal calcium and focal thinning. *American Journal of Cardiology*, 55:1091–1096, 1985.

[15] H.N. Sabbah, M.S. Hamid, and P.D. Stein. Mechanical stresses on closed cusps of porcine bioprosthetic valves: Correlation with sites of calcification. *Annals of Thoracic Surgery*, 42:93–96, 1986.

[16] E.P.M. Rousseau, A.A. van Steenhoven, J.D. Janssen, and H.A. Huysmans. A mechanical analysis of the closed hancock heart valve prosthesis. *Journal of Biomechanics*, 21:545–562, 1988.

[17] M.J. Thubrikar. *The Aortic Valve.* CRC Press, 1990.

[18] K. L. Billiar and M. S. Sacks. Biaxial mechanical properties of the natural and glutaraldehyde treated aortic valve cusp-Part I: Experimental results. *Journal of Biomechanical Engineering*, 122:23–30, 2000.

[19] Y. Liu, V. Kasyanov, and R.T. Schoephoerster. Effect of fiber orientation on the stress distribution within a leaflet of a polymer composite heart valve in the closed position. *Journal of Biomechanics*, 40:1099–1106, 2007.

[20] G. Arcidiacono, A. Corvi, and T. Severi. Functional analysis of bioprosthetic heart valves. *Journal of Biomechanics*, 38:1483–1490, 2005.

[21] N.J.B. Driessen, R.A. Boerboom, J.M. Huyghe, C.V.C. Bouten, and F.P.T. Baaijens. Computational analyses of mechanically induced collagen fiber remodeling in the aortic heart valve. *Journal of Biomechanical Engineering*, 125:549–557, 2003.

[22] N.J.B. Driessen, C.V.C. Bouten, and F.P.T. Baaijens. Improved prediction of the collagen fiber architecture in the aortic heart valve. *Journal of Biomechanical Engineering*, 127:329–336, 2005.

[23] N.J.B. Driessen, C.V.C. Bouten, and F.P.T. Baaijens. A structural constitutive model for collagenous cardiovascular tissues incorporating

the angular fiber distribution. *Journal of Biomechanical Engineering*, 127:494–503, 2005.

[24] A.D. Freed, D.R. Einstein, and I. Vesely. Invariant formulation for dispersed transverse isotropy in aortic heart valves. *Biomechanics and Modeling in Mechanobiology*, 4:100–117, 2005.

[25] T.M. Koch, B.D. Reddy, P. Zilla, and T. Franz. Aortic valve leaflet mechanical properties facilitate diastolic valve function. *Computer Methods in Biomechanics and Biomedical Engineering*, 13:225–234, 2010.

[26] M.R. Labrosse, C.J. Beller, F. Robicsek, and M.J. Thubrikar. Geometric modeling of functional trileaflet aortic valves: development and clinical applications. *Journal of Biomechanics*, 39:2665–2672, 2006.

[27] S.E. Clift and J. Fisher. Finite element stress analysis of a new design of synthetic leaflet heart valve. In *Proceedings of the Institution of Mechanical Engineers - part H*, volume 210, pages 267–272, 1996.

[28] B. Knierbein, U. Mohr-Matuschek, M. Rechlin, H. Reul, G. Rau, and W. Michaeli. Evaluation of mechanical loading of a trileaflet polyurethane blood pump valve by finite element analysis. *International Journal of Artificial Organs*, 13:307–315, 1990.

[29] F.L. Xiong, W.A. Goetz, C.K. Chong, Y.L. Chua, S. Pfeifer, E. Wintermantel, and J.H. Yeo. Finite element investigation of stentless pericardial aortic valves: Relevance of leaflet geometry. *Annals of Biomedical Engineering*, 38:1908–1918, 2010.

[30] K.J. Grande, R.P. Cochran, P.G. Reinhall, and K.S. Kunzelman. Mechanisms of aortic valve incompetence: Finite element modeling of aortic root dilatation. *Annals of Thoracic Surgery*, 69:1851–1857, 2000.

[31] K.J. Grande, R.P. Cochran, P.G. Reinhall, and K.S. Kunzelman. Mechanisms of aortic valve incompetence: finite element modeling of Marfan syndrome. *The Journal of Thoracic and Cardiovascular Surgery*, 122:946–954, 2001.

[32] K.J. Grande, R.P. Cochran, P.G. Reinhall, and K.S. Kunzelman. Mechanisms of aortic valve incompetence in aging: A finite element model. *Journal of Heart Valve Disease*, 8:149–156, 1999.

[33] C.A. Conti, A. Della Corte, E. Votta, L. Del Viscovo, C. Bancone, L.S. De Santo, and A. Redaelli. Biomechanical implications of the congenital bicuspid aortic valve: A finite element study of aortic root

function from in vivo data. *Journal of Thoracic and Cardiovascular Surgery*, 140:890–896, 2010.

[34] F. Auricchio, M. Conti, S. Demertzis, and S. Morganti. Finite element analysis of aortic root dilation: a new procedure to reproduce pathology based on experimental data. *Computer Methods in Biomechanics and Biomedical Engineering*, page in press, 2010.

[35] R. Gnyaneshwar, R.K. Kumar, and K.R. Balakrishnan. Dynamic analysis of the aortic valve using a finite element model. *Annals of T*, 73: 1122–1129, 2002.

[36] C.A. Conti, E. Votta, A. Della Corte, L. Del Viscovo, C. Bancone, M. Cotrufo, and A. Redaelli. Dynamic finite element analysis of the aortic root from MRI-derived parameters. *Medical Engineering & Physics*, 32:212–221, 2010.

[37] K. J. Grande-Allen, R.P. Cochran, P.G. Reinhall, and K.S. Kunzelman. Finite-element analysis of aortic valve-sparing: Influence of graft shape and stiffness. *IEEE Transactions on Biomedical Engineering*, 48:647–659, 2001.

[38] A. Ranga, O. Bouchot, R. Mongrain, Ugolini P, and Cartier R. Computational simulations of the aortic valve validated by imaging data: evaluation of valve-sparing techniques. *Interactive CardioVascular and Thoracic Surgery*, 5:373–378, 2006.

[39] K.S. Kunzelman, K.J. Grande, T.E. David, R.P. Cochran, and E.D. Verrier. Aortic root and valve relationships: impact on surgical repair. *Journal of Thoracic and Cardiovascular Surgery*, 107:162–170, 1994.

[40] L. Formaggia, A. Quarteroni, and A. Veneziani. *Cardiovascular mathematics: modeling and simulation of the circulatory system.* Springer-Verlag Italy, 2009.

[41] Texas Heart Institute. The Heart Valves, last access on August 2011. URL `http://www.texasheart.org/HIC/Anatomy/valves.cfm`.

[42] F. Saremi, S. Achenbach, E. Arbustini, and J. Narula. *Revisiting Cardiac Anatomy: a Computed-Tomography based atlas and reference.* Wiley-Blackwell, 2011.

[43] J.P. Sutton, S.Y. Ho, and R.H. Anderson. The forgotten interleaflet triangles: A review of the surgical anatomy of the aortic valve. *Annals of Thoracic Surgery*, 59:419–427, 1995.

[44] Mano J. Thubrikar, Michel R. Labrosse, Kenton J. Zehr, Francis Robicsek, Geoffrey G. Gong, and Brett L. Fowler. Aortic root dilatation

may alter the dimensions of the valve leaflets. *European Journal of Cardio-thoracic Surgery*, 28:850–856, 2005.

[45] G.M. Deeb. Freestyle® aortic root bioprosthesis: Modified subcoronary insertion technique, last access on Augus 2011. URL `http://www.ctsnet.org/doc/4690`.

[46] Y. Henderson and F.E. Johnson. Two modes of closure of heart valves. *Heart*, 4:69–82, 1912.

[47] I. Vesely. The role of elastin in aortic valve mechanics. *Journal of Biomechanics*, 31:115–123, 1998.

[48] J. de Hart, G. Cacciola, P.J.G. Schreurs, and G.W.M. Peters. Collagen fibers reduce stresses and stabilize motion of aortic valve leaflets during systole. *Journal of Biomechanics*, 31:629–638, 1998.

[49] R.I. Bashey, S. Torii, and A. Angrist. Age-related collagen and elastin content of human heart valves. *Journal of Gerontology*, 20:203–208, 1967.

[50] P. Stradins, R. Lacis, I. Ozolanta, B. Purina, V. Ose, and L. Feldmane. Comparison of biomechanical and structural properties between human aortic and pulmonary valve. *European Journal of Cardio-thoracic Surgery*, 26:634–639, 2004.

[51] J.T. Butcher, G.J. Mahler, and L.A: Hochaday. Aortic valve disease and treatment: the need for naturally engineered solutions. *Advanced Drug Delivery Reviews*, 63:242–268, 2011.

[52] Caitlin Martin, Thuy Pham, and Wei Sun. Significant differences in the material properties between aged human and porcine aortic tissues. *European Journal of Cardio-thoracic Surgery*, 40:28–34, 2011.

[53] P.D. Stein and W.A. Munter. New functional concept of valvular mechanics in normal and diseased aortic valves. *Circulation*, 44:101–108, 1971.

[54] R. Gramiak and P.M. Shah. Echocardiography of the normal and diseased aortic valves. *Radiology*, 96:1–8, 1970.

[55] M. Thubrikar, S.P. Nolan, J. Aouad, and J.D. Deck. Stress sharing between the sinus and leaflets of canine aortic valves. *Annals of Thoracic Surgery*, 42:434–440, 1986.

[56] T.R.P. Martin, J.A. Palmer, and M.M. Black. A new apparatus for the in vitro study of aortic valve mechanics. *Engineering in Medicine*, 7:229–230, 1978.

[57] M. Thubrikar, N. Harry, and S.P. Nolan. Normal aortic valve function in dogs. *American Journal of Cardiology*, 40:563–568, 1977.

[58] J.I.E. Hoffman and S. Kaplan. The incidence of congenital heart disease. *Journal of the American College of Cardiology*, 39:1890–900, 2002.

[59] B.F. Stewart, D. Siscovick, B.K. Lind, J.M. Gardin, J.S. Gottdiener, V.E. Smith, D.W. Kitzman, and C.M. Otto. Clinical factors associated with calcific aortic valve disease. *Journal of the American College of Cardiology*, 29:630–634, 1997.

[60] Proba123. Aortic stenosis characteristics, last access on May 2011. URL `http://probamyblog.wordpress.com/tag/aortic-stenosis-mnemonic/`.

[61] Phadney Cashews. Bicuspid aortic valve stenosis enlarged aortic root, last access on May 2011. URL `http://phadniscashew.asia/duracell-bicuspid-aortic-valve-symptoms`.

[62] B.H. Lorell and B.A. Carabello. Left ventricular hypertrophy : Pathogenesis, detection, and prognosis. *Circulation*, 102:470–479, 2000.

[63] J.B.P. de Waroux, A.C. Pouleur, C. Goffinet, D. Vancraeynest, M. Van Dyck, A. Robert, B.L. Gerber, A. Pasquet, G. El Khoury, and J.L. Vanoverschelde. Functional anatomy of aortic regurgitation: accuracy, prediction of surgical repairability, and outcome implications of transesophageal echocardiography. *Circulation*, 116:I 264 – I 269, 2007.

[64] R. Erbel, W. Daniel, C. Visser, R. Engberding, J. Roelandt, and H. Rennollet. Echocardiography in diagnosis of aortic dissection. *The Lancet*, 333:457–461, 1989.

[65] P.L. Darmon, Z. Hillel, A. Mogtader, B. Mindich, and D. Thys. Cardiac output by transesophageal echocardiography using continuous-wave doppler across the aortic valve. *Anesthesiology*, 80:796–805, 1994.

[66] R.C. Gilkeson, A.H. Markowitz, A. Balgude, and P.B. Sachs. Mdct evaluation of aortic valvular disease. *American Journal of Roentgenology*, 186:350–360, 2006.

[67] L.F. Squire and R.A. Novelline. *Squire's fundamentals of radiology (5th ed.)*. Harvard University Press, 1997.

[68] I.C. Joziasse, A. Vink, M.J. Cramer, M.F.M. van Oosterhout, L.A. van Herwerden, R. Heijmen, G.T.J. Sieswerda, B.J.M. Mulder, and P.A. Doevendan. Bicuspid stenotic aortic valves: clinical characteristics and morphological assessment using mri and echocardiography. *Netherlands Heart Journal*, 19:119–125, 2011.

[69] N.J.B. Driessen, A. Mol, C.V.C. Bouten, and F.P.T. Baaijens. Modeling the mechanics of tissue-engineered human heart valve leaflets. *Journal of Biomechanics*, 40:325–334, 2007.

[70] W.M. Swanson and R.E. Clark. Dimensions and geometric relationships of the human aortic valve as a function of pressure. *Circulation Research*, 22:871–882, 1974.

[71] M.A. Silver and W.C. Roberts. Detailed anatomy of the normally functioning aortic valve in hearts of normal and increased weight. *American Journal of Cardiology*, 55:454–461, 1985.

[72] K.J. Grande, R.P. Cochran, P.G. Reinhall, and K.S. Kunzelman. Stress variations in the human aortic root and valve: The role of anatomic asymmetry. *Annals of Biomedical Engineering*, 26:534–545, 1998.

[73] A. Rosset, L. Spadola, and O. Ratib. Osirix: An open-source software for navigating in multidimensional dicom images. *Journal of Digital Imaging*, 17:205–216, 2004.

[74] P.A. Yushkevich, J. Piven, H.C. Hazlett, R.G. Smith, S. Ho, J.C. Gee, and G. Gerig. User-guided 3D active contour segmentation of anatomical structures: Significantly improved efficiency and reliability. *Neuroimage*, 31(3):1116:1128, 2006.

[75] T.J.R. Hughes, A.J. Cottrell, and Y. Bazilevs. Isogeometric analysis: Cad, finite elements, nurbs, exact geometry, and mesh refinement. *Computer Methods in Applied Mechanics and Engineering*, 194:4135–4195, 2005.

[76] Y.C. Fung. Chapter: How are the heart valves operated? In *Biomechanics: circulation*, pages 42–49. Springer-Verlag, New York, 1997.

[77] M.J. Thubrikar, W.C. Piepgrass, L.P. Bosher, and S.P. Nolan. The elastic modulus of canine aortic valve leaflets in vivo and in vitro. *Circulation Research*, 47:792–800, 1980.

[78] P.M.F. Nielsen, P.J. Hunter, and B.H. Smaill. Biaxial testing of membrane biomaterials: testing equipment and procedures. *Journal of Biomechanical Engineering*, 113:295–300, 1991.

[79] J.D. Humphrey. Mechanics of the arterial wall: review and directions. *Critical Reviews in Biomedical Engineering*, 23:1–162, 1995.

[80] O. H. Yeoh. Some forms of the strain energy function for rubber. *Rubber Chemistry and Technology*, 66:754–771, 1993.

[81] Simulia. *Abaqus Manual.* Dassault Systèmes, Providence, RI, USA, 2010.

[82] A. Pandit, X. Lu, C. Wang, and G.S. Kassab. Biaxial elastic material properties of porcine coronary media and adventitia. *American Journal of Physiology: Heart and Circulatory Physiology*, 288:H2581–H2587, 2005.

[83] G.A. Holzapfel, G. Sommer, C.T. Gasser, and P. Regitnig. Determination of layer-specific mechanical properties of human coronary arteries with nonatherosclerotic intimal thickening and related constitutive modeling. *American journal of physiology. Heart and circulatory physiology*, 289:H2048–H2058, 2005.

[84] J.M. Ball. Convexity conditions and existence theorems in nonlinear elasticity. *Archives for Rational Mechanics and Analysis*, 63:337–403, 1977.

[85] J. Schröder and P. Neff. Invariant formulation of hyperelastic transverse isotropy based on polyconvex free energy functions. *International Journal of Solids and Structures*, 40:401–445, 2003.

[86] J. Schröder, P. Neff, and P. Balzani. A variational approach for materially stable anisotropic hyperelasticity. *International Journal of Solids and Structures*, 42:4352–4371, 2005.

[87] D. Balzani, P. Neff, J. Schröder, and G.A. Holzapfel. A polyconvex framework for soft biological tissues adjustment to experimental data. *International Journal of Solids and Structures*, 43:6052–6070, 2006.

[88] J. Stålhand and A. Klarbring. Aorta in vivo parameter identification using an axial force constraint. *Biomechanics and Modeling in Mechanobiology*, 3:191–199, 2005.

[89] J. Stålhand and A. Klarbring. Parameter identification in arteries using constraints. In G. A. Holzapfel and R. W Ogden, editors, *Mechanics of biological tissues*, pages 295–305. Springer, Wien, 2006.

[90] J. Stålhand, A. Klarbring, and M. Karlsson. Towards in vivo aorta material identification and stress estimation. *Biomechanics and Modeling in Mechanobiology*, 2:169–186, 2004.

[91] M. Soncini, E. Votta, S. Zinicchino, V. Burrone, A. Mangini, M. Lemma, C. Antona, and A. Redaelli. Aortic root performance after valve sparing procedure: a comparative finite element analysis. *Medical Engineering & Physics*, 31:234–243, 2009.

[92] A. Ranga, R. Mongrain, Y. Biadilah, and R. Cartier. A compliant dynamic FEA model of the aortic valves. In *Proceedings of 12th IFToMM World Congress, Besancon*, 2007.

[93] S. Petersen, V. Peto, M. Rayner, J. Leal, R. Luengo-Fernandez, and A. Gray. *European cardiovascular disease statistics.* BHF London, 2005.

[94] M.J. Davies. *Pathology of Cardiac Valves.* London, Butterworths, 1980.

[95] K.J. Grande, R.P. Cochran, P.G. Reinhall, and K.S. Kunzelman. Recreation of sinuses is important for sparing the aortic valve: a finite element study. *Journal of Thoracic and Cardiovascular Surgery*, 119: 753–763, 2000.

[96] G. Matalanis. Valve sparing aortic root repairs: An anatomical approach. *Heart Lung and Circulation*, 13S:S13–S18, 2004.

[97] T.E. David and C.M. Feindel. An aortic valve-sparing operation for patients with aortic incompetence and aneurysm of the ascending aorta. *Journal of Thoracic and Cardiovascular Surgery*, 103:617–621, 1992.

[98] R. Cochran, K.S. Kunzelman, A.C. Eddy, B.O. Hofer, and E.D. Verrier. Modified conduit preparation creates a pseudosinus in an aortic valve-sparing procedure for aneurysm of the ascending aorta. *Journal of Thoracic and Cardiovascular Surgery*, 109:1049–1057, 1995.

[99] T.E. David. Aortic root aneurysm: remodelling or composite replacement? *Annals of Thoracic Surgery*, 64:1564–1568, 1997.

[100] R.A. Hopkins. Aortic valve leaflet sparing and salvage surgery: evolution of techniques for aortic root reconstruction. *European Journal of Cardio-thoracic Surgery*, 24:886–897, 2003.

[101] R. De Paulis, G.M. De Matteis, P. Nardi, R. Scaffa, D.F. Colella, and L. Chiarello. A new aortic dacron conduit for surgical treatment of aortic root pathology. *Italian Heart Journal*, 1:457–463, 2000.

[102] K. Morishita, T. Abe, J. Fukada, H. Sato, and C. Shiiku. A surgical method for selecting appropriate size of graft in aortic root remodeling. *Annals of Thoracic Surgery*, 65:1795–1796, 1998.

[103] L.G. Svensson. Sizing for modified david's reimplantation procedure. *Annals of Thoracic Surgery*, 76:1751–1753, 2003.

[104] D. Maselli, A. Montalto, G. Santise, G. Minardi, C. Manzara, and F. Musumeci. A normogram to anticipate dimension of neo-sinuses

of valsalva in valve-sparing aortic operations. *European Journal of Cardio-thoracic Surgery*, 27:831–835, 2005.

[105] A.C. Kollar, S.D. Lick, and V.R. Conti. Valve-sparing aortic root reconstruction using in situ three-dimensional measurements. *Annals of Thoracic Surgery*, 87:1795– 800, 2009.

[106] Vascutek-Terumo. Gelweave Valsalva, last access October 2011. URL `http://www.terumo-us.com/`.

[107] M.A. Sarsam and M. Yacoub. Remodeling of the aortic valve anulus. *The Journal of Thoracic and Cardiovascular Surgery*, 105:435–438, 1993.

[108] T.E. David, C.M. Feindel, G.D. Webb, J.M. Colman, S. Armstrong, and M. Maganti. Long-term results of aortic valve-sparing operations for aortic root aneurysm. *Journal of Thoracic and Cardiovascular Surgery*, 132:347–354, 2006.

[109] T.E. David, S. Armstrong, M. Maganti, J. Colman, and T.J. Bradley. Long-term results of aortic valve-sparing operations in patients with marfan syndrome. *Journal of Thoracic and Cardiovascular Surgery*, 138:859–864, 2009.

[110] D. Maselli, G. Borelli, A. Amerini, P. Bajona, L. Bellieni, M. Croccia, and G. Minzioni. The ideal theoretical graft oversizing in valve-sparing aortic operations with a standard tubular or a valsalva graft. *European Journal of Cardio-thoracic Surgery*, 28:845–849, 2005.

[111] D. Maselli, R. De Paulis, R. Scaffa, L. Weltert, A. Bellisario, A. Salica, and A. Ricci. Sinotubular junction size affects aortic root geometry and aortic valve function in the aortic valve reimplantation procedure: An in vitro study using the valsalva graft. *The Annals of Thoracic Surgery*, 84:1214–1218, 2007.

[112] A. Avanzini. A computational procedure for prediction of structural effects of edge-to-edge repair on mitral valve. *Journal of Biomechanical Engineering*, 130:DOI: 10.1115/1.2913235, 2008.

[113] C. Capelli, A.M. Taylor, F. Migliavacca, P. Bonhoeffer, and S. Schievano. Patient-specific reconstructed anatomies and computer simulations are fundamental for selecting medical device treatment: application to a new percutaneous pulmonary valve. *Philosophical Transactions of the Royal Society*, 368:3027–3038, 2010.

[114] S Schievano, A.M. Taylor, C. Capelli, P. Lurz, J. Nordmeyer, F. Migliavacca, and P. Bonhoeffer. Patient specific finite element analysis results in more accurate prediction of stent fractures: application to

percutaneous pulmonary valve implantation. *Journal of Biomechanics*, 43(4):687–693, 2010.

[115] C.M. Feindel and T. E. David. Aortic valve sparing operations: basic concepts. *International Journal of Cardiology*, 97:61–66, 2004.

[116] J.P. Remadi, P. Marticho, A. Nzomvuama, and A. Degandta. Preliminary results of 130 aortic valve replacements with a new mechanical bileaflet prosthesis: the Edwards MIRA valve. *Interactive Cardiovascular and Thoracic Surgery*, 2:80–83, 2003.

[117] D. Pavoni, L.P. Badano, S.F. Musumeci, R. Frassani, P. Gianfagna, E. Mazzaro, and U. Livi. Results of aortic valve replacement with a new supra-annular pericardial stented bioprosthesis. *Annals of Thoracic Surgery*, 82:2133–2138, 2006.

[118] P. Totaro, N. Degno, A. Zaidi, A. Youhana, and V. Argano. Carpentier-Edwards PERIMOUNT Magna bioprosthesis: A stented valve with stentless performance? *The Journal of Thoracic and Cardiovascular Surgery*, 130:1668–1674, 2005.

[119] M. Glauber, S. Solinas, and J. Karimov. Technique for implant of the stentless aortic valve Freedom Solo. *Multimedia Manual of Cardiothoracic Surgery*, 13:161–167, 2007.

[120] G. Ganguly, Z.A. Akhunji, W.M.L. Neethling, and A.J. Hodge. Homograft aortic valve replacement: The experience of one unit. *Heart Lung and Circulation*, 13:161–167, 2004.

[121] C.-H. Yap and M. Yii. Allograft aortic valve replacement in the adult: A review. *Heart Lung and Circulation*, 13:41–51, 2004.

[122] A. Aboud, M. Breuer, T. Bossert, and J.F. Gummert. Quality of life after mechanical vs. biological aortic valve replacement. *Asian Cardiovascular and Thoracic Annals*, 17:35–38, 2010.

[123] A. Sedrakyan, P. Hebert, V. Vaccarino, A.D. Paltiel, J.A. Elefteriades, J. Mattera, Z. Lin, S.A. Roumanis, and H.M. Krumholz. Quality of life after aortic valve replacement with tissue and mechanical implants. *The Journal of Thoracic and Cardiovascular Surgery*, 128:266–272, 2004.

[124] P. Stassano, L. Di Tommaso, M. Monaco, F. Iorio, P. Pepino, N. Spampinato, and C. Vosa. Aortic valve replacement: A prospective randomized evaluation of mechanical versus biological valves in patients ages 55 to 70 years. *Journal of the American College of Cardiology*, 54:1862–1868, 2009.

[125] A. Kulik, P. Bedard, B.-K. Lam, F.D. Rubens, P.J. Hendry, R.G. Masters, T.G. Mesana, and M. Ruel. Mechanical versus bioprosthetic valve replacement in middle-aged patients. *European Journal of Cardio-thoracic Surgery*, 30:485–491, 2006.

[126] D.S. Peterseim, Y.Y. Cen, S. Cheruvu, K. Landolfo, T.M. Bashore, J.E. Lowe, W.G. Wolfe, and D.D. Glower. Long-term outcome after biologic versus mechanical aortic valve replacement in 841 patients. *Journal of Thoracic and Cardiovascular Surgery*, 117:890–897, 1999.

[127] P. Oses, J.P. Guibaud, N. Elia, G. Dubois, G. Lebreton, M. Pernot, and X. Roques. Freedom SOLO valve: early- and intermediate-term results of a single centre's first 100 cases. *European Journal of Cardio-thoracic Surgery*, doi:10.1016/j.ejcts.2010.04.038, 2010.

[128] S. Beholz, S. Dushe, and W. Konertz. Continuous suture technique for freedom stentless valve: Reduced crossclamp time. *Asian Cardiovascular and Thoracic Annals*, 14:128–133, 2006.

[129] T. Aymard, F. Eckstein, L. Englberger, M. Stalder, A. Kadner, and T. Carrel. The Sorin Freedom SOLO stentless aortic valve: Technique of implantation and operative results in 109 patients. *The Journal of Thoracic and Cardiovascular Surgery*, 139:775–777, 2010.

[130] J.M. Lee, S. A. Haberer, and D. R. Boughner. The bovine pericardial xenograft: I. effects of fixation in aldehydes without constraints on the tensile viscoelastic properties of bovine pericardium. *Journal of Biomedical Material Research*, 23:457–475, 1989.

[131] E. A. Trowbridge, M. M. Black, and C. L. Daniel. The mechanical response of glutaraldehyde fixed bovine pericardium to uniaxial load. *Journal of Material Science*, 20:114–140, 1985.

[132] M. Kass, A. Witkin, and D. Terzopoulos. Snakes: Active contour models. *International Journal of Computer Vision*, 1:321–331, 1988.

[133] W. Sun, K. Li, and E. Sirois. Simulated elliptical bioprosthetic valve deformation: Implications for a symmetric transcatheter valve deployment. *Journal of Biomechanics*, 43:3085–3090, 2010.

[134] B. Iung, G. Baron, E.G. Butchart, F. Delahaye, C. Gohlke-Barwolf, O.W. Levang, P. Tornos, J.-L. Vanoverschelde, F. Vermeer, E. Boersma, P. Ravaud, and A. Vahanian. A prospective survey of patients with valvular heart disease in europe: The euro heart survey on valvular heart disease. *European Heart Journal*, 24:1231–1243, 2003.

[135] A. Cribier, N. Saoudi, J. Berland, T. Savin, P. Rocha, and B. Letac. Percutaneous transluminal valvuloplasty of acquired aortic stenosis in elderly patients: an alternative to valve replacement? *The Lancet*, 327:63–67, 1986.

[136] E.B. Lieberman, T.M. Bashore, J.B. Hermiller, J.S. Wilson, K.S. Pieper, G.P. Keeler, C.H. Pierce, K.B. Kisslo, J.K. Harrison, and C.J. Davidson. Balloon aortic valvuloplasty in adults: Failure of procedure to improve long-term survival. *Journal of the American College of Cardiology*, 26:1522–1528, 1995.

[137] D.R. Holmes, R.A. Nishimura, and G.S. Feeder. In-hospital mortality after balloon aortic valvuloplasty : Frequency and associated factors. *Journal of the American College of Cardiology*, 17:189–192, 1991.

[138] A. Cribier, H. Eltchaninoff, A. Bash, N. Borenstein, C. Tron, F. Bauer, G. Derumeaux, F. Anselme, F. Laborde, and M.B. Leon. Percutaneous transcatheter implantation of an aortic valve prosthesis for calcific aortic stenosis: First human case description. *Circulation*, 106:3006–3008, 2002.

[139] E. Grube, J.C. Laborde, U. Gerckens, T. Felderhoff, B. Sauren, L. Buellesfeld, R. Mueller, M. Menichelli, T. Schmidt, B. Zickmann, S. Iversen, and G.W. Stone. Percutaneous implantation of the corevalve self-expanding valve prosthesis in high-risk patients with aortic valve disease: The siegburg first-in-man study. *Circulation*, 114: 1616–1624, 2006.

[140] J.I. Fann, N. Chronos, S.J. Rowe, R. Michiels, B.E. Lyons, M.B. Leon, and A.V. Kaplan. Evolving strategies for the treatment of valvular heart: preclinical and clinical pathways for percutaneous aortic valve replacement. *Catheterization and Cardiovascular Interventions*, 71: 434–440, 2008.

[141] C. Lally, F. Dolan, and P.J. Prendergast. Cardiovascular stent design and vessel stresses: a finite element analysis. *Journl of Biomechanics*, 38:1574–1581, 2005.

[142] P. Mortier, M. De Beule, D. Van Loo, B. Verhegghe, and P. Verdonck. Finite element analysis of side branch access during bifurcation stenting. *Medical Engineering & Physics*, 31:434–440, 2009.

[143] F. Auricchio, M. Conti, M. De Beule, G. De Santis, and B. Verhegghe. Carotid artery stenting simulation: From patient-specific images to finite element analysis. *Medical Engineering & Physics*, 33:281–289, 2011.

[144] J.G. Webb, M. Chandavimol, C.R. Thompson, D.R. Ricci, R.G. Carere, B.I. Munt, C.E. Buller, S. Pasupati, and S. Lichtenstein. Percutaneous aortic valve implantation retrograde from the femoral artery. *Circulation*, 113:842–850, 2006.

[145] S.V. Lichtenstein, A. Cheung, J. Ye, C.R. Thompson, R.G. Carere, S. Pasupati, and J.G. Webb. Transapical transcatheter aortic valve implantation in humans: Initial clinical experience. *Circulation*, 114: 591–596, 2006.

[146] N. Piazza, P. de Jaegere, C. Schultz, A.E. Becker, P.W. Serruys, and R.H. Anderson. Anatomhy of the aortic valvar complex and its implications of transcatheter implantation of the aortic valve. *Circulation Cardiovascular Interventions*, 1:74–81, 2008.

[147] A.N. Smuts, D.C. Blaine, C. Scheffer, H. Weich, A.F. Doubell, and K.H. Dellimore. Application of finite element analysis to the design of tissue leaflets for a percutaneous aortic valve. *Journal of the Mechanical Behavior of Biomedical Materials*, 4:85–98, 2011.

[148] E. Sirois, Q. Wang, and W. Sun. Fluid simulation of a transcatheter aortic valve deployment into a patient-specific aortic root. *Cardiovascular Engineering and Technology*, DOI: 10.1007/s13239-011-0037-7: –, 2011.

[149] A.N. Azadani, N. Jaussaud, P.B. Matthews, L. Ge, T. S. Guy, T.A.M. Chuter, and E.E. Tseng. Energy loss due to paravalvular leak with transcatheter aortic valve implantation. *Annals of Thoracic Surgery*, 88:1857–1863, 2009.

[150] H.A. Dwyer, P.B. Matthews, A. Azadani, L. Ge, T. S. Guy, and E.E. Tseng. Migration forces of transcatheter aortic valves in patients with noncalcific aortic insufficiency. *Journal of Thoracic and Cardiovascular Surgery*, 138:1227–1233, 2009.

[151] Edwards Lifesciences web-page. The Edwards SAPIEN valve, last access on April 2011. URL `http://www.edwards.com/products/transcathetervalves/Pages/sapienthv.aspx`.

[152] F. Auricchio, M. Di Loreto, and E. Sacco. Finite element analysis of a stenotic artery revascularization through a stent insertion. *Computer Methods in Biomechanics and Biomedical Engineering*, 4:249–263, 2001.

[153] A. Beck, M.J. Thubrikar, and F. Robicsek. Stress analysis of the aortic valve with and without the sinuses of valsalva. *Journal of Heart Valve Disease*, 10:1–11, 2001.

[154] G.A. Holzapfel, T.C. Gasser, and R.W. Ogden. A new constitutive framework for arterial wall mechanics and a comparative study of material models. *Journal of Elasticity*, 61:1–48, 2000.

[155] M. De Beule. *Finite Element Stent Design.* Phd thesis, University of Ghent, 2007/2008.

[156] P. Zioupos, J. C. Barbenel, and J. Fisher. Anisotropic elasticity and strength of glutaraldehyde fixed bovine pericardium for use in pericardial bioprosthetic valves. *Journal of Biomedical Materials Research*, 28:49–57, 1994.

[157] L. Piegl and W. Tiller. *The NURBS book. Monographs in visual communications.* Springer-Verlag, 1997.

[158] D.J. Benson, Y. Bazilevs, M.-C. Hsu, and T.J.R. Hughes. Isogeometric shell analysis: the reissner-mindlin shell. *Computer Methods in Applied Mechanics and Engineering*, 199:276–289, 2010b.

[159] D.J. Benson, Y. Bazilevs, E. De Luycker, M.-C. Hsu, M. Scott, T.J.R. Hughes, and T. Belytschko. A generalized finite element formulation for arbitrary basis functions: from isogeometric analysis to XFEM. *International Journal for Numerical Methods in Engineering*, 83:765–785, 2010a.

[160] M.J. Borden, M.A. Scott, J.A. Evans, and T.J.R. Hughes. Isogeometric finite element data structures based on bezier extraction of NURBS. *International Journal for Numerical Methods in Engineering*, 87:15–47, 2010.

[161] A. Radjeman, S. C. Liew, and K. O. Lim. Anisotropic elasicity of bovine pericardial tissue. *The Japanese Journal of physiology*, 35: 831–840, 1985.

[162] Y. L. Yue and S. P. Zhong. The machanical anisotropy of yak pericardium. In *Trans. 3rd World Biomaterials Congress "Biomaterials '88", Kyoto, Japan*, 1988.

[163] P. Zioupos, J. C. Barbenel, and J. Fisher. Mechanical and optical anisotropy of bovine pericardium. *Medical and Biological Engineering and Computing*, 30:76–82, 1992.

[164] E. A. Trowbridge and C. E. Crofts. The extension rate inependence of the hysteresis in glutaraldehyde-fixed bovine pericardium. *Biomaterials*, 8:201–206, 1986.

[165] D. Chachra, P.F. Gratzer, C.A. Pereira, and J.M. Lee. Effect of applied uniaxial stress on rate and mechanical effects of cross-linking in tissue-derived biomaterials. *Biomaterials*, 17:1865–75, 1996.

[166] S.E. Langdon, R. Chernecky, C.A. Pereira, D. Abdulla, and J. M. Lee. Biaxial mechanica/structural effects of equibiaxial strain during crosslinking of bovine pericardial xenogrfat materials. *Biomaterials*, 20:137–153, 1999.

[167] J. Lee and D. R. Boughner. Tissue mechanics of canine pericardium in different test environments. *Circulation Research*, 49:533–544, 1981.

[168] A.W. Wiegner, O.H.L. Bing, T.K. Borg, and J.B. Cauldfield. Mechanical and structural correlates of canine pericardium. *Circulation Research*, 49:807–814, 1981.

[169] F.C.P. Yin, P.H. Chew, and S.L. Zeger. An approach to quantification of biaxial tissue stress-strain data. *Journal of Biomechanics*, 19:27–37, 1986.